University of Memphis
University of Memphis Digital Commons

Electronic Theses and Dissertations

4-17-2017

Synthetic Design of Polysulfone Membranes: Morphological Effect on Property and Performance in Flow Batteries

Brandon Philippe Gindt

Follow this and additional works at: https://digitalcommons.memphis.edu/etd

Recommended Citation
Gindt, Brandon Philippe, "Synthetic Design of Polysulfone Membranes: Morphological Effect on Property and Performance in Flow Batteries" (2017). *Electronic Theses and Dissertations*. 1611.
https://digitalcommons.memphis.edu/etd/1611

This Dissertation is brought to you for free and open access by University of Memphis Digital Commons. It has been accepted for inclusion in Electronic Theses and Dissertations by an authorized administrator of University of Memphis Digital Commons. For more information, please contact khggerty@memphis.edu.

SYNTHETIC DESIGN OF POLYSULFONE MEMBRANES: MORPHOLOGICAL EFFECT ON PROPERTY AND PERFORMANCE IN FLOW BATTERIES

by

Brandon Gindt

A Dissertation

Presented in Partial Fulfillment of the

Requirements for the Degree of

Doctor of Philosophy

Major: Chemistry

University of Memphis

May 2017

DEDICATION

Of course, Caroline Sage and Madeline Gindt.

I would also like to take this time to acknowledge the many positive influences I have been fortunate enough to be exposed to.

ACKNOWLEDGEMENTS

I would like to thank the Department of Chemistry at the University of Memphis and NSF EPS-1004083 for supporting my education over the last 5 years.

I am very grateful for the guidance I have received from Dr. Fujiwara over the course of my PhD work. Under her supervision, I continually elevated my research abilities (which were nonexistent in 2012), which ultimately led me to this opportunity to defend my thesis.

My research has been a collaboration with Dr. Zawodzinski's (Dr. Z) and his group at the University of Tennessee. Dr. Z and his graduate student (at the time) Dr. Zhijiang Tang really helped move this research forward with constant optimism and superb data collection and analysis. It was a 100% team effort. Since Dr. Tang, many others have aided the coming research including Dr. Gabriel Goenaga, Dr. Mengkun Tian, and Melanie Lindsey. I also would like to thank all committee members for overseeing my research that began 5 years ago.

Thanks to all group members who graciously shared their knowledge and kindness that was crucial for this research to develop. Many professors aided in my "book-learning" throughout the years, strengthening my chemistry backbone. Dr. Burkey's classroom lectures were helpful in my understanding of general organic chemistry.

Again, Thank you all!

ABSTRACT

Gindt, Brandon, Philippe. Ph.D. The University of Memphis. May 2017. Synthetic Design of Polysulfone Membranes: Morphological Effect on Property and Performance in Flow Batteries. Major Professor: Tomoko Fujiwara, Ph.D.

This dissertation outlines a novel path towards improved understanding and function of proton exchange membranes (PEMs) for redox flow batteries, a large-scale battery storage device. This research uses synthetic methods and nanotechnology through two different approaches to prepare tailored polymer membranes:

1) Ion exchange membranes with enhanced chemical structures to promote membrane morphology on the nano-scale were prepared. Specifically, functional polysulfones (PSUs) were synthesized from different pre-sulfonated monomers. These PSUs have controlled placement and content of unique sulfonic acid moieties. PEMs were fabricated and characterized. The new PEMs showed desirable physical properties and performance in a vanadium redox flow battery (VRFB) cell.

2) Nanoporous PSU membranes were fabricated via post-hydrolysis of polylactide (PLA) from PLA-PSU-PLA triblock copolymer membranes. The controlled morphology and pore size of the resulting nanoporous membranes were evaluated by different microscopy and scattering techniques to understand structure-property relationships. Further, the resulting nanopore surface was chemically modified with sulfonic acid moieties. Membranes were analyzed and evaluated as separators for a VRFB. The chemically modified nanoporous PEMs exhibited unique behavior with respect to their ion conductivity when exposed to solutions of increasing acid concentration. In addition, the hierarchical micro-nanoporous membranes developed further showed promising structure and properties.

PREFACE

This dissertation is based on two published journal articles. Chapter 2 is a modified version of paper published in *Journal of Membrane Science* **2017**, *532*, 58. Chapter 3 is a modified version of paper published in *Journal of Materials Chemistry A* **2016**, *4*, 4288. Chapters 4 & 5 are based on nanoporous membranes, and manuscript is in preparation. Specifically, Chapter 4 will be published after further battery analyses on these membranes are complete. Chapter 5 details different pore modifications developed to modify porous PSU membranes. The guidelines followed are from the *Journal of the American Chemical Society*.

TABLE OF CONTENTS

LIST OF TABLES

LIST OF FIGURES

ABBREVIATIONS

AEAPST	N-(2-Aminoethyl)-3-Aminopropyl Silane-triol
AEM	Anion Exchange Membranes
AFM	Atomic Force Microscopy
APS	Advanced Photon Source
ASR	Area Specific Resistance
ATR-FTIR	Attenuated Total Reflection Fourier Transform Infrared Spectroscopy
Bisphenol AF	4,4′-(Hexafluoroisopropylidene) Diphenol
BPA	Bisphenol A or 4,4'-(Propane-2,2-Diyl) Diphenol
CAES	Compressed-Air Energy Storage
CDCl3	Deuterated Chloroform
CEMs	Cation Exchange Membranes
CMCS	Carboxy Methyl Cellulose Sodium Salt
DBP	Dibutyl Phthalate
DBU	1,8-Diazabicyclo[5.4.0]Undec-7-Ene
DCDPS	4,4’-Dichlorodiphenyl Sulfone
DCM	Dichloromethane
DFDPS	4,4’-Difluorodiphenyl Sulfone
DMAc	N,N-Dimethylacetamide
DMF	N,N-Dimethylformamide
DMSO	Dimethyl Sulfoxide
DSC	Differential Scanning Calorimetry

DVB	Divinyl Benzene
EDS	X-Ray Dispersive Analysis
FESEM	Field Emission Scanning Electron Microscope
GPC	Gel Permeation Chromatography
HDFTHDTES	Heptadecafluoro-1,1,2,2-Tetrahydrodecyl) Triethoxy Silane
IEC	Ion Exchange Capacity
IPA	Isopropanol
JCESR	U.S. Joint Center For Energy Storage Research
NF	Nanofiltration
NIPS	Non-Solvent Induced Phase Separation
NMP	N-Methyl-2-Pyrrolidone
NMR	Nuclear Magnetic Resonance
NSF	National Science Foundation
OCV	Open-Circuit Voltage
PAA	Poly(Acrylic Acid)
PAN	Polyacrylonitrile
PBI	Polybenzimidazole
PDDA	Diallyldimethylammonium Chloride
PDI	Polydispersity Index
PDMS	Poly(Dimethylsiloxane)
PEEK	Polyetheretherketone
PEG	Polyethylene Glycol
PEM	Proton Exchange Membrane

PEMFC	Proton Exchange Membrane Fuel Cells
PEO	Polyethylene Oxide
PFSA	Perfluorosulfonic Acid Polymers
PIM-1	Polymer of Intrinsic Microporosity 1
PLA	Polylactide
PPSU	1-Propenyl Functionalized Polysulfone
PPY	Polypyrrole
PS	Polystyrene
PSS	Polystyrene Sulfonate
PSU	Polysulfone
PTESPC	O-(Propargyl)-N-Triethoxysilyl Propyl Carbamate
PTFE	Polytetrafluoroethylene
PVDF	Polyvinylidene Fluoride
RFB	Redox Flow Batteries
ROP	Ring Opening Polymerization
SAXS	Small-Angle X-Ray Scattering
SEM	Scanning Electron Microscopy
SIEM	Size Exclusion Membranes
SPEEK	Sulfonated Polyetheretherketone
SPEEKK	Sulfonated Polyetherketone
SR-LBL	Solvent Responsive Layer-By-Layer
TEM	Transmission Electron Microscopy
TGA	Thermal Gravimetric Analysis

THF	Tetrahydrofuran
TMS	Tetramethylsilane
TPPMS	Sodium Diphenylphosphinobenzene-3-Sulfonate
UF	Ultrafiltration
VIPS	Vapor Induced Phase Separation
VRFB	Vanadium Redox Flow Batteries

Chapter 1

Introduction

1.1 Background

Current electric power is generated mostly from nonrenewable energy sources that supply reliable and constant power. These energy sources have been indispensable in our modern power-driven world. However, critical concerns such as climate change and sustainability continue to draw attention. Thus, there has been a growing demand for alternative energy. Innovative and creative solutions to cut emissions, reduce waste, and provide a more sustainable power system nationwide have been proposed to address these critical issues. Many of these solutions rely on intermittent sources, such as wind or solar to generate electric power. The U.S. has steadily increased the use of non-hydro renewables over recent years, i.e., from 4.2% in 2010 to 9.2% in 2015.[1] If intermittent energy sources continue to grow at this rapid pace with no countermeasures, the grid could become destabilized.[2]

To fully utilize these intermittent energy sources, their unpredictable nature must be addressed. One obvious way is to incorporate large scale energy storage.[3-6] To date, various energy storage devices have been proposed to resolve this problem by storing electricity during times of high output and releasing it during low output. These devices convert electrical energy to another form of energy while charging, then revert to electrical energy during discharge.[7]

The employed technologies for a large-scale energy storage are compressed-air energy storage (CAES), pumped hydroelectric, redox flow batteries (RFB), superconductors, and flywheels.[6] Pumped-hydro accounts for the majority of worldwide

energy storage capacity with CAES being a distant second. However, pumped-hydro and CAES are geographically limited. In contrast, the RFB is a flexible electrochemical storage device that shows high efficiency and durability in many demonstration plants worldwide. The RFB uses two separate electroactive species of different potential to produce and store energy through a reversible redox reaction.[8]

The vanadium redox flow battery (VRFB) is a specific type of RFB that uses vanadium ions for both oxidation and reduction half-reactions. The reversible redox reaction is shown below:

$$VO^{2+} + H_2O - e^- \rightarrow VO_2^+ + 2H^+ \qquad (E_0 = 0.99 \text{ V vs. SHE})$$
$$V^{3+} + e^- \rightarrow V^{2+} \qquad (E_0 = -0.26 \text{ V vs. SHE})$$

$$E^0_{cell} = E^0_{red} - E^0_{ox}$$

$$E^0_{cell} = 0.99\,V + 0.26\,V = 1.25\,V$$

Historically, the VRFB draws the most attention because it can minimize negative effects from crossover of the active species. A schematic of the VRFB is shown in Figure 1-1. The battery uses two separate tanks to store anodic and cathodic solutions that circulate through a cell stack where the redox reaction between the solutions occurs. During discharge, electrons transfer from the more reduced to the more oxidized storage tank through an external circuit. In the cell stack an ion selective membrane permits the passage of charge carriers, usually protons, for charge balance in the system while preventing cross-mixing of the bulk electrolyte solutions.

In a VRFB system, vanadium ions of different oxidation states serve as both the cathodic and anodic active metals. A large advantage of using the same metal is no permanent capacity loss from electrolyte crossover. Other redox couples would require

separation of different metal active species that would increase maintenance cost. One disadvantage of the all-vanadium redox couple is the high cost of vanadium metal.

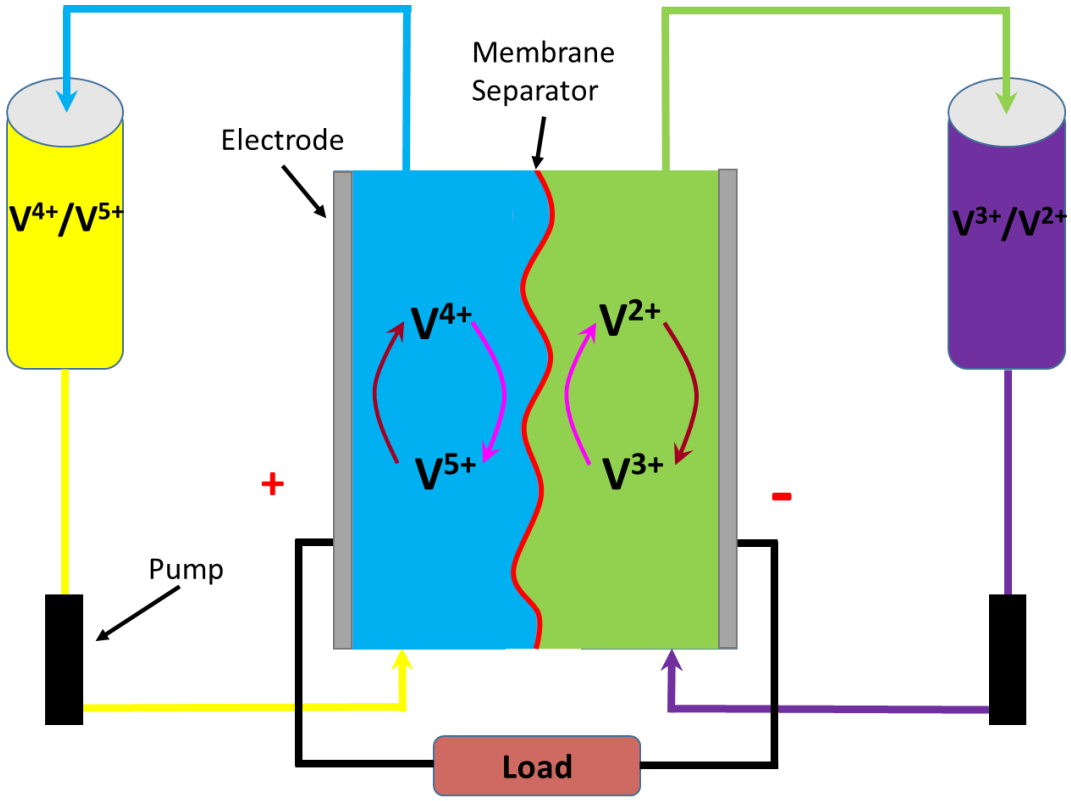

Figure 1-1 Schematic of a vanadium redox flow battery. Redox reactions are shown for charging (pink) and discharging (red).

1.2 Membrane Separators

One of the key components in VRFBs is the membrane separator. The separator in the cell serves the dual purpose of partitioning the bulk electrolyte solutions and supporting the passage of charge carriers during operation. The underlying principles of how membrane separators function in VRFBs and related systems such as proton exchange membrane fuel cells (PEMFC) are well studied. However, a more detailed understanding of ion transport and other factors is still being developed. The current model employs nano-size pores in the material to facilitate transfer of ions through the

membrane. Other characteristics of the pores such as size and surface charge are important in promoting the passage of ions and will be discussed later.

Ideally, a membrane should meet the following requirements; 1) chemically and physically robust, 2) highly ion selective, 3) electrically insulating, 4) derived from low cost materials, and 5) minimize solvent transfer. Chemical resistance prevents premature membrane failure caused by the highly acidic electrolyte solutions that also contain potent oxidizers such as VO_2^+. The US Joint Center for Energy Storage Research (JCESR) is targeting batteries capable of more than 7,000 cycles or approximately 20 years of usage, emphasizing the importance on durability.[7] High ion selectivity allows protons to travel through the membrane, while preventing crossover of other ionic species that would lower efficiency and increase capacity decay. Membrane cost is possibly the most important criteria. Current commercial membrane separators are responsible for ~11% of the overall cost for the battery system.[9] Many battery components such as vanadium have limited cost flexibility because they are essential elements in the system. If the system is not competitive financially with the current electrical infrastructure it will never commercialize.

Nafion® and other perfluorosulfonic acid polymers (PFSA) are the most widely used membrane separators for VRFBs and related applications such as PEMFC. Nafion shows satisfactory energy efficiency in a VRFB, but its most advantageous attribute is its durability. PFSAs are exceptionally inert in harsh chemical environments and possess good mechanical properties. Although this class of membranes possesses high proton conductivity, one significant downfall is low ion selectivity. Low selectivity reduces efficiency during cycling and leads to rapid capacity decay. This drawback, coupled with

their high cost, is the continuous driving force for researchers to design alternative membranes that overcome the shortcomings of Nafion.

Various types of membranes with different chemical and physical properties were investigated for use in a VRFB and related systems. Four classes of membranes dominate in recent literature are the following: 1) PFSAs, 2) non-perfluorinated proton exchange membranes, 3) anion exchange membranes, and 4) porous membranes.[10] As previously noted, PFSAs have been studied in most battery and fuel cell systems. Non-perfluorinated proton exchange membranes (PEMs) are considered to be an alternative membrane due to their superb performance and lower costs than PFSAs. Anion exchange membranes (AEMs) received little attention historically; but they have attracted increased attention over the past several years for their high ion selectivity. Finally, in a recent few years porous membranes are experiencing a revival particularly in RFBs, where they show the potential as alternate PEMs.

1.2.1 Perfluorosulfonic acid membranes

Nafion and other PFSAs monopolize separators used in commercial VRFB systems despite the persistent research and evaluation of alternative membranes over the years. Industrially, PFSA membranes are used in many applications such as the first commercially available hydrogen fuel cell automobile. Nafion consists of a polytetrafluoroethylene (PTFE) backbone with perfluorinated sulfonic acid side groups. The hydrophilic sulfonic acid group uptakes water to form ca. 2-3 nm hydrated pores.[11-16] Protons can permeate through the hydrated pores via a Grotthuss or hopping mechanism or by a vehicle mechanism where the amount of hydration is significant. Zawodzinski *et al.* thoroughly evaluated water diffusion and uptake in Nafion and other PFSA

membranes, which highlighted the importance of water in proton conductivity.[17-19] Hydration of the sulfonic acid moiety is different depending on the type of membrane the sulfonic acid group is bound.[20,21]

1.2.2 Hydrocarbon based proton exchange membranes

Non-perfluorinated PEMs generally have negatively charged (anionic) ionic groups that show selectivity towards positive ions such as a proton. For PEM applications, the ionic group is a strong acid, most often a sulfonic acid moiety. Early development of this class of materials was predominantly done for PEMFC, but it has since been translated over to other PEM applications. The sulfonic acid groups promote formation of pores slightly smaller than Nafion (ca. 2 nm). Sulfonated aromatic polymers show high energy efficiency during cell cycling with required durability in the condition. Figure 1-2 illustrates the differences of pore size and connectivity in Nafion and sulfonated polyetherketone (SPEEKK). SPEEKK structure is not as defined as Nafion's, that is, it has more branched channels with dead-end "pockets". This structural difference accounts for its lower proton conductivity at equivalent ion exchange capacity (IEC).

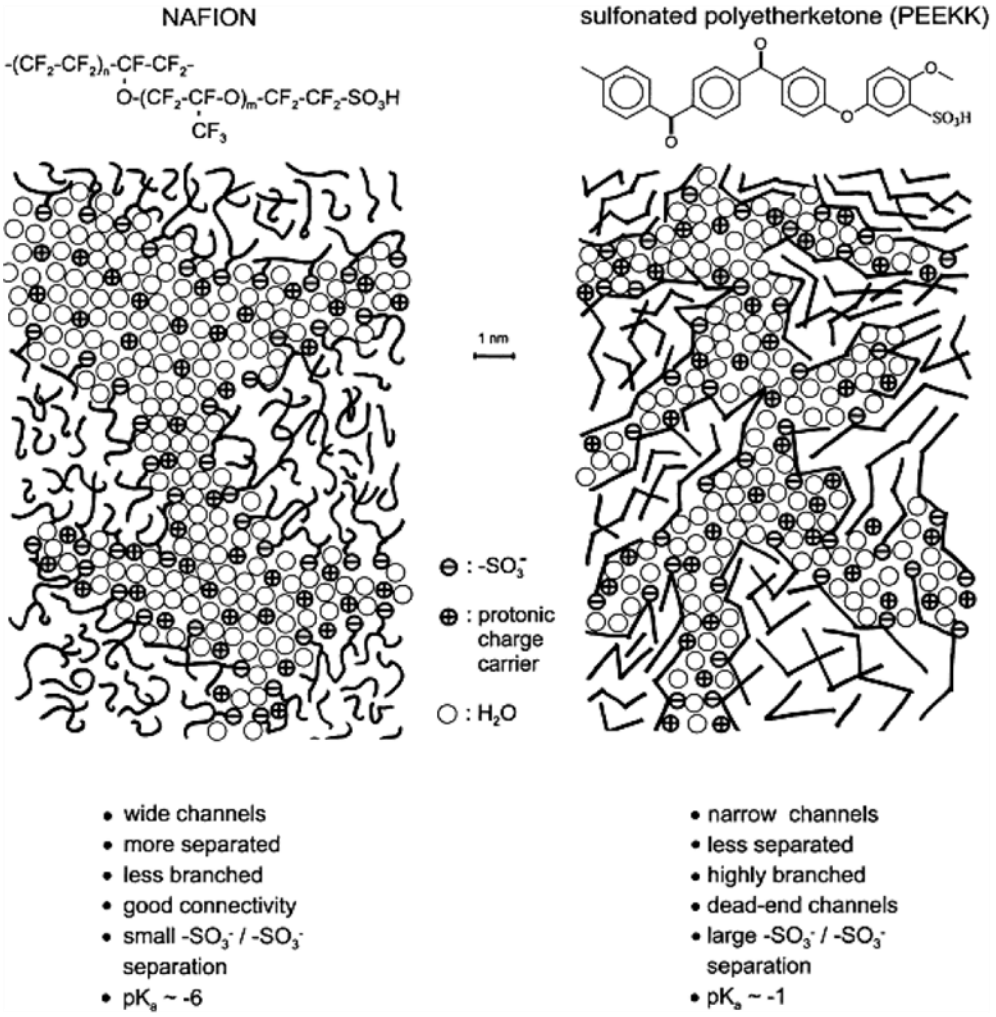

Figure 1-2 Schematic representation of the microstructures of NAFION and a sulfonated polyetherketone (derived from SAXS experiments) illustrating the less pronounced hydrophobic/hydrophilic separation of the latter compared to the former.[21]

Aromatic sulfonated polymers have been developed as PEMs, e.g., polysulfone (PSU), polyetheretherketone (PEEK), polybenzimidazole (PBI), polyphenylene, polyimide, and others. These common engineering polymers are physically robust and chemically resistant. Sulfonated PSU membranes have shown excellent energy performance and are also readily scalable.[22,23] These PEMs are capable to possess high proton conductivity; however, it requires significantly high IEC that simultaneously decreases membrane durability considerably.[24,25] Partially fluorinated PEMs are also

investigated and found to show effect morphology and performance.[26] Numerous reviews on these materials have been published.[24,25]

Structure-property relationship of non-perfluorinated proton exchange membranes has been well studied. It is known that the polymer architecture significantly affects morphology and performance of the membranes.[27] For example, to mimic phase separation of Nafion, the use of block copolymers can improve both battery performance and physical properties over the membrane from the corresponding random copolymer. McGrath *et al.* improved proton conductivity and ion selectivity by controlling the polymer architecture.[26,28-32] They demonstrated that the self-assembled morphology of block copolymers promoted more defined and connected ion transport channels which led to decreased water uptake and increased proton conductivity. Block compatibility and block length in the copolymers significantly affected the morphology and performance. Small-angle X-ray scattering (SAXS) of a polysulfone based block copolymer revealed that increased block size generated larger domains and improved self-assembly in the membranes as shown in Figure 1-3. This translated to increased performance in PEMFCs.

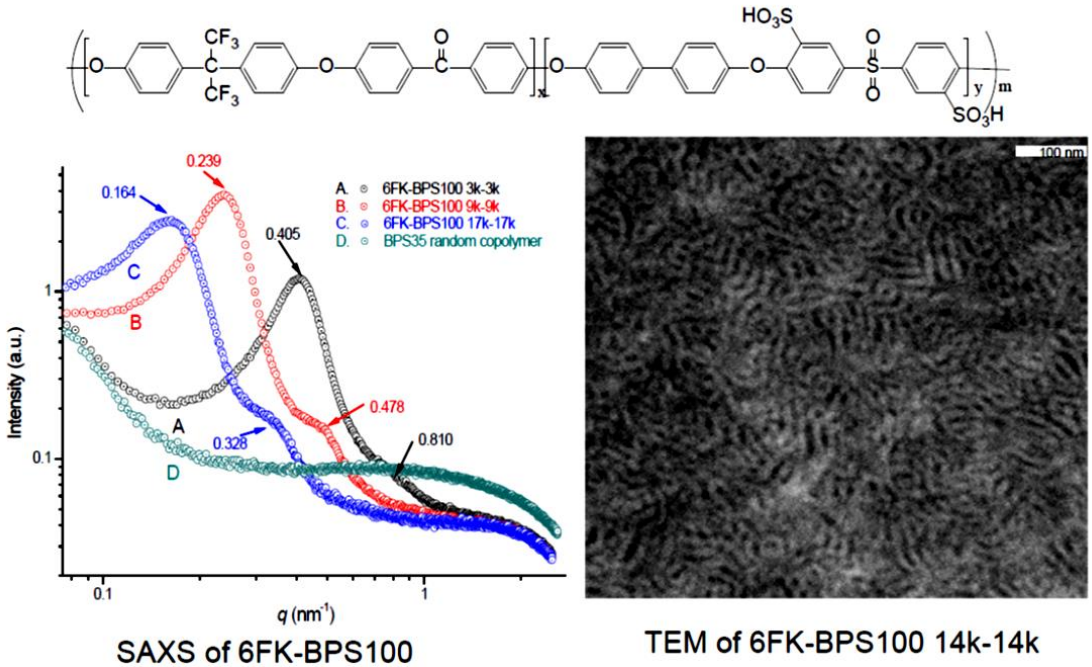

Figure 1-3 Block length effect on morphology for block copolymers.[33,34] (Mcgrath *et. al.* 2013 Advances in Materials for Proton Exchange Membrane Fuel Cells Systems)

Other strategies to facilitate self-assembly of the ion channels, such as designing the placement and number of acid groups on the polymer backbone, improving chain flexibility, and increasing acid pK_a have also improved morphology and PEM performance.[26,28,30,31,35-40]

1.2.3 Anion exchange membranes

This class of membranes is derived from polymers possessing anion exchange groups, e.g., quaternary ammonium groups. Commonly used anion exchange group is a quaternized trimethyl amine group that is covalently bound to the polymer backbone. AEMs provide high ion selectivity in VRFBs in part due to the Donnan exclusion principle.[41] The positively charged ionic channels can repel the positively charged vanadyl ions considerably well.[42]

PEMs generally show higher vanadyl permeability than their AEM analogs because the current is exclusively carried by protons for PEMs, while the current is carried by both protons and sulfate ions in AEMs. Thus, the lower resistivity of the PEM is due to the higher mobility of protons compared to that of hydrogen sulfate and sulfate ions.[43] Both PEMs and AEMs have shown their advantages and disadvantages when used as a separator in VRFB.[42]

1.2.4 Porous membranes

Porous materials are by far the least characterized as VRFB separators in spite of their potential to reduce cost over other alternatives. Porous membranes are readily available and found in applications such as nanofiltration (NF) , size exclusion, battery separators, dialysis and so forth. Porous membranes were first evaluated by Skyllas-Kazacos *et al.* in her pioneering work on VRFBs in the late 80s. Daramic separators (commercially available nanoporous polyethylene/SiO_2 membrane) functionalized by different chemistries gave good battery efficiency.[44,45] Depending on the treatment procedure, they were able to improve proton conductivity or control vanadium crossover. This early work has not attracted much attention until the last few years.

The renewed porous separators and their fabrication methods offer high proton conductivity, ion selectivity, and oxidative resistance. Recent studies using nano- to micro-size porous membranes in VRFBs showed higher energy efficiency than Nafion with comparable durability. A comprehensive comparison of polymer membranes used in VRFBs is presented in Table 1-1.

Table 1-1 Comparison of VRFBs polymer membranes.[10]

Membrane type	Ionic conductivity	Selectivity	Stability
Nafion	High	Low	Excellent
Modified Nafion	Medium	Medium	Excellent
Other PEMs	Medium	Medium	Medium
AEMs	Low	High	Low
AIEMS[b]	Medium	High	Low
Non-ionic porous	Medium	Medium	N/A[a]

[a] N/A: not applicable
[b] AIEMS: Amphoteric ion exchange membranes (cationic and anionic exchange groups present)

1.3 Literature Review on Porous Membrane Separators

In this section, reports on recent porous membrane separators in VRFBs are reviewed. Majority of related work were done primarily by a few research groups and were focuseed on the membrane fabrication and efficiencies during battery cycling. During cycling, three main efficiencies are collected simultaneously: 1) coulombic efficiency (CE), 2) voltage efficiency (VE), and 3) energy efficiency (EE). The three efficiencies can be calculated using the following equations:

$$CE = \frac{Q_{discharge}}{Q_{charge}}$$

$$VE = \frac{V_{discharge}}{V_{charge}}$$

$$EE = CE \times VE$$

where Q is the capacity at either charge or discharge and V is the average voltage at charge or discharge. Table 1-2 shows a compilation of these membranes described below for a comparative analysis.

Table 1-2 Comparison of efficiencies for recent porous membranes cycled in VRFBs at different current densities.

ref	Fabrication-polymer-thickness	current density #1	CE%	VE%	EE%	current density #2	CE%	VE%	EE%
PBI Porous Membranes									
[46]	Commercial-PBI-30 um	80	99	~66	~65	40	99	79	79%
[47]	Porogen (PEG400) extract-PBI- 45 um	80	~99	~69	~68	40	99.4	78.7	78.2
[48]	VIPS-PBI-87 um	xxx	xxx	xxx	xxx	40	99	~87	~87
[49]	VIPS-PBI-68 um	80	100	89	89	40	99	94	93
[49]	VIPS-PBI-34 um	80	98	92	90	40	96.5	95	92
[50]	Porogen (DBP) extract-PBI - 103 um	80	99	86	85	40	98	91	89
PSU:SPEEK Porous Membranes									
[51]	NIPS-PSU(28) SPEEK(7) - 130 um 7 bilayers	80	94.5	87	83	120	96	83	79
[52]	NIPS-PSU(80) SPEEK(20)-130 um 7.5 bilayers (+)	80	97.5	93	91	180	99	81	80
[52]	NIPS-PSU(80) SPEEK(20) -130 um 7 bilayers (-)	80	94	91	86	180	94	79	74
[53]		80	96.3	90.55	87.2	160	98.11	79.98	78.47
[54]	VIPS- PSU(87) SPEEK(13) - 85 um	80	93	85	79	160	98	70	68
Others									
[55]	Commercial - PIM1 coated PAN -50 um					40	98	82	80
[56]	NIPS w/THF-PAN-500 um	80	95	83	79	40	90	90	81
[57]	Drop cast - PSU/PVP -35 um	80	95	84	80	40	93	89	83
[58]	NIPS -PVDF-125 um	80	95	82.7	78.6	40	90.3	90	81.3
[59]	NIPS - quatarnized PSU-200 um	80	99	78	77	40	97	87	85

1.3.1 Daramic Membrane Functionalization

Daramic is a porous membrane with ~100 nm pores that are highly disordered, while remaining well connected. The main component in Daramic, PE, is a common

polymeric material used in battery separators due to adequate chemical and physical properties.

Daramic was treated in either polystyrene sulfonate (PSS), Amberlite CG400, or carboxy methyl cellulose sodium salt (CMCS) solution to fill its pores. Afterwards, the "stuffing agent" was trapped by crosslinking with divinyl benzene (DVB).[60] This reduced the pore size for all membranes increased resistance but improved selectivity. This improved CE at the expensive of VE for the modified membranes. The Amberlite modified membrane yielded the highest EE compared to the other "stuffing agents".

The Amberlite modification reduced the average pore size of Daramic from 95 nm to less than 60 nm. This increased its area resistance by six-fold, but reduced diffusivity and electrolyte uptake.[44,45] The composite membrane was cycled at 20 mA cm^{-2} and gave a CE, VE, and EE of 94, 90, and 85, respectively. Increasing the current density to 80 mA cm^{-2} caused the efficiencies to decrease to 97%, 63%, and 62% respectively. At a higher current density, CE increases due to shorter time between cycles and reflects a commonly seen trend. The large decrease in VE at a higher current density reduced the EE by 23%. The low VE reflects low proton conductivity, an effect of no ion exchange groups being present. The membrane showed satisfactory durability, lasting over 700 cycles with little capacity decay.[61,62]

Cationic functionalization of Daramic was evaluated using two different sulfonation methods.[43,63] In the first method, DVB crosslinked Daramic was sulfonated by sulfuric acid giving IECs as high as 2.0 and a pore size of 20 nm. The second method used PSS stuffed membranes. Overall, sulfonation had a minimal effect on EE, however, water transport from one half-cell to the other was reduced by over an order of

magnitude. This is a great example demonstrating the importance of ion exchange groups on mitigating water transport for porous separators; a topic that is not often reported or overlooked.

Another investigation on Daramic composites separators embedded Nafion into the pore.[64] These Nafion impregnated separators showed decreased water uptake and increased cell resistance due to reduced sulfuric acid uptake in the membrane. This type of stuffing showed little potential based on poor results.

In summary, Daramic was functionalized with different polymers by stuffing, embedding, or grafting. These membranes showed the largest EE improvement by simply reducing the pore size from 100 nm to below 60 nm.[65] Studies highlighted that IEC and charge have a dramatic effect on water transport and crossover in the battery. One example showed the addition of cation exchange groups to a Daramic membrane with 20 nm pores could minimize water transfer without effecting EE. This initial work showed promising results, but the membranes were still lackluster compared to Nafion.

1.3.2 Polybenzimidazole porous membranes

Recent studies using porous polybenzimidazole (PBI) membranes have shown high EE and chemical durability, comparable to Nafion. PBIs excellent chemical and thermal stability have been utilized in other applications such as high temperature PEMFCs.[66,67] The polymer shown in Figure 1-4, can be readily synthesized by condensation polymerization. It can be further doped with many different acids due to the basic nature of the benzimidazole ring (pK_a ~5.5) which allocates ion exchange groups onto the polymer.[68]

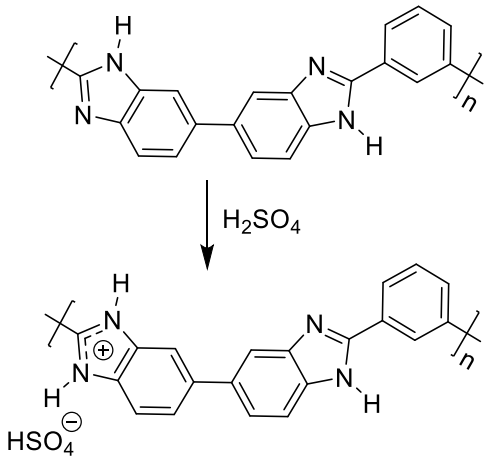

Figure 1-4 PBI polymer protonated in the presence of a strong acid

-Porogen extraction membrane fabrication

Porous PBI has been fabricated using an array of procedures that led to different and unique morphologies. Porous PBI with readily tunable morphologies was prepared by using a leaching method to extract dibutyl phthalate (DBP) in one study or polyethylene glycol (PEG) (M_n = 400) in another. Membranes prepared using DBP porogen (between 100-300%) were quaternized in acid. The amount of porogen affected morphology, pore size, and pore connectivity as shown in Figure 1-5. The pore size observed in the cross section SEM was large, around 5-10 μm, while top layer had smaller pores not detectable by SEM.

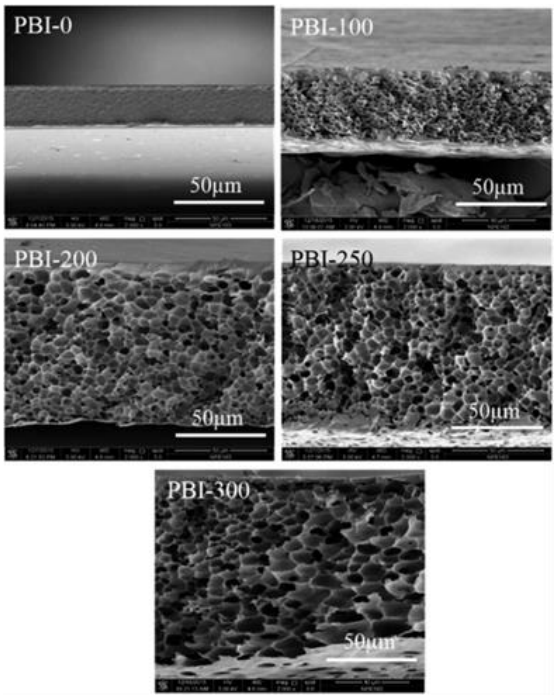

Figure 1-5 SEM images of the cross sections of the dense and the asymmetric PBI membranes

Pore size had a linear relationship with membrane resistance were the larger pores had lower resistance from increased acid uptake. Regardless of pore size, vanadium permeability remained over two orders of magnitude lower than Nafion 211. Pore size has a small effect on CE but a large effect on VE. PBI, and Nafion 211 were cycled 50 times at 100 mA cm^{-2} and exhibited stable performance with EE of 92.4 and 73.4% respectively. The PBI membranes showed an increased capacity decay with increased porosity where up to 92.0% of its capacity was retained after 20 cycles while Nafion retained only 73.2%.

Moon *et al.* used PEG porogen to prepare porous PBI membranes with pore sizes 98 – 21 nm.[47] These membranes experience similar changes in permeability and conductivity with changing pore size as the previous PBI membranes. The EE at 40 mA cm^{-2} increased from 47.9% to 78.2% as pore size decreased. PBI with 21 nm pores had a

CE of 99.4% and an EE of 78.2% while Nafion 117 had an EE 78.9% under the same conditions. Capacity decay of PBI with 21 nm pores and Nafion were 0.27% and 0.58% per cycle respectively. Again, the cationic and porous structure of PBI membranes gave very high CE for quaternized pores that are 10s of nanometer wide.

-Commercial PBI membranes

Zhou *et al*. soaked commercially available PBI membrane with nearly no pores in 4 M H_2SO_4 for 1 week.[46] The authors speculated that this treatment gave pores a few nanometers in diameter but no direct evidence was shown to prove this claim. Vanadium ion permeability was examined using VO^{2+} were PBI had at least two orders of magnitude lower permeability than Nafion. However, the PBI membrane has significantly lower proton conductivity than Nafion 211 at 15.8 and 50.7 mS cm^{-1} respectively. The PBI membrane gave a CE over 99% when cycled at 20-80 mA cm^{-2}, but its lower VE led to an EE below Nafion.

-Phase inversion casting

Lou *et al*. also analyzed PBI porous membranes by testing three different cast methods creating a large contrast in membrane morphology.[48] Membranes were prepared by: 1) traditional solvent casting, 2) non-solvent induced phase separation (NIPS) named n-PBI, and 3) water vapor induced phase separation (VIPS) named p-PBI. All membranes were soaked in H_2SO_4 solution for 24 h before characterization. The p-PBI membrane had pores ~2 microns in diameter free of macroscopic voids. SEM images of the p-PBI membrane are shown in Figure 1-6 and show different structural features than the porogen extracted membranes in Figure 1-5, for example p-PBI is more uniform and possesses pores with a smaller diameter.

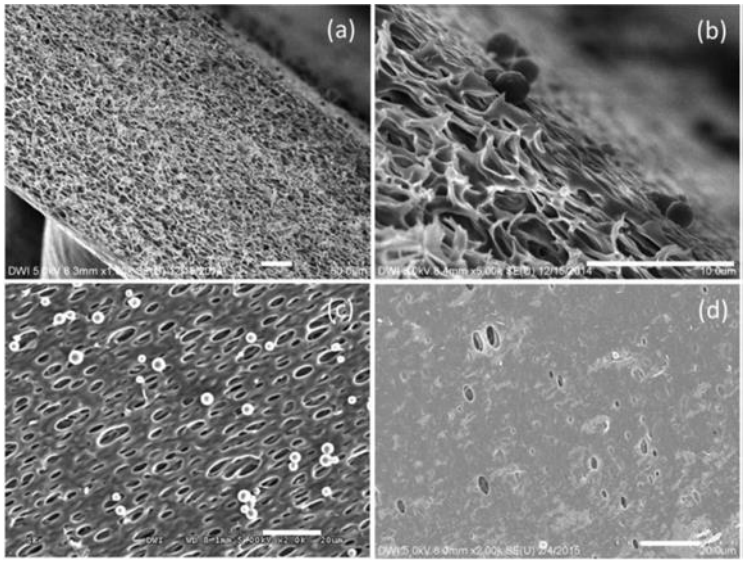

Figure 1-6 Morphology of the p-PBI membrane. (a) Membrane cross section featuring macropores, (b) cross section near membrane surface facing water vapour during preparation, (c) membrane surface facing water vapour during preparation, (d) membrane surface facing glass plate during preparation. Scale bars indicate 20 μm for (c) and (d)

The p-PBI membrane had a smaller pore size giving it lower conductivity but higher selectivity than membranes prepared using the other casting methods. At 50 mA cm^{-2}, p-PBI showed a CE of ~98% and an EE of 84%, 4% higher than Nafion 112.

Wessling et al. fabricated porous PBI membranes with top-tier EE that were stable over 13,000 cycles.[69] The cross section showed a uniform spongy structure with micron sized pores and a surface having smaller pores. At 80 mA cm^{-2} PBI had a CE of 98.87% and EE of 90.11% compared to Nafion's EE of 82%. This is the highest reported value in the literature per the author. Cycling over 13,000 times from 80-120 mA cm^{-2} showed little drop in efficiency. The authors note this is well over the benchmark of 4000 deep cycles targeted for commercial applications. Overall, this study clearly presented a nanoporous membrane showing higher EE and capacity decay than Nafion while showing stability over 13,000 cycles.

Overall porous PBI is promising as a VRFB separator with an EE higher than Nafion at high current density. PBI's innate ability to become charged at low pH can increase performance by the Donnan exclusion principle. Thus, controlled membrane fabrication combined with ion exchange groups gives nanosized pores that are selectively lined with quatarnized groups. This leads to high conductivity from the relatively large pores uptaking electrolyte and high ion selectivity from the quatarnized groups.

1.3.3 Porous PSU-SPEEK Membranes

Aromatic polymers such as PSU and PEEK are good candidates for alternative separators as noted in an earlier section, and are readily available or can be polymerized by simple condensation polymerization. PEEK can be sulfonated with high conversion and control to give SPEEK shown in Figure 1-7.

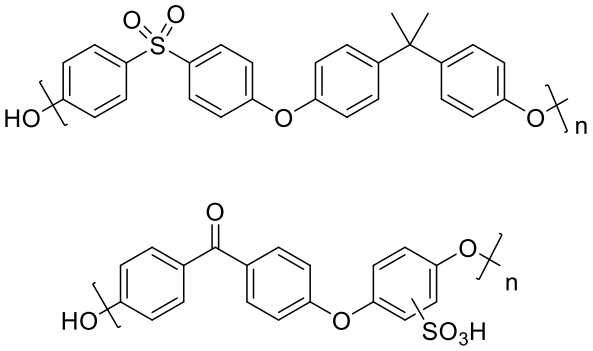

Figure 1-7 Top = PSU, and bottom = SPEEK.

The two polymers consist of rigid aromatic backbones responsible for their great physical and chemical properties. These polymers have limited solubility in common organic solvents, but certain polar aprotic solvents can dissolve both polymers, necessary for membrane preparation. The following section uses this polymer system to fabricate membranes by phase inversion casting. These polymers require a "quick" membrane

fabrication step to minimize macroscopic phase separation of the hydrophobic PSU and hydrophilic SPEEK.

Li *et al.* used blends of PSU and SPEEK to make microporous membranes by doping THF in the casting solution and using NIPS fabrication.[70] The films were highly porous with large macrovoids in a spongy matrix which is common for this type of fabrication. A concentration gradient from THF evaporation during membrane formation gave different morphologies controlled by THF concentration. This scaffold was modified and adapted for use in VRFBs.[71] Porous membranes were also fabricated using a binary solvent system were a high boiling solvent was extracted after film formation. The porous membrane gave CE close to 99% and an EE around 85% at 80 mA cm^{-2}, higher than those of Nafion 115. Demonstrating how the fabrication of nanopores on common ion exchange polymers can improve performance in a VRFB.

Porous PSU:SPEEK porous membranes coupled with solvent responsive layer-by-layer (SR-LBL) assembly was used to functionalize the surface of the anionic porous membrane.[51] It is proposed here that this new SR-LBL method can turn on and off the pores allowing controlled uptake of ionomers by swelling of the membrane in different solvents. The ionic layers are formed using poly (diallyldimethylammonium chloride) (PDDA) as the cationic layer and poly (acrylic acid) (PAA) as the anionic layer. After SR-LBL each of these membranes has an anionic surface of 3, 5, and 7 bilayers.

Cross-section SEM images showed spongy structures with 100-200 nm pores, not affected by SR-LBL. The Hagen-Poiseuille equation and water flux was used to characterize the membrane porosity and showed 10 nm pores before SR-LBL functionalization and 3-6 nm after. The pore size from this measurement might more

accurately reflect the effective pore size since the surface layer and cross section of the membrane are different.

Each bilayer assembled increased the area resistance while decreasing the VO^{2+} permeability. The decreased resistance is due to a smaller pore size up-taking less acid solution. Each bilayer showed an increase in CE and EE with a slight decrease in VE were the 7-layered membrane gave the highest EE at ~84% at 80 mA cm^{-2}. Decreasing pore size while increasing local pore IEC resulted in increased CE from smaller pores with slightly decreased VE.

The SR-LBL method was further studied to understand how surface charge effects the above membranes.[52] A PSU:SPEEK membrane with a cationic outer layer of PDDA was compared to its PAA equivalent. The cationic membrane showed lower permeability than the anionic membrane despite the area resistance remaining nearly the same. This agrees with the Donnan exclusion principle seen in AEMs. Cycling over the current densities of 80-180 mA cm^{-2}, the cationic surface showed higher CE, VE, and EE than the anionic surface; this difference is shown in Figure 1-8.

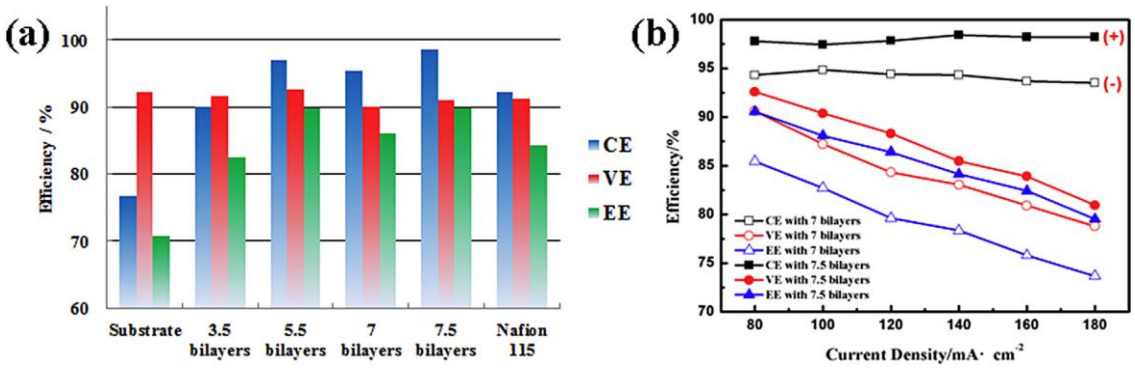

Figure 1-8 (a) VFB performance of the single cell with Nafion 115 or porous membranes with different PE layers; (b) VFB performance of single cell with porous membranes with different charged Pes at various current densities.[52]

At 80 mA cm^{-2} the cationic membrane had an EE of 88% compared to roughly 84% for Nafion 115. This experiment sheds light on how porous membranes can be ionized for improved performance.

Zhang *et al.* modified PSU:SPEEK blend porous separators by *in-situ* polymerization in the porous scaffold to incorporate polypyrrole. This modification reduced the pore size on the surface layer while the cross section shows a similar structure. Polypyrrole modification increased the CE from 87.2% to 96.3% while slightly decreasing the VE from 91.87% to 90.55% at 80 mA cm^{-2}. This trade off in efficiencies resulted in a net increase in EE to 80.16% to 87.20%, higher than Nafion 115's EE of 82.29%.

This PSU:SPEEK polymer system was used for VIPS to give blend membranes with different morphology than the previously outlined membranes which used NIPS.[54] These membranes had nanopores and performed well, without having to have an additional chemistry applied to PSU:SPEEK system. This agrees with the previous PBI membrane results where VIPS gave more efficient membranes for VRFB than NIPS.

1.3.4 Porous Polyacrylonitrile

Commercially available polyacrylonitrile (PAN) ultrafiltration (UF) membranes, were coated with PIM-1 (polymer of intrinsic microporosity 1), an inherently microporous polymer having a pore diameter less than 2 nm, shown in Figure 1-9.[55] The thin coating (750 nm) improved VO^{2+} permeation and prevented any detectable crossover of vanadium after 1 week due to exceptionally high selectivity. Further, an EE of 98.7% was reported at 1 mA cm^{-2} due to no vanadium ion crossover. The authors contribute this extremely high proton selectivity to the small pore size from PIM-1 and hydrophobicity of their composite material.

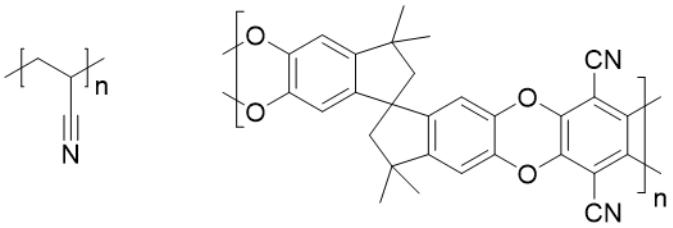

Figure 1-9 Chemical structure of PAN (left) and PIM-1 (right)

This approach is unique and offers a truly size exclusion approach to minimize vanadyl crossover.

Other PAN membranes are prepared by a standard phase inversion method to give microporous membranes.[56] After casting, membranes were hydrolyzed in base to increase hydrophilicity and give selective placement of ion exchange groups. At 80 mA cm^{-2} the NF membranes showed a CE of 95% and an EE of 76%, comparable to Nafion. By changing the hydrophilicity of the pore improved the EE of the battery.

1.3.5 Porous Polysulfone

Xiang *et al*. blended polyvinylpyrrolidone (PVP), a nonionic polyamide, into a PSU nanoporous membrane.[57] PVP contains a lactam ring that can be protonated or even

hydrolyzed under acidic condition, increasing the IEC along the pores. Dosing 40-70% PVP into membranes gave thin membranes (35 μm) with better selectivity than Nafion 212 (51 μm) despite being thinner. The PSU membrane showed over 2 orders of magnitude lower permeation of VO^{2+} than Nafion.

Its morphology was analyzed by TEM which showed hydrophilic channels to be around 2 nm, half the size of the Nafion 212 channels. Cycling showed the membrane had a much higher EE than Nafion 212 at current densities up to 80 mA cm^{-2} with a CE of 97%, VE of 88% and EE of 85%.

Zhang *et al.* produced nanoporous polysulfone membranes with no charge carrier having high EE in VRFBs.[72] Spongy membranes with pores less than 100 nm in diameter were soaked in isopropanol (IPA) and dried for an allocated amount of time. This drying process shrinks the membrane pores, making the sponge denser as shown in Figure 1-10.

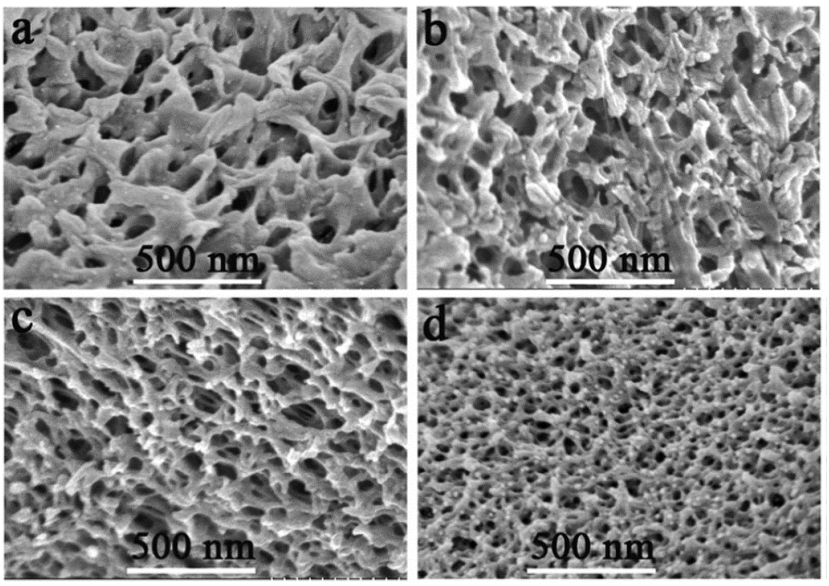

Figure 1-10 The cross-section morphology of M20 before and after evaporating the solvent at different times (a) M20, (b) M20-0, (c) M20-0.5, and (d) M20-24. The resulting membranes are referred to as MX-t, where X is the PVP/(PES + PVP) mass ratio in the casting

Despite a large shrinking the pore size, the resistance only changed slightly. However, vanadium crossover decreased substantially with decreased pore size. Overall the membranes all have relatively large nanopores that still effectively minimize vanadium crossover.

1.3.5 Other membranes

Polyvinylidene fluoride (PVDF) membranes with pores on the order of tens of nanometers showed impressive durability with excellent EE.[58] The PVDF membrane was cycled over 1000 times at 80 mA cm^{-2} where it maintained a CE over 95% demonstrating excellent chemical stability. Interestingly, the authors then subjected the membrane to a dehydrofluorination procedure to make the pores more hydrophilic. After the reaction, the membrane was found to have increased permeability to both H^+ and VO^{2+} ions causing drop in CE from 95% to 83%. These results demonstrated that the hydrophobic

nature of the pore caused hydrated vanadium ions to resist crossover due to high surface tension.

1.3.6 Porous Membrane Conclusion

The above membranes demonstrated the promising utility of simple porous separators in VRFBs. Membranes with differing pore size, morphology, surface charge, and hydrophilicity have shown a range of possibilities that led to high performance membranes from readily available precursors. Porous PBI membranes with both a premade porous structure and positively charged pore surfaces generated a great combination of high proton conductivity and low vanadyl crossover. Membranes with EE over 90% at high current density were cycled over 10,000 times. These recent breakthroughs could bring porous separators towards the forefront of alternative membrane separators for VRFBs.

1.4 Block Copolymer Porous Membranes

Polymers made of two or more monomers are referred to as copolymers. Copolymers are designed to have different microstructures and polymer architecture, which lead enormously different materials properties. For example, 3 common arrangements can occur for linear copolymers using a two-monomer system, using monomers termed A monomer and B monomer:

1. Random: AABBABABABBAAABAABBB
2. Alternating: ABABABABABABABABABAB
3. Block: AAAAAAAAAABBBBBBBBBB

Herein the interest is in block copolymers. Much of this attraction is because of their intrinsic ability to self-assemble in nanometer length scale due to block

incompatibility. Self-assembly of simple diblock systems has been studied since the 1960s and is well understood.[73,74] Common morphologies achieved in a model diblock copolymer are shown in Figure 1-11.

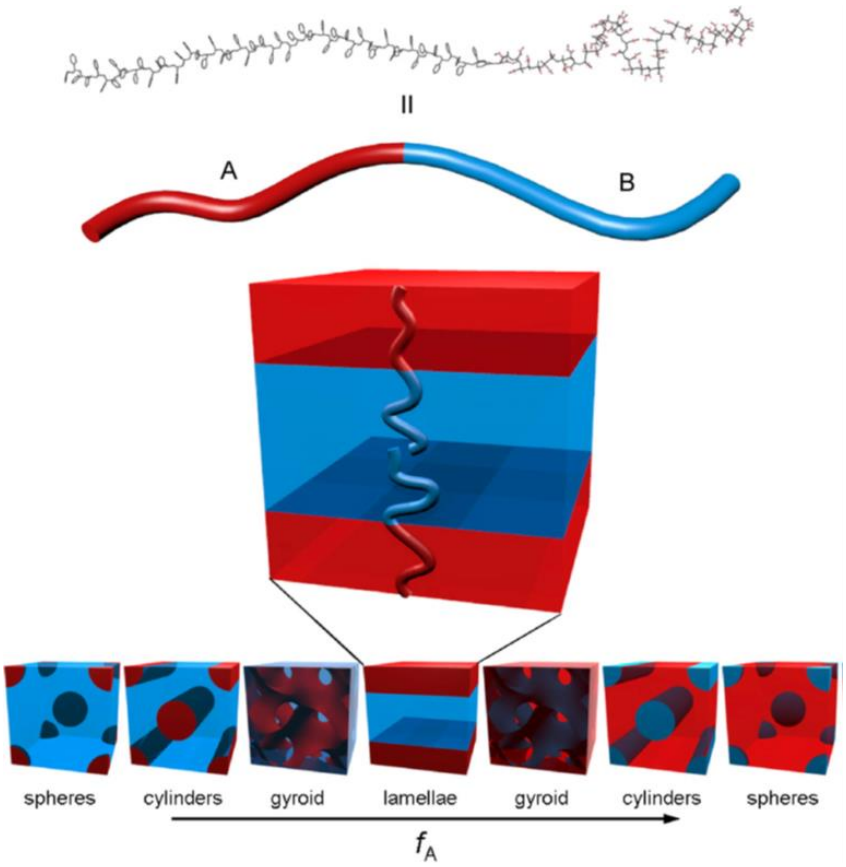

Figure 1-11 Schematic of thermodynamically stable diblock copolymer phases. The A–B diblock copolymer, such as the PS-b-PMMA molecule represented at the top, is depicted as a simple two-color chain for simplicity. The chains self-organize such that contact between the immiscible blocks is minimized, with the structure determined primarily by the relative lengths of the two polymer blocks (f_A).[70]

The volume fraction of the two blocks can be tailored to induce different morphologies such as body-centered-cubic spheres, hexagonally packed cylinders, bicontinuous gyroids, and lamellar. This self-assembly process is driven by an unfavorable mixing enthalpy coupled with a small mixing entropy.[75] Three parameters drive microphase separation in a model two block system: 1) the volume fractions of the A and B blocks

such that $f_A + f_B = 1$, 2) the total degree of polymerization, N ($N = N_A + N_B$), and 3) the Flory-Huggins interaction parameter, χ_{AB}.[76] The χ parameter is based on the thermodynamics of polymer mixing and specifies the degree of incompatibility between the A and B blocks. The relationship of χ and temperature is given below.

$$\chi_{AB} = \left(\frac{z}{k_B T}\right)[\epsilon_{AB} - \frac{1}{2}(\epsilon_{AA} + \epsilon_{BB})]$$

where z is the number of nearest neighbors per repeat unit in the polymer, k_B is the Boltzman constant, k_BT is the thermal energy, and ε_{AB}, ε_{AA}, and ε_{BB} are the interaction energies per repeat unit of A–B, A–A, and B–B, respectively. For example, polystyrene-*b*-polyisoprene has no strong secondary interactions such as hydrogen bonding and has a small positive χ_{AB}.

In equation 1, χ_{AB} is inversely proportional to temperature. At a specific temperature, χN determines the actual separation of a polymer system. Numerous morphologies are possible depending on how the system is optimized using aforementioned variables. If a block copolymer system gains further layers of complexity such as an additional block or different topology, then it affects the polymer morphology as well.

1.4.1 Degradable Component Block Copolymers

Among tremendous potentials of block copolymers in various applications, an example of the creative potential is the production of nanoporous membranes. Incorporating a selectively degradable block into a block copolymer and removing the degradable block after the tailored morphology is achieved give controlled nanoporous membranes. The pioneering work on this method was published in 1988 and has spurred related work for more than 2 decades.[77-79] Different degradable blocks have been used

such as polydienes, polymethylmethacrylate, polylactide, and others that can be selectively removed by hydrolysis, ozonolysis, pyrolysis, etc. There are two key requirements for preparing nanoporous materials from self-assembled block copolymers: 1) the removable material must be physically accessible to the solvent or reagent used for degradation, 2) the matrix material must be able to support the resultant nanoporous structure.[78,80]

Of the many degradation procedures, hydrolysis of polyesters works with flexible conditions and straightforward. Over the last 15 years Hillmyer *et al.* established the incorporation of a polylactide (PLA) block into block copolymers for selective degradation.[78,80,81] This method was applied to many block copolymers, where one system exhaustively studied was polystyrene-polylactide (PS-PLA). Phase separation for PS-PLA has been reported: 1) under different annealing conditions, 2) using different polymer topology, 3) incorporating additional comonomers, and 4) with different N and *f* of the matrix block.[81-85]

1.4.2 PLA Degradable Polymers

Early work on PS-PLA block copolymers established PLA selective hydrolysis in mild alkaline conditions.[82,83] Different f_{PLA} with different total degrees of polymerization (N) were examined before and after hydrolysis. A change in f_{PLA} from 0.13 → 0.55 resulted in changing morphologies from disordered, cylinder, gyroid, and to lamellae as shown in Figure 1-12. SEM images of nanoporous PS with cylindrical morphology show uniform structures that remain unharmed after PLA degradation.

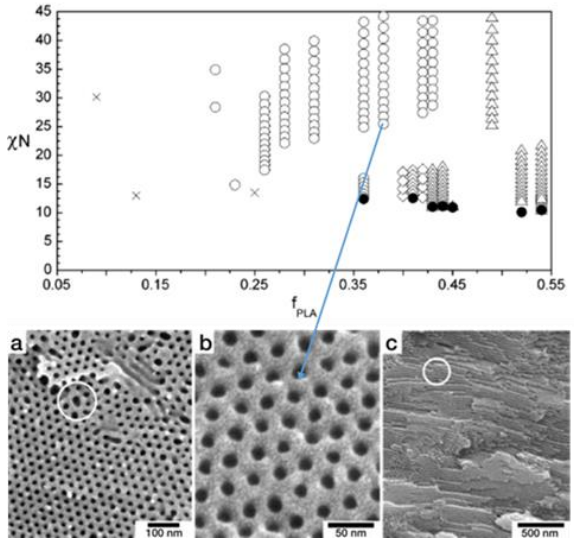

Figure 1-12 Top) Experimental PS-PLA morphology diagram. Morphologies were determined from SAXS at different temperatures (circles) cylinders, (diamonds) gyroid, (triangles) lamellae and crosses (disordered) with solid circles indicating order-disorder transitions temperature. Bottom) SEM images of nanoporous PS from monolithic PS-PLA (f_{PLA} = 0.37, N = 307) precursors. a and b perpendicular to the pore axes c parallel to the pore axes.

Incorporation of PLA on many other systems is summarized below in Table 1-3. This table describes different copolymer systems and polymer architectures used to produce an array of nanoporous materials through PLA degradation.

PS nanoporous materials can be coupled with other fabrication methods to add another layer of functionality.[86] This method gave submicron sized pores combined with nanopores after PLA etching shown in Figure 1-13. The PLA macroinitiator is used to polymerize styrene (S) and divinylbenzene (DVB) in the presence of PEO (30-70%). Although PEO is miscible with S and DVB monomers, the high volume of PEO macroscopically separates from the *in situ* formed PLA-b-P(S-co-DVB), yielding macrophase domains on the order of hundreds of nanometers. Etching this material in basic solution extracted out both PEO and PLA, leaving a crosslinked PS scaffold. SAXS

and SEM were used to confirm the presence of smaller domains (SAXS) being distributed throughout the material.

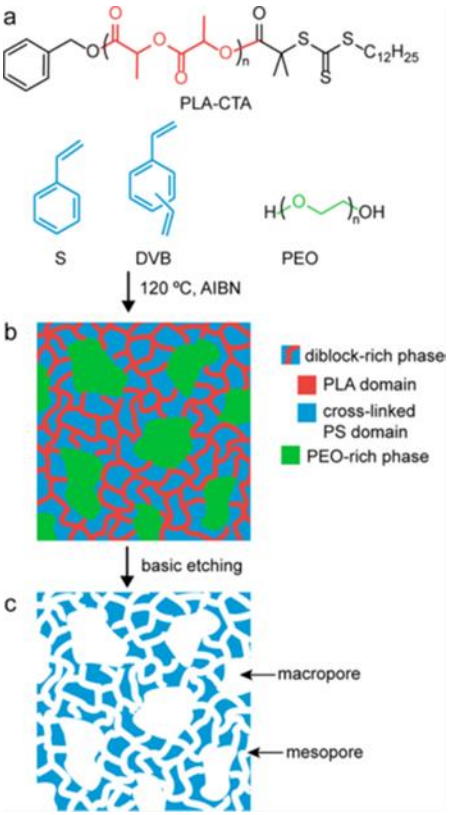

Figure 1-13 Preparation of hierarchically porous membranes using PEO additive.

Selectively degradable block copolymers have also been adapted to inorganic materials. Hillmyer *et al.* used poly(dimethylsiloxane) (PDMS) to synthesize copolymers with PLA, and degradation pf PLA left a porous PDMS scaffold.[87-89] PLA-PDMS-PLA block copolymers with low molecular weight PLA (1.6-9.5 kDa blocks) gave a cylindrical morphology verified by SAXS and SEM. The copolymer has a high $\chi_{PLA\text{-}PDMS}$ of 0.94, that means the blocks are highly incompatible, capable of strong phase separation at low *N*. Using solvent annealing, sub-20 nm domains were fabricated and etched to give an inorganic template that is promising for microelectronic applications.

1.5 Prelude

Inspired by urgent energy concern and the literature work on polymeric separators described in Chapter 1, this dissertation research studies the relationship on of structure-property-performance of the PSU-based tailor-made membranes for VRFB application.

The coming chapters use two different types of separators to evaluate structure-property relationships in a VRFB: 1) Non-perfluorinated PEMs and 2) nanoporous membranes. In chapter 2, the polymer structure in non-perfluorinated PEMs was modified by incorporating different side chains between the polymer backbone and sulfonic acid moiety. The modified PEMs showed appreciable changes in membranes properties and energy efficiencies.

Chapters 3-5 describe the systematic study of pore size and morphology in porous membrane separators for VRFBs. A novel method was developed which controlled pore size and morphology and was used to prepare different membranes series for battery evaluation. Different pore modifications were employed to change hydrophilicity, charge, and so forth, to selectively functionalize the membrane pores. The pore modifications affected to the membrane properties in various ways, which would be promising for next generation polymeric separators.

Table 1-3 Reference compilation of block copolymers utilizing PLA as a degradable block for nanoporous substrate fabrication

Ref	Polymer system	Polymer Architecture	Membrane Fabrication	f_{PLA}	Structure [b]	Special conditions	Additional information
[82,83]	PS-PLA	Linear diblock copolymer	Pressed and/or sheared	0.09-0.55	Dis, C, G, L	Sheared for alignment of the domains	Clean and oriented cylinder
[90]	PCHE-PLA	Linear diblock copolymer	Pressed and/or sheared	0.14-0.40 + 0.74	All C, except f_{PLA} = 0.74 gave L	Similar to PS-PLA, but PS was reduced prior to PLA polymerization	X is approximately 3 times that of PS-PLA meaning stronger segregation
[91]	PS-PLA blend with PS-PEO	Blend of linear diblock membranes	Drop cast		C	Using AB/AC blend polymers (B and C are miscible and one is PLA).	After hydrolysis, the water compatibility was much higher than plain PS-PLA nanoporous membranes
[92]	PS-PLA	Linear diblock copolymer	Drop cast		C, L	Used base hydrolysis and oxygen reactive etching	Prepare PS-PLA with perpendicular cylinders onto different substrates
[93]	PS-PDMA-PLA	ABC linear triblock terpolymers		0.17-0.30	C, L	Used acid to cleave PDMA amide bonds	f_{PS} b/t 0.66 – 0.79 = C and b/t 0.56-0.64 =L. base hydrolysis left PDMA brushes in the pore for later functionalization.
[94]	PS-PI-PLA	ABC linear triblock terpolymers		0.19-.038	Dis, C, L	Membranes showed tough resistant to base hydrolysis, it was attributed to hydrophobicity.	Epoxidize up to 80% of PI block after PLA etching. Possible loss of pore alignment during epoxide functionalization

Ref	Polymer system	Polymer Architecture	Membrane Fabrication	f_{PLA}	Structure [b]	Special conditions	Additional information
[95]	PS-PLA or PS-PEO	Linear diblock and blends			G		Target gyroid phase to give - bicontinuous nano-template after hydrolysis of PLA
[96]	PLA-PDMA-PS	ABC linear triblock terpolymers	Pressed in apparatus for filtration		C		Used as ultrafiltration membranes for gas and liquid separations.
[97]	PI-PLA	Linear diblock copolymer				Use chloroform for vapor annealing	Control orientations of the of the cylinders depending on how films are annealed
[98,99]	PLA-P(N-S)	Block copolymer	Drop cast then hot pressed	0.39-0.49	C, L, C + L	Metathesis reaction for crosslinking	Crosslinking improved mechanical properties significantly.
[100]	PFS-PLA	Linear diblock copolymer				Cylinders aligned via electric field	Cast onto gold coated silicon. After etching PLA, cylinders filled with copper oxide. Removal of PFS left freestanding nanowires
[101]	P3AT-PLA	Linear diblock copolymer	Spin- cast		C, L		P3AT is a semiconducting and films had high degrees of crystallinity

Ref	Polymer system	Polymer Architecture	Membrane Fabrication	f_{PLA}	Structure [b]	Special conditions	Additional information
[102]	PS-PLA	Linear diblock copolymer				polymers are cast onto a microporous membrane for support	By controlling the solvent evaporation rate, the orientation of the PLA cylinders could be controlled. After etching, PEO filtration was low for low M_n PEO, near 100% for 100 kDa PEO
[103]	PLA	ABA triblock copolymer			C	ROMP used for bifunctional B block	Membranes had high chemical resistance in acid solution.
[104]	PS-PLA	Bottlebrush copolymer, high M_n, > 1,000 kDa	sheared		C		TEM showed PLA diameters of 47 ± 8 nm. Very low order in cylinder spacing via SEM. Pore size was 55 nm after etching.
[105]	PS-PLA	Linear diblock copolymer			C		Changed the interface of the 2 blocks by replacing with sulfonyl group. After hydrolysis pore was lined with sulfonic acid moiety from block interface.
[106]	$(PS)_2$-PLA	Three-arm star architecture			C, L		Gave C morphology at f_{PLA} gave lamellae for the corresponding linear diblock copolymer
[107]	PS-PI-PS-PLA	ABAC tetrablock terpolymer	Spin coating	0.2-0.25	C, L	Cast onto a PSU microporous support	Pore sizes were 15 nm in diameter. Tested against an aqueous solution for dye filtration, rejecting 97% of the dye.

[a] polymer abbreviations, PCHE = poly(cyclohexylethylene), PEO = polyethylene oxide, PDMA = polydimethylacrylamide, PI = polyisoprene, P(N-S) = poly(norbornenylethylstyrene-styrene) copolymer, PFS = poly(4-fluorostyrene), P3AT = poly(3-alkylthiophene), PEO = poly(ethylene oxide), PE = polyethylene,
[b] Dis = disordered, C = cylinder, G = gyroid, L = lamellae

Chapter 2

Effects of Sulfonated Side Chains Used in Polysulfone Based PEMs for VRFB Separator

Although sulfonated hydrocarbon polymers have been extensively studied for PEM applications, only few systematic studies to directly compare different side chains in VRFB have been reported. This chapter describes the first approach of this research towards understanding of structure-property-performance relationship of PEMs in the VRFB system. The polymers incorporate different types of sulfonated side chains to improve self-assembly in the membranes. Properties and performance of side chain modified PEMs as a VRFB membrane separator are evaluated comparing with backbone sulfonated analogs to correlate their structure with those results.

2.1 Introduction

Demand for devices capable of large scale energy storage has heightened as a result from the continuous growth of alternative energy and the need to store it. Redox flow batteries (RFB) have emerged as an option for grid-scale energy storage in view of their energy efficiency, rapid response to varying loads, durability shown in lengthy charge/discharge cycles and reasonable costs.[3] The all-vanadium redox flow battery (VRFB) in particular has drawn the most attention since its use of four vanadium species as redox couples allows for potential to minimize upkeep cost, as reflected by its many demonstration plants worldwide.[110] VRFBs utilize a central cell (or cell stack) containing an ion exchange membrane which separates two electrolyte solutions containing a mixture of V(IV)/V(V) and V(II)/V(III) in the positive and negative compartments, respectively. These solutions are circulated through the cell where a redox reaction

occurs; allowing electrons to travel from the negative to the positive electrodes through an external circuit during discharge while the proton exchange membrane (PEM) allows for transport of ions to maintain charge balance (while both PEMs and anion exchange membranes have been used in RFBs,[111,112] we focus here upon the former). The PEM also acts as a barrier material partly preventing crossover that could lead to side reactions and lower the energy efficiency of the battery. RFB efficiency is greatly dependent on the PEM. For baseline measurements, the most commonly used membrane at present is Nafion®. Despite its adequate performance, its high cost and modest ion selectivity have driven research aimed at identifying better performing, more cost-effective alternatives. Hydrocarbon based polymeric materials, e.g., sulfonated polyarylenes, have been studied for alternative PEMs over the past decades.[111-116] These hydrocarbon membranes are being sought after as a means of improving cost and performance in VRFB, while maintaining the chemical and mechanical integrity.

The selectivity of the membranes, that is their ability to perform as barriers with relatively free flow of protons, is considerably influenced by the morphology of these membranes. The hydrophilic sulfonic acid groups encourage uptake of water, which swells the membrane in wet/humid conditions. This results in the formation of nanosized pores through which protons can permeate. This phenomenon is typically seen, for example, in Nafion in which ca. 2 nm wide pores are present.[11,117] Numerous efforts have revolved around alternating the placement of sulfonic acid groups in a variety of ways as a means of creating nanostructures to further improve performance.[118-121] Nanoscale morphologies formed in block copolymers with hydrophilic and hydrophobic blocks yielded some degree of improvement in proton conductivity.[26] Another report showed

that clustering of the acid groups in random copolymers led to more defined nanostructures, promoting superior membrane performance.[122-124] PEMs with nanosize domains have been fabricated from polymers with sulfonic acid terminating side chains off the main backbone, ostensibly giving the sulfonic acids greater 'flexibility.[125-128]

Herein this work aims at studying structure-performance relationships of PEMs in VRFBs. Two monomers are synthesized containing different sulfonic acid side chains, followed by polymerization to develop partially fluorinated sulfonated polysulfone (PSU) random copolymers, which then are cast into ductile membranes. These membranes are analyzed comparatively followed by testing in a VRFB cell to investigate the effect of the different side chains. We compare a group of three sulfonated polysulfones containing different sulfonated 'spacer' groups off the backbone: sulfonic acid directly on the backbone (sb-PSU), one separated by an allyl group (as-PSU) and another separated by a styrenyl group (ss-PSU). These have been prepared with a narrow IEC range to discern changes in performance.

2.2 Experimental

2.2.1 Materials

4,4'-Difluorodiphenyl sulfone (DFDPS) and 4,4'-(hexafluoroisopropylidene)diphenol (bisphenol AF) were purchased from Oakwood Chemicals and recrystallized twice from toluene. Palladium(II) acetate, sodium diphenylphosphinobenzene-3-sulfonate (TPPMS), sodium p-styrenesulfonate hydrate, and sodium allylsulfonate were purchased from TCI. Decafluorobiphenyl was purchased from Sigma Aldrich. Dimethyl sulfoxide (DMSO) and toluene were distilled over

calcium hydride, and dimethylformamide (DMF) was purified by a Vacuum Atmospheres solvent purifier system. All other reagents were used as received.

2.2.2 Monomer Synthesis

Two novel monomers containing different sulfonated side chains were both prepared using a Mizoroki-Heck coupling reaction to give two new monomers with pendant acid side chains as shown in Figure 2-1. The precursor dbDFDPS used for the Heck reaction was synthesized as reported in literature.[126] This precursor was then coupled with one of two presulfonated vinyl reagents, either sodium p-styrenesulfonate hydrate or sodium allylsulfonate giving pure disulfonated products for both.

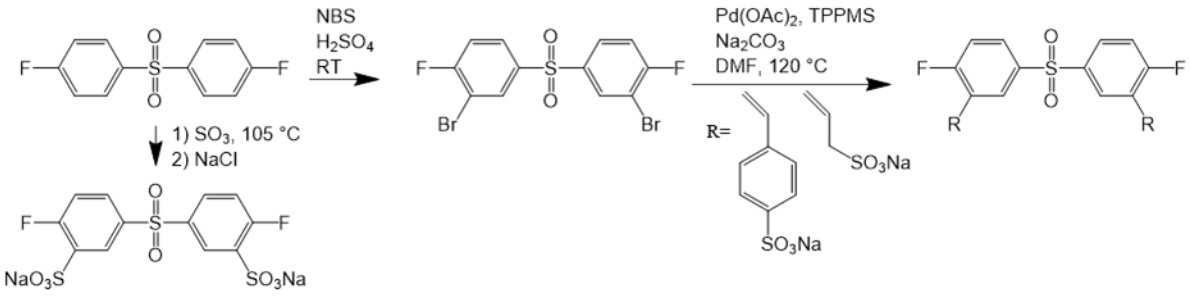

Figure 2-1 Monomer Synthesis

3,3'-Dibromo-4,4'-difluorodiphenyl sulfone (dbDFDPS): As a preliminary step to the coupling reaction to from the two acid-functionalized monomers, DFDPS was brominated as reported in the literature to yield dbDFDPS.[126] The details of the reaction are as follows: DFDPS (25 g, 98 mmols) was first dissolved in concentrated H_2SO_4 (160 mL). *N*-bromosuccinimide (40 g, 226 mmols) was added in 3 equal intervals to the flask over 30 minutes with vigorous stirring. After 6 h the reaction mixture was poured into 1 L of ice water and the precipitate was collected via Büchner filtration and washed multiple times with H_2O and hexanes (100 mL). The product was recrystallized three times from toluene to remove mono-reacted byproduct.

*Bis[4-fluoro-3-(4-vinylbenzenesulfonate)phenyl]sulfone disodium salt (**ss-DFDPS**):* To a 500 mL 3-neck round bottom flask equipped with nitrogen inlet and a condenser, dbDFDPS (8 g, 19.4 mmols), sodium p-styrenesulfonate (8.59 g, 41.7 mmols assuming 10% H_2O), palladium(II) acetate (0.262 g, 1.07 mmols), TPPMS (0.212 g, 0.582 mmols), sodium carbonate (8.23 g, 50 mmols) were charged into the flask. Dry DMF (170 mL) was added to the nitrogen flushed flask with stirring followed by heating at 120 °C for 12 h. DMF was then rotary evaporated, and the residual precipitate was dissolved in DMSO, filtered, precipitated into chloroform, and finally recrystallized from water/alcohol mixture to give the resulting trans isomer, ss-DFDPS (2.81 g, 35%). ^{1}H NMR: (499.7 MHz, DMSO-d6) δ 8.47 (dd, J = 6.9, 2.2 Hz, 2H), 8.00 (ddd, J = 8.9, 4.8, 2.4 Hz, 2H), 7.34 (d, J = 16.7 Hz, 2H), 7.53 (dd, J = 10.1, 8.9 Hz, 2H), 7.56 (d, J = 16.8 Hz, 2H), 7.64 (q, J = 7.8 Hz, 4H).

*Bis[4-fluoro-3-(prop-2-ene-1-sulfonate)phenyl]sulfone disodium salt (**as-DFDPS**)*: Using similar methodology to ss-DFDPS, sodium allylsulfonate (5.88 g, 40.8 mmol) was added in place of sodium p-styrenesulfonate. The same steps were followed to those in the similar reaction giving as-DFDPS (1.95 g,30%). ^{1}H NMR: (499.7 MHz, DMSO-d6) δ 8.22 (dd, J = 7.0, 2. Hz, 2H), 7.93 (ddd, J = 8.7, 4.6, 2.4 Hz, 2H), 7.44 (dd, J = 10.6, 8.8 Hz, 2H), 6.59 (dT, J = 15.6, 6.7 Hz, 2H), 6.55 (d, J = 16.1 Hz, 2H), 3.41 (d, J = 6.1 Hz, 4H).

*3,3'-Disulfonate-4,4'-difluorodiphenylsulfone disodium salt (**sb-DFDPS**)*: The monomer was synthesized according to the literature for a similar monomer.[129] DFDPS (6 g, 24 mmol) was dissolved in 17 mL of fuming sulfuric acid (20% SO_3). The reaction mixture was flushed with nitrogen then heated at 105 °C overnight. The crude product

was diluted with 60 mL of ice water and 15.5 g of NaCl was added with mild heating. After cooling, the precipitated crude product was collected by filtration. It was then redissolved in water and neutralized. The pure product was salted out by adding 15 g of NaCl with heating and cooling steps, and then collected and dried *in vacuo* before further polymerization.

2.2.3 Polymer Synthesis

Figure 2-2 shows the synthesis scheme for acid-functionalized polysulfones. All polymers were synthesized under the same reaction conditions, only changing the monomer feed ratio of sulfonated acid monomer.

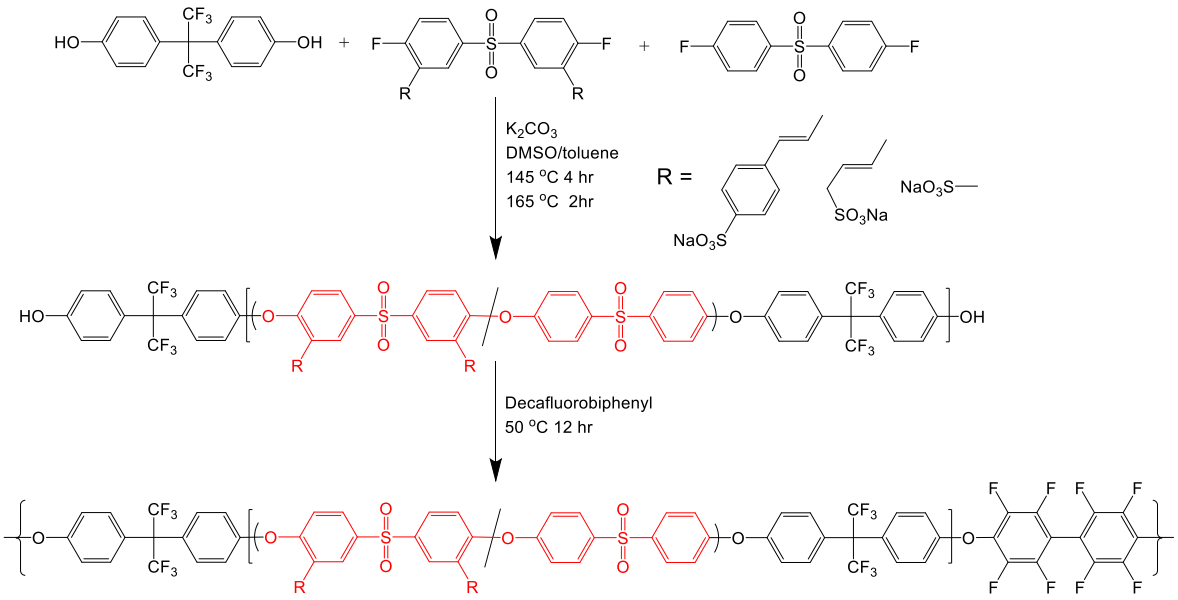

Figure 2-2 Synthesis of sulfonated side chain polymers by two step method.

Synthesized polysulfones and their membranes are referred to using the side group type and theoretical IEC value (Low, Medium, High) by monomer feed ratios as listed in Table 2-1. A typical polymerization is as follows: for the synthesis of ss-PSU-L, ss-DFDPS (0.745 g, 1.124 mmol), DFPDS (0.191 g, 0.749 mmol), bisphenol AF (0.700 g, 2.082 mmol), and potassium carbonate (0.36 g, 2.6 mmol) were loaded into a 50 mL 3-

neck flask equipped with a Dean-Stark, condenser, nitrogen inlet, and magnetic stirrer. The system was flushed with N_2 and dry DMSO (7 mL) and toluene (4.5 mL) were added. The reaction mixture was heated at 150 °C for 3 h then slowly heated to 180 °C for gradual removal of toluene. The vessel was then cooled to 55 °C after 3 h and decafluorobiphenyl (0.072 g, 0.214 mmol) was added with 7 mL of DMSO. After 12 h the reaction temperature was increased to 65 °C for 1 h and the viscous solution was precipitated into warm isopropyl alcohol, filtered, washed with hot water, and dried *in vacuo*.

2.2.4 Membrane formation

Each polymer was dissolved in DMSO (6-8 w/v%), centrifuged at 4500 rpm for 3 h to remove any insoluble impurities, cast onto a flat glass surface, and kept at 75 °C for 4-5 h. The cast plate was immersed in DI water to lift the membranes from the glass surface. The membranes were acidified in 1 M H_2SO_4 under reflux for 1 h followed by rinsing in boiled water for 1 h prior to any characterization.

Table 2-1 Acid-functionlized polysulfone synthesis

Series [a]	Acid side-group	Polymer ID (Membrane ID)	IEC Theoretical (meq g^{-1})	Feed ratio of sulfone monomers	
				Acid monomer (mol %)	DFPDS (mol %)
sb	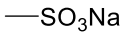	sb-PSU-L	1.45	50	50
		sb-PSU-M	1.62	57	43
		sb-PSU-H	1.77	63	37
as	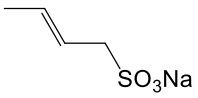	as-PSU-L	1.45	53	47
		as-PSU-M	1.62	61	39
		as-PSU-H	1.77	69	31
ss	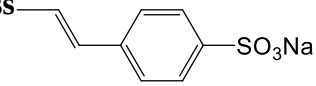	ss-PSU-L	1.45	60	40
		ss-PSU-M	1.62	70	30
		ss-PSU-H	1.77	80	20

[a] Abbreviations are defined as: sulfonated backbone (sb), allyl sulfonate (as), and styrenyl sulfonate (ss).

2.2.5 Characterization

^1H NMR: NMR spectra were obtained on a Varian 500 MHz spectrometer in DMSO-d_6 to confirm the chemical structure of monomers and polymers.

Conductivity: Acidified membranes were cut into 5 x 0.75 cm^2 strips and soaked in deionized water, acid solution (1 to 3.3 M H_2SO_4), or electrolyte solution (1.7 M vanadyl sulfate in 3.3 M H_2SO_4) for at least 24 h prior to measurements. The strips were removed from the soaking solution, patted to remove surface water, and immediately placed into the cell. The resistance was then measured on a Biologic sp-150 potentiostat using a 4 pt. closed wall cell of a design described elsewhere.[130] Proton conductivity was then calculated using the following equation:

$$\sigma = \frac{L}{R \times A}$$

Where σ is the conductivity, L is the length between electrodes, R is resistance, and A is the cross-sectional area.

Water uptake: The water uptake of the membranes in acid form was calculated by the weight loss from wet and dry samples using the equation shown below:

$$Water\ Uptake\ \% = \frac{W_{wet} - W_{dry}}{W_{dry}} \times 100\%$$

Where W_{wet} is the wet weight and W_{dry} is the dry weight. All samples were soaked in DI water for a minimum of 24 h then removed and excess water was patted off and quickly weighed to get W_{wet}. Samples were then dried in vacuum at 100 °C for 24 h then weighed to get W_{dry}.

IEC and hydration number: IEC was calculated by back-titration of the membranes in the acid form using membranes of known dry weight. Membranes were allowed to equilibrate in a known excess of base for 48 h, followed by titrating the excess base. Hydration number, λ, was calculated using the experimental IEC and wet and dry weights to calculate how many water molecules per SO_3H using the following equation where 18.02 is the mass of H_2O.

$$\lambda = \frac{(W_{wet} - W_{dry})/18.02}{IEC \times W_{dry}} \times 1000$$

Thermal analysis: All thermal measurements were performed using 1-3 mg of membrane in the acid form. Thermal Gravimetric Analysis (TGA) was done using TA Instruments Q50 under a nitrogen environment. Samples were first held at 150 °C for 1 h then ramped from 30 °C to 700 °C at a rate of 10 °C/min. Differential Scanning Calorimetry (DSC) curves were collected using TA Instruments Q20. Under nitrogen the sample was kept at 120 °C for 20 min then cycled from -40 °C to 270 °C four times at a heating rate of 10 °C/min after every rapid cooling run (ca. -50 °C/min).

VRFB cell cycling test: Synthesized membranes were tested in vanadium redox flow battery single cells to determine their performance as an electrolyte separator. Membrane samples with thickness around 50 μm were chosen to allow direct comparison with commercial standard Nafion 212 membrane. The electrolyte solutions were prepared by two step charging from raw electrolyte with 1.7 M vanadyl sulfate (99.9% alfa aesar) and 3.3 M sulfuric acid (96~98%, Fisher Scientific). The charged electrolyte solutions (50 mL) were placed on positive and negative sides respectively. The 5 cm^2 flow battery cell hardware with serpentine flow field was supplied by Fuel Cell Technologies Inc. A single layer of untreated SGL CP X-1 high surface area carbon paper compressed from 400 μm to 250 μm in thickness was used in each electrode. The electrolyte solutions were circulated between cell and reservoirs by a Masterflex peristaltic pump. A pair of cartridge heaters controlled by an Omega CSC32 temperature controller was installed in the battery cell to maintain a 30°C operation temperature of the cell. A current density of 200 $mA \cdot cm^{-2}$ was used during the cycling. The electrolyte flow rate was held at 50 $mL \cdot min^{-1}$ during cycling. To record the OCV decay, OCV was monitored across the battery cell after electrolytes were fully charged and the pump was stopped.

2.3 Results and Discussion

2.3.1 Monomer synthesis

The Heck coupling method gave nearly complete conversion with demonstrating both regio- and stereo-specific addition. The use of this coupling method, with its high conversion, allowed for relatively simple purification to remove excess sulfonated vinyl reagents. The structure of both monomers in the sodium salt form was confirmed by ^1H NMR as seen in Figure 2-3. The Heck reaction was found to be sensitive to the typical

bases; however, sodium carbonate gave little to no byproduct. Although high conversion was achieved, multiple recrystallizations were required to give high purity needed for polycondensation, that lowered the overall yield.

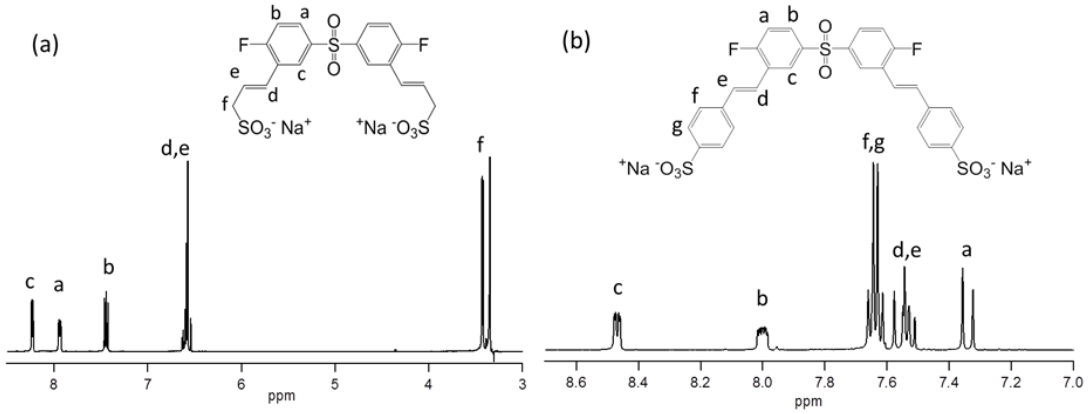

Figure 2-3 ^{1}H NMR spectra of (a) as-DFDPS and (b) ss-DFDPS.

2.3.2 Polymer synthesis

Acid-functionalized polysulfones were synthesized via a two-step process: (i) synthesis of stoichiometry-controlled prepolymers, followed by (ii) *in situ* coupling to yield high molecular weight polymers. This coupling approach using decafluorobiphenyl was necessary to fabricate robust membranes for VRFB application. The prepolymers were synthesized using a specific feed ratio to give an average degree of polymerization of 9 by stoichiometric excess of bisphenol AF. Actual degree of polymerization of the prepolymers calculated by the ^{1}H NMR spectrum in Figure 2-4a using the end group aromatic peak (peak 1 or 2) versus polymer backbone peaks revealed the molecular weight ranging from around 4000-6000 g/mol. A stoichiometric molar ratio of decafluorobiphenyl was then added at reduced temperature to couple the prepolymers, thereby maximizing molecular weight. Figure 2-4b shows a spectrum of the typical post-coupling polymer in which the loss of the end group peak at around 6.8 ppm can be seen.

Each of three types of acid polymers (sb-, as-, and ss-PSU) was synthesized with three different IECs: 1.45, 1.62, and 1.77. These theoretical IECs could be targeted by adjusting the feed ratio of acid- to nonacid- DFDPS monomer. Both as- and ss- side chains, gave polymers that were only soluble in DMSO and that were not soluble in other aprotic polar solvents such as DMF, *N*-methyl-2-pyrrolidone (NMP), and dimethylacetamide (DMAc).

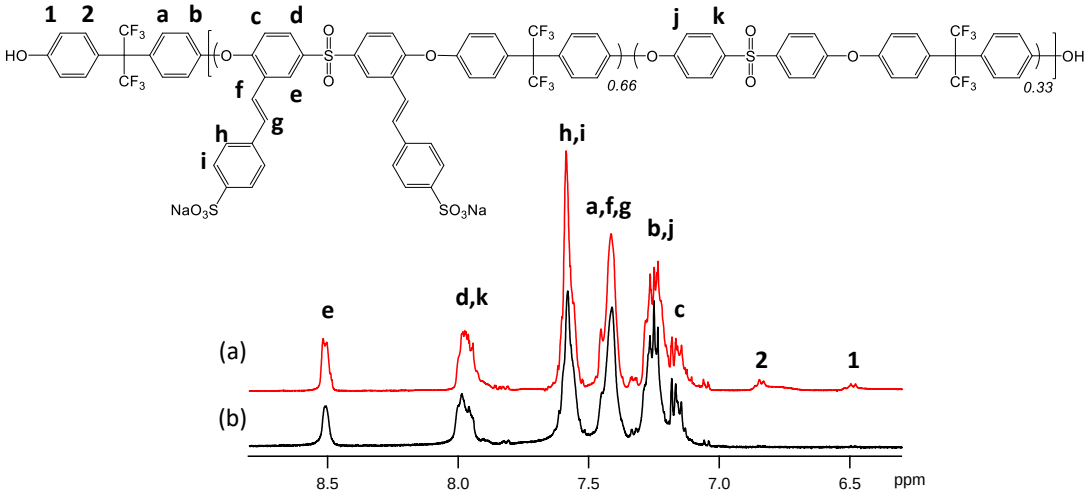

Figure 2-4 ^{1}H NMR spectra of (a) the prepolymer with a structure and (b) the post-coupling ss-PSU.

2.3.3 Membrane characterization

The thin membranes, typically 40 to 70 μm in thickness, were prepared by solvent casting of the synthesized polymers. Membranes were characterized as summarized in Table 2-2. Experimental IECs were measured through titration and exhibited trends consistent with the theoretical IEC calculated by the monomer feed ratio, although experimental values were lower than those derived from the monomer feed values (theoretical IEC).

The conductivity and water uptake tend to increase as IEC increases for PSU membranes for most of side chain types, expected as an effect of the sulfonic acid group. These data were the average of measurements repeated at least 3 times for multiple strips ($n > 6$) from each membrane. Measurements were taken after the membranes were immersed in water for more than 24 h and continuously up to 11 days for testing consistency and equilibrium state of the membranes. Figure 2-5 shows the conductivity data against water uptake to examine correlation of these two properties. This graph revealed that all types of side chain PSU membranes have a linear correlation with a slightly different slope for the linear regression curve. Although ss-PSU membranes displayed lower conductivity and water uptake in comparison with sb- and as-PSU membranes, the higher slope indicates that ss-PSU membranes may transfer ions more efficiently when all membranes take up the same water amount (if more than 42%). This slight difference could be explained by the membrane morphology. The polymer membrane with the longest side-chain (ss-PSU) may have more complete segregation of the hydrophilic ionic channel from the hydrophobic and robust polymer domain when compared to the membrane of direct sulfonation (sb-PSU), as depicted in Figure 2-6. Theoretically, longer side chains can promote more defined channels by allowing the sulfonic acid groups to aggregate, the basis for this work. While these basic data indicate a difference in bulk physical properties, more localized effects related to structure of the pores might be reflected in actual battery test conditions in which the membranes are exposed to concentrated solutions of electrolytes. In that situation, the pores may play a larger role in overall proton mobility and crossover of vanadium ions reflected in its various efficiencies.

Table 2-2 Properties of PSU membranes with different acid side chains

Side-chain	Membrane ID[a]	Theo. IEC (meq g^{-1})	Exp. IEC (meq g^{-1})[b]	Conductivity in Water (mS/cm)[c]	Water uptake (%)	Hydration number (λ)	Height wet (mm)	σ in Electrolyte (mS/cm)[d]
sb	sb-PSU-L	1.45	1.26	52	35	15	0.070	27
	sb-PSU-M	1.62	1.42	74	56	19	0.057	nd[e]
	sb-PSU-H	1.77	1.59	88	70	23	0.060	34
as	as-PSU-L	1.45	1.31	58	39	12	0.063	24
	as-PSU-M	1.62	1.41	87	70	24	0.062	45
	as-PSU-H	1.77	1.57	83	62	22	0.060	nd[e]
ss	ss-PSU-L	1.45	1.25	44	32	11	0.056	20
	ss-PSU-M	1.62	1.49	62	42	14	0.065	16
	ss-PSU-H	1.77	1.53	73	50	15	0.056	26
	Nafion 212	0.91	0.90	105	28	24	0.051	34[f]

[a] L/M/H represent low/medium/high content of acid-functional DPDFS monomer in all DPDFS monomers in feed.
[b] Determined by titration.
[c] Measured in DI water at RT (22 °C).
[d] Measured in 1.7 M $VOSO_4$ / 3.3 M H_2SO_4 at RT (22 °C).
[e] Not detected.
[f] Data for Nafion 117.

Conductivity of all PEMs was measured in acid solution with different concentrations and then electrolyte solution containing 1.7 M $VOSO_4$ in 3.3 M H_2SO_4 as shown in Table 2-2. It was observed that the conductivity of membranes equilibrated in the electrolyte solution significantly dropped for all membranes including Nafion when compared to the conductivity in H_2O. This phenomenon has been reported for Nafion 117.[131] The decrease is the resultant of several factors, including uptake of transition metal ions and dehydration of the membrane. Because transition metal cations have much lower mobility than protons in fully hydrated Nafion, membranes containing such cations generally have much lower conductivity than unexchanged proton-form membranes. We have also measured conductivity in H_2SO_4 solutions before obtaining electrolyte conductivity via the following sequence: DI water, 1 M H_2SO_4, 2 M H_2SO_4, 3.3 M H_2SO_4, and finally 1.7 M $VOSO_4$ in 3.3 M H_2SO_4. To compare the membranes

with different side-chains, the results for the lowest IEC sb-, as-, and ss-PSU-L membranes are plotted in Figure 2-7. Up to 3.3M, all membranes show minimal changes in conductivity. It was seen that ss-PSU-L exhibited appreciably lower conductivity in water as well as in acid solutions when compared to the other membrane types. However, interestingly the difference of electrolyte conductivity of all three membranes measured in 1.7 M $VOSO_4$ / 3.3 M H_2SO_4 became almost negligible as indicated by the points with open marks.

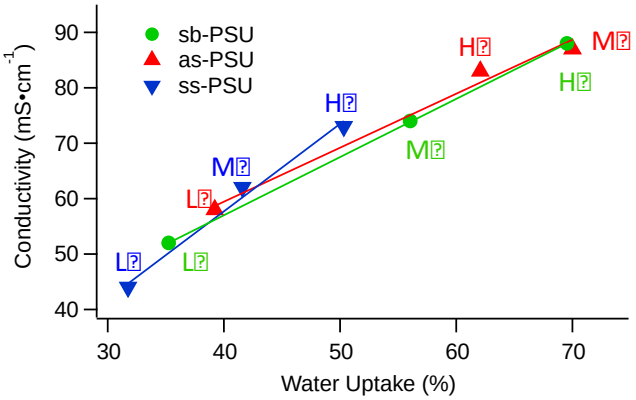

Figure 2-5 The correlation of conductivity and water uptake for all PEMs.

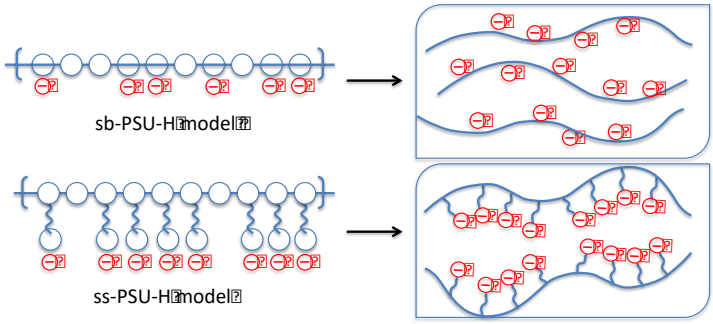

Figure 2-6 Schematic illustration of the proposed morphologies for sb- and ss-PSU membranes

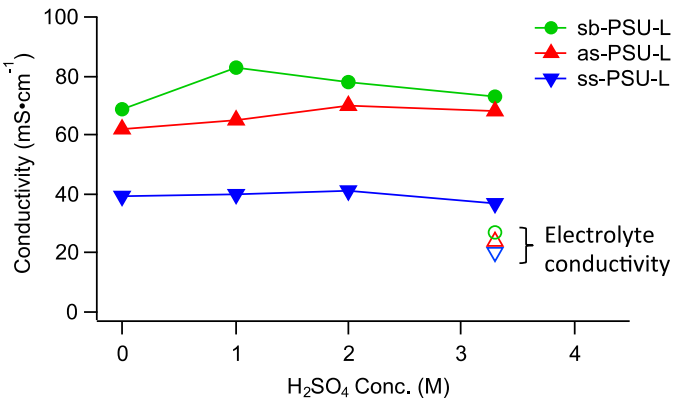

Figure 2-7 Comparison of conductivity in acid and electrolyte solutions between sb, as, and ss-PSU-L (IEC=1.45) membranes. Measurements were done using same strips (n=3 for each) in sequence from DI water to increasing acid concentration with >24 h time before each measurement. The conductivity of membranes measured in 1.7 M $VOSO_4$ / 3.3 M H_2SO_4 are shown with open marks.

2.3.4 Membrane evaluation in VRFB cell

The membranes were subjected to an OCV decay measurement with results shown in Figure 2-8. OCV decay correlates with the rate of exchange of vanadium species across the membranes. In previous studies of the effects of the equivalent weight (EW),[111,112,116] permeation through lower EW materials was slower than through high EW systems, presumably due to the higher degree of swelling of the latter when exposed to electrolytes. A similar trend was observed here: higher EW led to higher cross-over rates for each type of polymer. As indicated by the OCV decay, the as-PSU-L and as-PSU-M membranes exhibited high vanadium crossover rates and therefore the as-PSU-H membrane was not tested. According to Figure 2-8, the 'ss' series membranes showed the slowest overall vanadium crossover. For the three side chain types, the OCV of cells with as-PSU-M, sb-PSU-M and ss-PSU-M dropped to 1.2 V at 2338, 5386 and 9346 s respectively after the pump was stopped. The voltage shoulder near 1.3 V on the OCV decay curve is caused by depletion of V^{2+} and V^{5+} in the pores of the electrode and flow

field. To summarize this, for a given EW range, the vanadium permeability indicated in the OCV test increased in the order ss < sb < as.

In Table 2-2, the conductivity values in water for as-PSU-M, sb-PSU-M and ss-PSU-M are 0.087, 0.074 and 0.062 S/cm, respectively. Conductivity values in electrolyte have similar ordering and this in turn typically reflects the overall uptake of water or solution by the membrane. Given the similarity of the trends in water and electrolyte, we use the water conductivities here to analyze selectivity since we have complete data sets for these membranes. Because as-PSU has the lowest ratio of conductivity to rate of depletion of charged vanadium species (the inverse of the times given), the ionic transport selectivity of this membrane is the least suitable for use as an electrolyte separator in a VRFB. The ionic selectivity index proposed by Tang et al[112] indicates ss-PSU-M and sb-PSU-M are 2.9 and 2.0 times more selective than as-PSU-M. The side chain structures on PSU membranes can influence their ionic transport properties. Perhaps the flexible (though shorter) side chain on the as-PSUs can lead to altered mechanical properties of the material, leading to ion cluster channels of larger size in swollen as-PSUs. The overall higher conductivity and vanadium transport for 'as'-form membranes likely reflect increased swelling. This higher degree of swelling can facilitate diffusion, especially for vanadium ions with large coordination structures. The key point is that the most effective membranes balance conductivity and permeability, as reflected in the selectivity index. A more detailed investigation of these aspects of membrane properties and morphology is in progress.

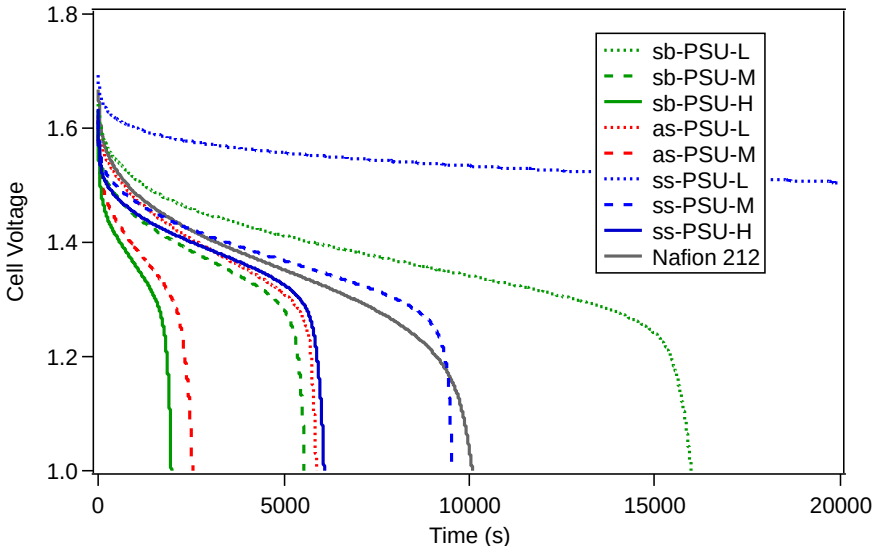

Figure 2-8 The OCV decay on battery cell with 100% SoC electrolyte after electrolyte circulation was stopped.

Cell cycling tests in VRFB cells were performed on the series of membranes with Nafion 212 as a control. Figure 2-9 shows efficiencies and areal specific resistance for 20 charge-discharge cycle tests for each membrane at a 200 mA/cm^2 current density. Overall, battery systems with PSU membranes showed excellent efficiencies with some membranes demonstrating superior performance over Nafion 212. For four PSU membranes, ss-PSU-H, ss-PSU-M, sb-PSU-H and sb-PSU-M, cells had energy efficiency of 86 to 87%, higher than the 85% observed with Nafion 212 under the same test conditions. Cells using sb-PSU-L and as- PSU-M exhibited energy efficiencies close to that for Nafion-based cells, while as-PSU-L showed the lowest EE, around 83%. The performance of PSU membranes in cycling test demonstrated that they are suitable for use as electrolyte separators in VRFB.

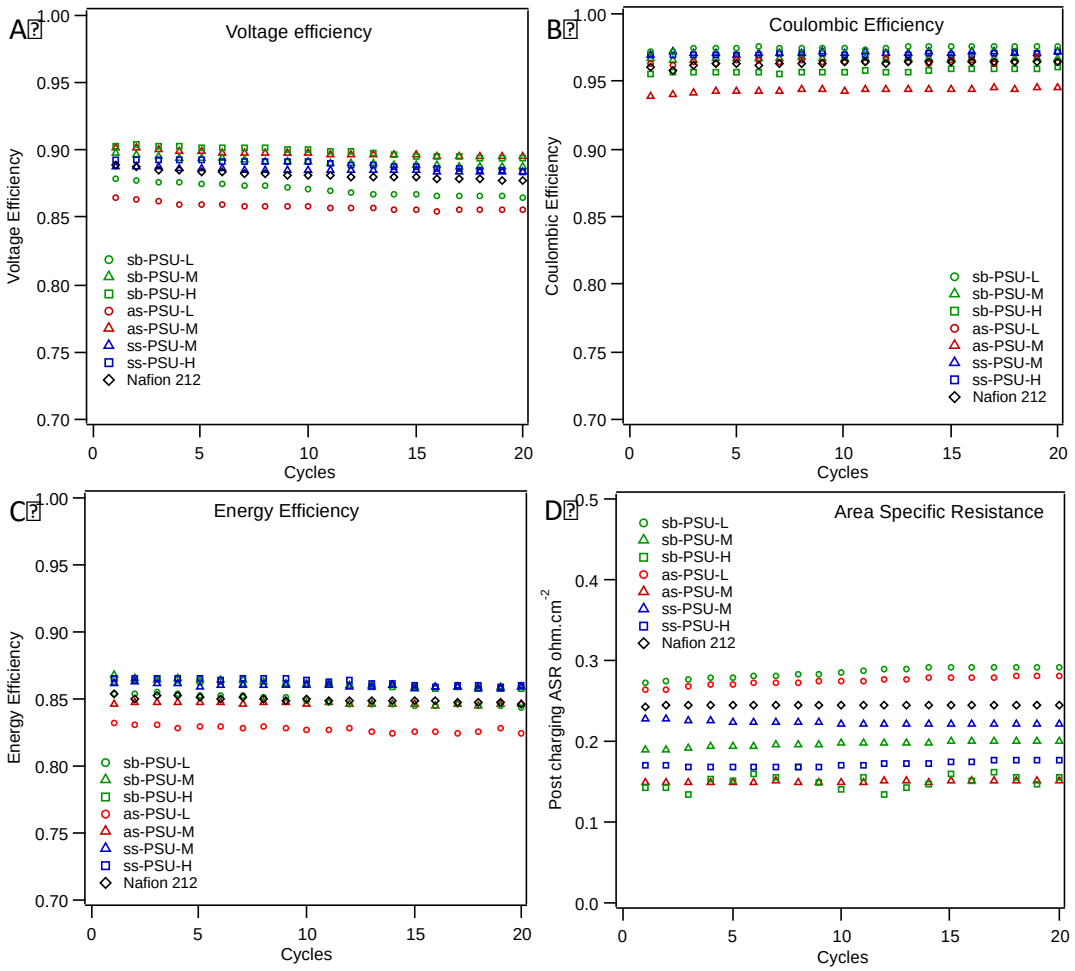

Figure 2-9 Efficiency data for the membranes, sb-PSU (green), as-PSU (red), and ss-PSU (blue), in a VRFB cell for 20 cycles: (A) Voltage Efficiency, (B) Coulombic Efficiency, (C) Energy Efficiency, and (D) Area Specific Resistance after each cycle.

PSU membranes can contribute to enhanced battery performance with their high conductance in the VRFB environment. Although all PSU membranes tested are slightly thicker than Nafion 212, areal specific resistances (ASR) of all cells with PSU membranes are lower than Nafion 212, except for cells using sb-PSU-L and as-PSU-L, as is shown in Figure 2-9 (D). All proton-form PSU membranes are less conductive than Nafion in DI water (Table 2-2), but have comparable or greater conductivities in the electrolyte solution. Details such as the uptake of ions and water by the membrane and the detailed mechanism of ionic transport in PSUs in equilibrium with strong electrolyte

solutions are under investigation and will be reported in the future. Cells equipped with PSU membrane of ASR lower than Nafion 212 showed higher voltage efficiency than Nafion 212 (Figure 2-9 (A)), because of lower ohmic loss by lowered internal resistance. The VE of each cell is dependent on its ASR in a roughly linear pattern, as presented below in Figure 2-10. The ohmic potential loss is proportional to the cell ASR.

The coulombic efficiency achieved by each PSU membrane is consistent with the OCV decay measurement. All cells with PSU membranes have higher coulombic efficiency than Nafion 212 in the cycling, except for those with sb-PSU-H and as-PSU-M. The higher CE obtained in cycling measurements directly reflect the slower rate of vanadium crossover across the membrane in battery cell. For each side chain type, the ionic conductivity of both proton and vanadium in the membrane increases with its IEC. Generally, membranes of higher IEC and lower thickness are used to reduce the internal resistance of the battery. Although a VRFB system with low ASR and high CE is always desired, vanadium crossover can also be increased by using a membrane with high conductivity. In Figure 2-10, the CE vs ASR of battery cell with PSU membranes is plotted to correlate the vanadium crossover with ASR. Apparently, as-PSU series and Nafion have lower ionic selectivity towards protons because they cause lower CE than the other membrane types at the same ASR level. The ss-PSU series have the highest ionic selectivity among all three types of membrane since it has the highest CE level. The high ionic selectivity in sb and ss-PSU suggests that their polymer structure is more favorable for proton transport than for vanadium ion transport. Since ss-PSU has a benzene- tethered side chain and sb-PSU has sulfonate directly attached on backbone,

narrower and more branched ionic channels may form in the sb-form. These can be expected to slow down ion and water transport.

PSU membranes with ss- and sb- types of side chain structure show superior ionic selectivity to reduce vanadium crossover and maintain high conductivity in the VRFB. Figure 2-11 shows the relative capacity of the cells over 20 cycles. The capacity decrease is much less with all hydrocarbon membranes than that with Nafion. This is a great sign of the higher ionic selectivity towards proton transfer. In particular, the membranes with the highest IEC such as ss-PSU-H and sb-PSU-H, which also gave the highest EE, showed the highest capacity retention of all membranes cycled. The incorporation of a side chain onto the polymer scaffold resulted in a change in efficiency. The longer and more hydrophobic ss- side chain gave a lower VE and ASR, but increased CE as a result of increased ion selectivity.

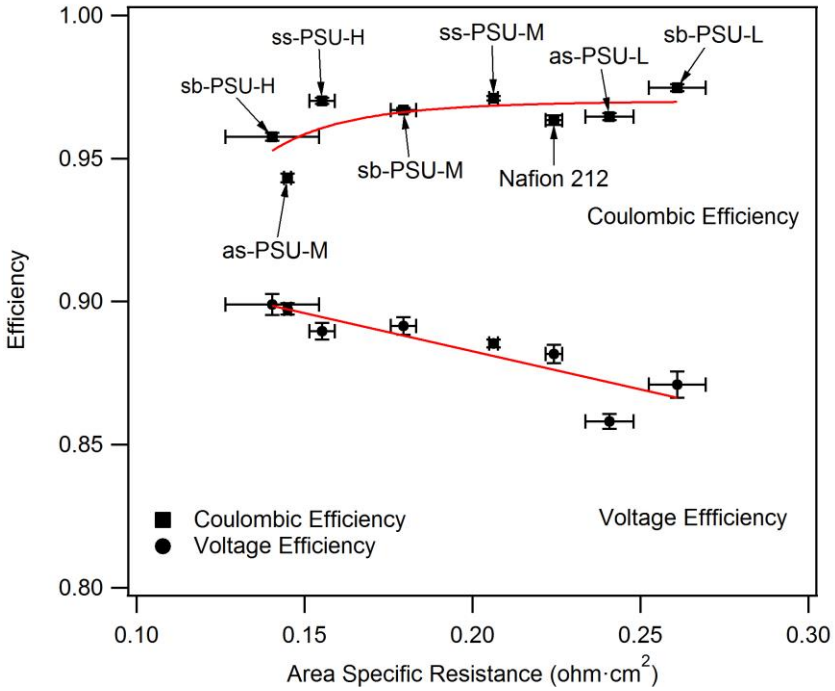

Figure 2-10 The comparison of coulombic and voltage efficiencies with respect to Area Specific Resistance of the battery with PSU membranes and Nafion 212.

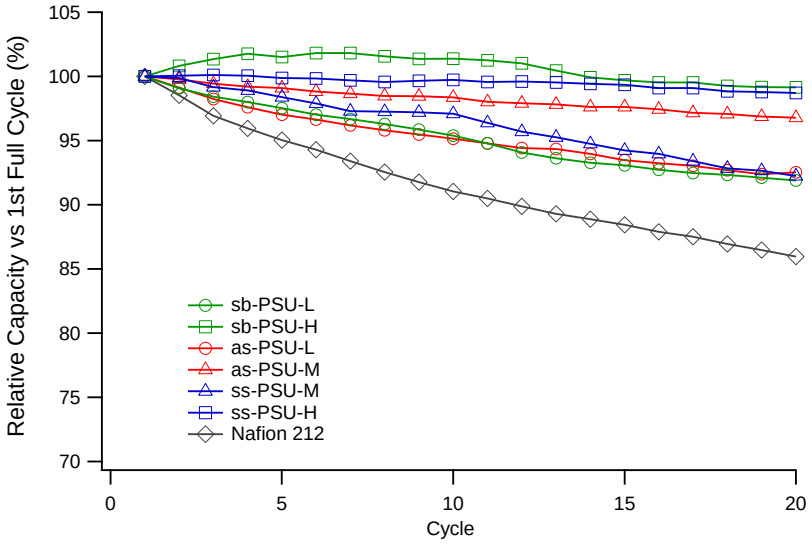

Figure 2-11 Capacity changes over 20 cycles in VRFB.

2.3.5 Thermal analysis

Thermal behavior of three types of membranes and stability of structure and properties after the cell cycling test were studied using TGA, DSC, ^{1}H NMR, and conductivity measurements. TGA profiles of sb-, as-, and ss-PSU-H membranes are shown in Figure 2-12. Thermal degradation of sb-PSU (green) shows 2-step process and that of as- (red) and ss-PSU (blue) indicates 3-step process. For these 'H' series with IEC 1.77, theoretical wt% of -SO_3H in the polymer is 14 wt% for all three membranes. The first weight loss % in all membranes is corresponding to the degradation of sulfonic acid group, which also agrees with previous reports.[23] The 5% weight loss temperature, T_d (5%) of sb-, as-, and ss-PSH-H are 338, 254, and 320 °C, respectively. Significantly lower thermal stability of the -SO_3H group in as-PSU is reasonable because it is an isolated group on the alkyl side chain unlike more stable conjugated acid form seen in sb- and ss-PSU. The as-PSU-H membrane displays distinct second degradation starting around 400 °C, that indicates degradation of propenyl side group (theoretical weight% of as-PSU side chain except -SO_3H: 7 wt%). The same second degradation is recognizable for ss-PSU, however it is slower process as seen in gentle slope. Finally, degradation of polymer backbone of all three membranes starts around 470 °C. Changes of the degradation profiles for all membranes before and after cell cycling test were negligible as shown in Figure 2-16 (supporting info), indicating no appreciable degradation of polymers occurred in the VRFB cell.

DSC curves of three PSU-H membranes for their third heating runs are shown in Figure 2-13. The Tg of all these polymers are expected to be between 200-300 °C, which is close to acid group degradation temperatures. Only one distinct Tg was observed at

245 °C in sb-PSU-H. Interestingly, exothermic transitions were observed at lower temperature for as- and ss-PSU-H membranes. Those thermal events were reversible for multiple runs after every rapid cooling from 270 to -40 °C. Since no such transition was observed for the backbone-sulfonated sb-PSU-H, the reversible exothermic events are probably caused by the orientation of side groups or ion complex formation with the side chain.

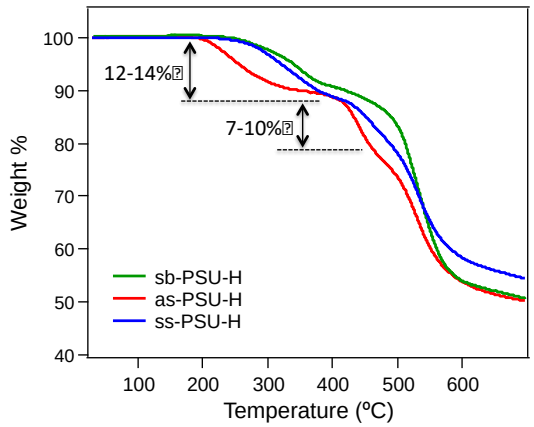

Figure 2-12 TGA profiles of H-series (IEC = 1.77) membranes: heating at 10 °C/min.

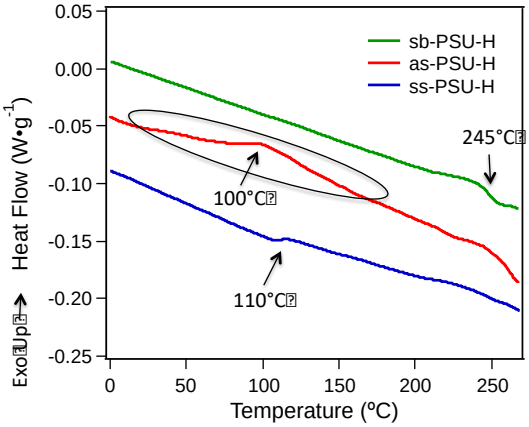

Figure 2-13 DSC profiles of H-series membranes: third heating run at 10 °C/min.

2.3.6 Chemical stability

Proton conductivity was re-evaluated for the membranes after cell cycling to observe any changes in performance. The original conductivity for sb-, as-, and ss-PSU-H were 88, 83, and 73 mS/cm, respectively. The conductivity values of the same membranes after the cell test were in the range of 60-99 mS/cm. This comparable conductivity ranges before and after cell cycling was indication that no major chemical or physical change took place, which agreed with the aforementioned thermal stability by TGA. It is, however, noted that all three types of membranes showed some degree of signs of wear after cycled in the VRFB cell, indicating that they were no longer as robust

as they were prior to cycling. The more brittle nature of the membranes after cycling indicates polymer chain cleavage. ASR shows that the resistance in the cell only increased slightly through 20 cycles, complementing the minimal change in conductivity.

Finally, the detailed chemical structure of the polymers was studied using ^{1}H NMR by re-dissolving the membranes in DMSO-*d6* after the cell cycle test. The NMR spectra of sb-PSU-M before and after the cell were identical (Figure 2-17). However, after the cell cycling the ss-PSU-M membrane was no longer completely soluble in the solvent. This is possibly due to a crosslinking reaction of the side groups under the VRFB cell conditions. As shown in Figure 2-14, the ^{1}H NMR spectra of as-PSU-M before and after the VRFB cell cycling test revealed a noticeable decrease in non-aromatic alkene proton peaks (d, e) at 6.6 and 6.7 ppm as well as the related peaks (a, b, c, f) of the functional monomer unit, against the main chain peaks (g, h, i, j) in the spectrum (b). The integration of those acid monomer peaks appeared to be nearly 20% lower after the cell cycling test. Alkenes are generally sensitive to aqueous acid by way of hydration reactions or they can be oxidized by oxidizing agents. Even given this minor structure change, the electrolytes potentially could have morphology changes. Both 'as' and 'ss' side chain membranes are more susceptible to reactions under the given conditions than the direct backbone sulfonated polymer membrane. As expected, sb-PSU-M remained chemically unchanged shown by ^{1}H NMR (see Figure 2-17). Overall, the three types of membranes in this study have shown satisfactory stability in their structures and performance based on the cycling studies. More detailed structural/morphological characterization and thermal/mechanical analysis are underway.

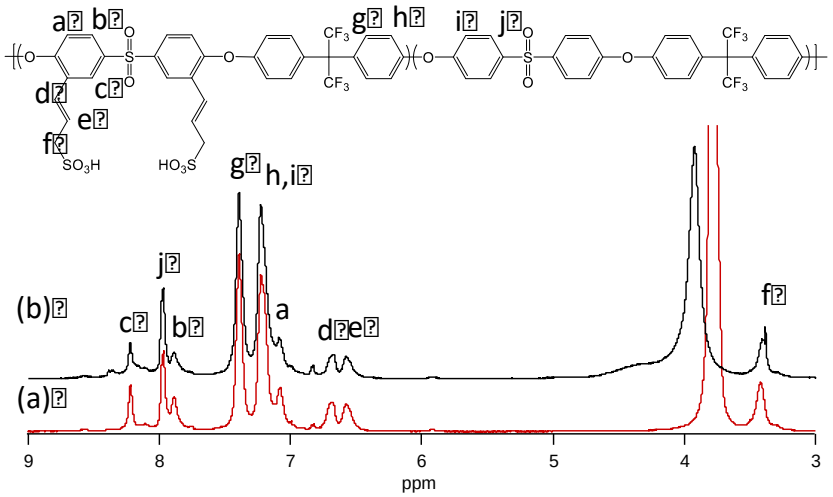

Figure 2-14 ^{1}H NMR spectra of as-PSU-M membranes before (a) and after (b) cell cycling test.

2.4 Conclusion

Proton exchange membranes were prepared from polysulfone random copolymers containing three different side chains with a controlled range of IECs. The physical properties of the membranes were affected by the addition of a side group between a polysulfone backbone and the characteristic sulfonic acid groups. The use of a styrenyl group resulted in relatively lower water uptake without compromising its *in situ* performance compared to PSU sulfonated along its backbone. Coulombic, voltage, and energy efficiencies were measured in a VRFB cell and showed similar energy efficiency for most membranes despite large difference in conductivity and water uptake. Most of the membranes, regardless of their side chain, displayed high EE (up to ca. 86%) which was higher than that of Nafion 212. Specifically, the membranes of PSU with a styrenyl sulfonic acid side group (ss-PSU) showed slightly higher proton conductivity than other membranes if comparing at same water uptake, and performed well in the VRFB cell with excellent VE and CE. This result would indicate the formation of the most favorable domain structure in the membrane by the longest and most hydrophobic acid side group.

It was demonstrated that the morphology and properties of polysulfone PEMs can be improved without sacrificing overall cell efficiency. The post-cell membranes showed no significant changes in structure and performances, however indicated a minor chemical transformation. Further characterization will be done on these membranes and ss-PSU series will be further explored due to its higher potential in VRFB membrane applications.

2.5 Supplemental Materials

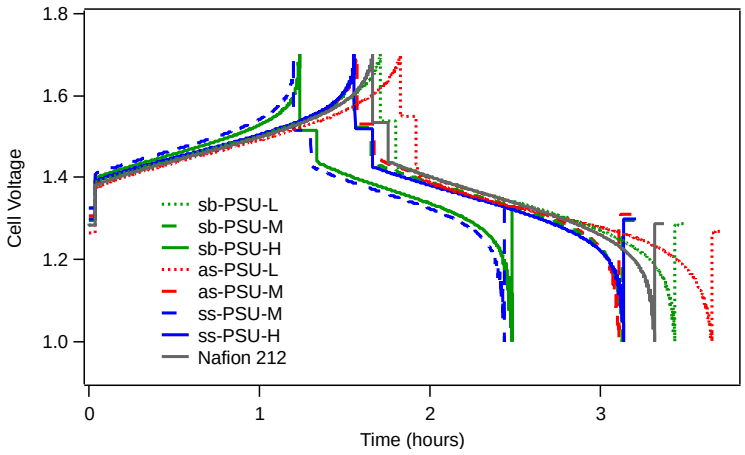

Figure 2-15 The 1st cycle of charge-discharge curves for a VRFB cell.

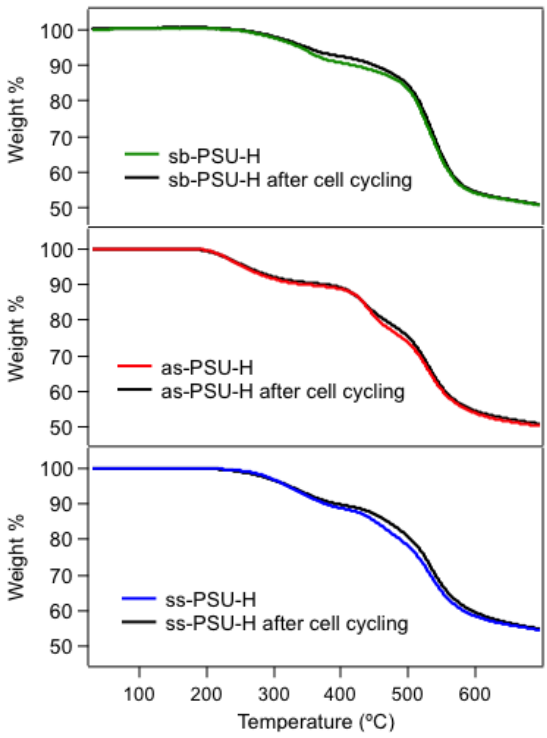

Figure 2-16 TGA profiles of H-series (IEC = 1.77) membranes, before and after VFRB cell cycling test: heating at 10 °C/min.

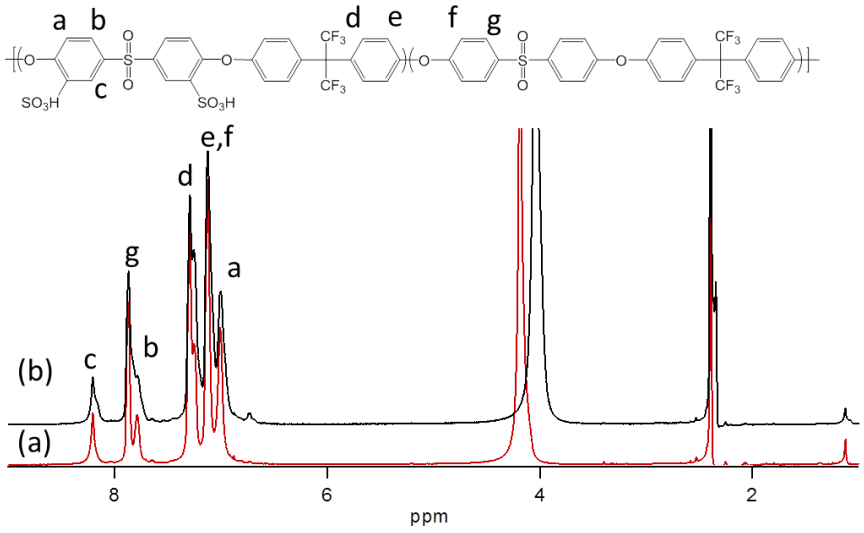

Figure 2-17 ^{1}H NMR spectra of sb-PSU-M membranes before (a) and after (b) cell cycling test in DMSO-d6.

Chapter 3

Nanoporous Polysulfone Membranes via Degradable Block Copolymer Precursor for Redox Flow Batteries

Porous membranes are advantageous as VRFB separators since they are the most cost-effective alternative to Nafion. A systematic study on structure-property relationships, specifically correlated to pore size and morphology, can lay the foundation necessary for porous membranes. This chapter outlines the initial study of our second approach towards the research goal to understand the structural effect of PEMs, focusing on the novel fabrication method of robust nanoporous membranes from precisely designed degradable block copolymers, and the preliminary results in VRFBs.

3.1 Introduction

Various types of energy storage technologies including electrochemical systems such as fuel cells and redox flow batteries (RFB) have been actively developed in the past few decades. RFBs are considered to be a leading option for medium to large scale energy storage because of their excellent combination of energy efficiency, capital cost and life cycle costs without specific site requirements.[3,113,132,133] One of the key materials in the RFB is the membrane separating the two half cells. This is typically an ion exchange membrane which serves the dual purpose of ion conduction and inhibition of 'cross-over' of active species between compartments. Perfluorosulfonic acid (PFSA) membranes such as Nafion® have been employed in redox battery systems as a separator. While these membranes show good stability in the RFB, they suffer from relatively high crossover as well as their high cost. Developing a suitable membrane to provide

the right balance between performance and cost is a focal point for RFB developers. Specifically for vanadium redox flow battery (VRFB) systems, an ideal membrane should offer the following characteristics: 1) high proton conductivity to reduce internal resistance, 2) low vanadium and water permeability to prevent crossover, 3) chemically inert and mechanically robust to withstand highly acidic RFB conditions, and 4) low cost to be market competitive.[9,112,115,116,134,135]

To achieve superior VRFB membranes, investigation of the effect of membrane morphology on the ionic conduction behaviour is a feasible approach. Recent studies have demonstrated the nanostructural control of heterogeneous polymers for ion exchange membranes. Block copolymers offer ordered or disordered bicontinuous morphologies which could effectively localize the ion channels. In addition to the amphiphilic nanostructured membranes of which many researchers have developed thus far, nanoporous membranes are particularly of interest if the pore structures and properties can be tailored. A promising avenue for production of nanoporous materials involves a bottom-up approach utilizing self-assembled block copolymer membranes containing a degradable block that can be selectively removed. The removal of this block can be done after the tailored nanoscale morphology has been achieved resulting in a continuous nanoporous morphology throughout the material. Since the late 1980's several groups have employed similar methods to achieve nanoporous materials in general purposes or other applications.[136-141] Hillmyer et al. and a few other groups have prepared various block copolymer systems including a polylactide (PLA) block

which is synthesized by controlled ring opening polymerization (ROP) and is readily hydrolyzed under mildly basic conditions.[84,85,101,105,108] Polystyrene-b-PLA is one of the most studied systems. After removal of the PLA blocks the morphologies of nanoporous polystyrene materials were well characterized. While a few studies using hydrocarbon porous membranes for VRFB have recently been reported,[46,49] the structures and chemistry of those pores have not been tailored. In this work, we report a new method to prepare well-structured nanoporous polysulfone (PSU) membranes via cross-linkable PSU-PLA block copolymers as a precursor, followed by degradation of the PLA block and pore surface functionalization. PSU is a widely-utilized polymer for membrane applications based on its chemical resistance, mechanical strength, and thermal stability. Hydroxyl-surface and acid-functionalized nanoporous PSU membranes are characterized and examined as a separator for VRFB systems. It is important to point out that the emphasis here is on the preparation and investigation of the new type of nanostructure, not on the final application of the membrane. The latter is described in preliminary fashion and many practical details will be explored in work to follow this contribution.

3.2 Experimental

3.2.1 Materials

Bisphenol A (BPA) and 4,4'-dichlorodiphenyl sulfone (DCDPS) were purchased from Oakwood Chemicals, and DL-Lactide was purchased from Purac Biochem (Netherlands). All these monomers were recrystallized twice from dry toluene. Dimethylacetamide (DMAc) and toluene purchased from Fisher and 1,8-

Diazabicyclo[5.4.0]undec-7-ene (DBU) purchased from Sigma-Aldrich were vacuum distilled over calcium hydride and stored under nitrogen. All other reagents were reagent grade and used as received.

3.2.2 Polymer synthesis

Propenyl-functionalized polysulfone (PPSU) macroinitiator. α, ω-Dihydroxy-PPSU macroinitiator was synthesized by polycondensation with precise stoichiometric control.[142] The typical procedure is as follows: BPA (9.702 g, 42.50 mmol), 2,2'-diallylbisphenol A (2.313 g, 7.50 mmol), DCDPS (14.05 g, 48.91 mmol), and K_2CO_3 (8.31 g, 60 mmol) were charged into a 3-neck flask equipped with a nitrogen inlet, Dean-Stark trap, reflux condenser, and magnetic stirrer. Under nitrogen purge, anhydrous DMAc (105 mL) and toluene (52 mL) were added to the reaction flask and the mixture was heated to 155 °C for 4 h. Following dehydration, the temperature was slowly increased to 180 °C with gradual removal of toluene from the trap. After complete removal of toluene, the reaction temperature was kept at 170 °C for 16 h. After confirming, by ^{1}H NMR, the completion of polycondensation to yield the diphenol capped polymer, the temperature was slightly decreased to 160 °C and 4-fluorobenzaldehdye (1.2 mL, 11 mmol) was added to the reaction mixture and stirred for another 12 h. After complete conversion of the diphenol end groups to dialdehyde, the reaction mixture was cooled to room temperature. To reduce the aldehyde terminals to primary alcohols, $NaBH_4$ (1.26 g, 33.3 mmol) was added to the crude mixture and diluted with 30 mL of DMAc and allowed to stir for 12 h. The final product was obtained by first centrifugation to remove solid byproducts, and reprecipitation into 1:16 acetic acid/isopropanol (850 mL) solution. The off-white fibrous precipitate was recovered by

vacuum filtration and washed in boiled water for 1 h. The solid product was recovered from the aqueous solution by vacuum filtration, dried and precipitated twice from chloroform to diethyl ether. The fibrous product was dried in vacuo at 100°C for 48 h before moving on to the next step.

PLA-PPSU-PLA triblock copolymers. The triblock copolymers of PLA and PPSU were prepared by ROP of D,L-lactide onto dihydroxyl end-capped PPSU using an organocatalyst.[143] The typical polymerization procedure for PLA-PPSU-PLA with targeted 50:50 weight ratio is as follows: in a nitrogen filled glovebox, PPSU (4.0 g, 2.0 mmol) and D,L-lactide (4.6 g, 32 mmol) were charged into a single neck reaction flask equipped with a magnetic stirrer. Anhydrous dichloromethane (58 mL) was added to the reaction flask and following complete dissolution DBU (48 µL, 0.32 mmol) was added to the reaction mixture. The flask was stoppered and allowed to stir at room temperature for 4 h. After determining near 100% monomer conversation by ^{1}H NMR, benzoic acid (60 mg, 0.56 mmol) was added to the reaction mixture. The solution was subsequently added dropwise to vigorously stirring diethyl ether (500 mL) to precipitate the product. A second precipitation from chloroform to diethyl ether was done to further purify the final polymer. The product was recovered by vacuum filtration, washed with isopropanol and dried in vacuo at 60°C for 24 h.

3.2.3 Nanoporous PPSU membranes

The polymer membranes were prepared by solution casting. The PLA-PPSU-PLA triblock copolymer was dissolved in DMAc to give a 7-10% w/v solution. To the polymer solution, tert-butyl hydroperoxide (5.5 M solution in decane) was added which resulted in a 0.022 M solution to catalyze crosslinking of the propenyl pendant groups by

radical reaction. The mixed solution was first cast onto a flat glass plate in an oven at 40 °C for 24 h. Subsequently, the oven temperature was increased to 150 °C, and the membrane was annealed for 8 h under nitrogen atmosphere and mild vacuum. The oven temperature was further increased to 180 °C for 8 h to activate the radical-mediated crosslinking reaction. After cooling the glass plate was immersed into H_2O at room temperature to recover the crosslinked block copolymer membranes. Hydrolysis of the degradable PLA block domains and formation of the nanoporous channels was accomplished by immersing the membranes in 4 M NaOH solution and heating for 7 days.[84] After complete PLA hydrolysis, confirmed by FT-IR, the membranes were refluxed in H_2O for 1-2 h three times with fresh H_2O. Finally, the membranes were allowed to soak in H_2O overnight and dried in vacuo before any further functionalization.

Membrane ID is described in this paper based on (1) the block weight% of PPSU in PLA-PPSU-PLA determined by ^1H NMR and (2) mol% of crosslinkable dipropenyl-BPA out of total BPA monomers. For example, the membrane prepared from the copolymer, PPSU/PLA (62/38 wt%) and dipropenyl-BPA/BPA (15/85 mol%) was labeled as "PPSU62-X15".

3.2.4 Pore sulfonation of nanoporous PPSU membrane

Synthesis of Sodium 4-(2-azidoethyl)benzenesulfonate. Sodium 4-(2-bromoethyl)benzenesulfonate (4.0 g, 14mmol) was dissolved in H_2O (20 mL) then diluted with ethanol (20 mL) and transferred to a single neck reaction flask equipped with a magnetic stirrer and condenser. NaN_3 (5.0 g, 77mmol) was dissolved separately in 20 mL of H_2O (20 mL) and ethanol (20 mL) and added to the reaction vessel. The reaction mixture was heated to reflux for 12 h, and cooled

to room temperature after confirming complete conversion of halide groups to azido groups by ^{1}H NMR. The solution was filtered and product was recovered *in vacuo* and recrystallized once from H_2O/isopropyl alcohol. Sodium 4-(2-azidoethyl)benzenesulfonate (2.83 g, 82%). ^{1}H NMR: (499.7 MHz, D_2O) δ 7.60 (d, J = 8.5 Hz, 2H), 7.30 (d, J = 8.3, 2H), 7.34 (3, d, J = 16.7 Hz, 2H), 3.47 (t, J = 6.9 Hz, 2H), 2.83 (t, J = 7.1 Hz, 2H).

Conversion of hydroxyl to alkyne groups. The hydroxyl group lining the nanoporous channel was further functionalized by solid-phase reaction to obtain an alkyne group lining. The typical procedure is as follows: the nanoporous PPSU membrane (300 mg) was placed in a large neck flask capped with a septum and flushed with nitrogen. Anhydrous diethyl ether (130 mL) and DBU (1.6 mL, 10.7 mmol) were added to the reaction vessel and the heterogeneous reaction mixture was cooled to 0 °C. After 2 h, propargyl bromide (1.8 mL, 16.2 mmol) was added and the reaction was kept at 0 °C for 24 h. The membrane was removed from the solution and rinsed thoroughly with H_2O and sonicated in ethanol and H_2O several times.

Conversion of alkyne to sulfonic acid groups. The nanoporous channels of the alkyne functionalized membranes were clicked with sodium 4-(2-azidoethyl)benzenesulfonate to introduce sulfonic acid groups on the pore surface. In a large mouth flask capped with a septum, sodium 4-(2-azidoethyl)benzenesulfonate (1.0 g, 4.0 mmol), and sodium ascorbate (0.3 g, 1.7 mmol) were dissolved in 40 mL of 1:1 (vol) H_2O/t-butanol. Alkyne functionalized nanoporous PPSU membrane (300 mg) was immersed in the solution and purged with nitrogen. Separately copper sulfate pentahydrate (0.1 mg, 0.4 mmol) was

dissolved in 20 mL of 1:1 (vol) H_2O/t-butanol and added to the reaction flask. The reaction mixture was sonicated with heat for 24 h. The sulfonated nanoporous membrane was removed from the solution and washed with H_2O refluxed for 4 h, replacing the solution 2-3 times. The membrane was acidified by soaked in 1M H_2SO_4 overnight.

3.2.5 Instrumentation

Nuclear magnetic resonance spectroscopy (^{1}H NMR and ^{13}C NMR) was used to characterize all polymers on a Varian 500 MHz spectrometer in $CDCl_3$ using tetramethylsilane (TMS) as a reference. Gel permeation chromatography (GPC) was performed on a Shimadzu LC-20AD with two Jordi DVB 5 µm particle size columns (250 × 10 mm) calibrated against polystyrene standards with a flow rate of 1.0 mL/min using a THF eluent at 35 °C. Differential scanning calorimetry (DSC) was performed on a TA instruments Q20. Samples were scanned with a ramp rate of 10 °C/min over the temperature range 40 °C to 210 °C for 3 cycles. Fourier transform infrared spectroscopy (FT-IR) was done on a Nicolet 310 using thin film (neat) samples scanning from 4000 cm^{-1} to 400 cm^{-1}. Atomic force microscopy (AFM) was run using an AFM Workshop TT-AFM in tapping mode on a 15 x 15 x 7 µm scanner. Samples were drop cast onto fresh mica surface and treated under the same conditions used as membrane fabrication (5 µL of a 0.01% solution). Transmission Electron Microscopy (TEM) was used to observe nanostructures of block copolymer membranes. Samples were either microtomed from the membrane or drop-cast of the polymer solution onto the carbon-coated

copper grids and allowed to undergo same thermal treatment during membrane preparation and were subsequently analyzed on Jeol JEM-1200 TEM.

3.2.6 Membrane analysis

Conductivity measurement. Proton conductivity was calculated using a Biologic sp-150 potentiostat to measure the resistance on a strip of membrane in a 4 pt. closed wall cell. Conductivity was determined through the following equation:

$$\sigma = \frac{L}{R \times A}$$

where σ is the conductivity, L is the length between electrodes, R is resistance, and A is the cross-sectional area. Membranes of either porous PSU or acid functionalized porous PSU were cut into about 5 x 0.5 cm^2 strips and placed in soaking solution for at least 24 h prior to measurements. The strips were removed from the soaking solution, patted dry, and immediately placed into the cell for analysis.

Water uptake. Water uptake of the membranes was calculated by the weight loss from wet and dry samples as shown below in the equation:

$$Water\ uptake\ (\%) = \frac{W_{wet} - W_{dry}}{W_{dry}} \times 100$$

where W_{wet} is the wet weight and W_{dry} is the dry weight. All samples were soaked in DI water for a minimum of 24 h then removed and excess water was patted off and quickly weighed to get W_{wet}. Samples were then dried in vacuum at 50 °C for 24 h followed by heating at 100 °C for 1 h and quickly weighed to get W_{dry}.

Ion exchange capacity (IEC). IEC was calculated by titration of the membranes in the acid form. Membranes were allowed to equilibrate in 3 M NaCl for 24 h to promote cation exchange, followed by titrating against NaOH.

Acid titration. Titration was done by allowing the membrane strips to soak in a 3 M NaCl solution for 48 h and titrated against 0.01 M NaOH solution using phenolphthalein as an indicator.

3.2.7 Membrane RFB cell studies

The cell performance with nanoporous membranes was carried out with comparison to as received Nafion 212. The testing cell hardware used is a 5 cm^2 flow battery cell manufactured by Fuel Cell Technologies Inc. The test cell was equipped with one layer of the membrane of interest and, on each side, one layer of SGL enhanced-surface area carbon paper electrode (400 μm) housed in a 250 μm thick Teflon coated glass fiber gasket. The battery was operated through a Bio-Logic SP150 potentiostat with a 20 A booster. Electrolyte solutions (50 mL) contained 1.7 M $VOSO_4$ and 3.3 M H_2SO_4 were placed on each side of the battery. They were pumped between the cell and reservoirs by a Masterflex L/S peristaltic pump. Two-step charging was adapted to charge the battery up to fully charged state with all vanadium ion converted to V^{5+} on positive side and V^{2+} on negative side. During the cell operation, nitrogen of ultra-high purity was purged into negative electrolyte solution to prevent V^{2+} oxidation by air. The cell was cycled at current density of 200 mA/cm^2 with 1.75 V charging cutoff voltage and 1.0 V cutoff voltage. After each charging or discharging step, cell internal resistance was measured by AC impedance spectroscopy.[144]

3.3 Results and Discussions

Figure 3-1 summarizes the overall procedure to prepare functional nanoporous PSU membranes through 4 steps. In Step-1, propenyl-substituted PSU (PPSU) with dihydroxyl terminal groups was synthesized in a one-pot sequence. Polycondensation

between DCDPS and a mixture of BPA / diallyl-BPA (85:15 mol%) was performed under stoichiometric control to obtain α, ω-diphenol PPSU with the molecular weight range of 21-24 kDa calculated from the terminal aromatic peaks in ^{1}H NMR spectra (Figure 3-2a).

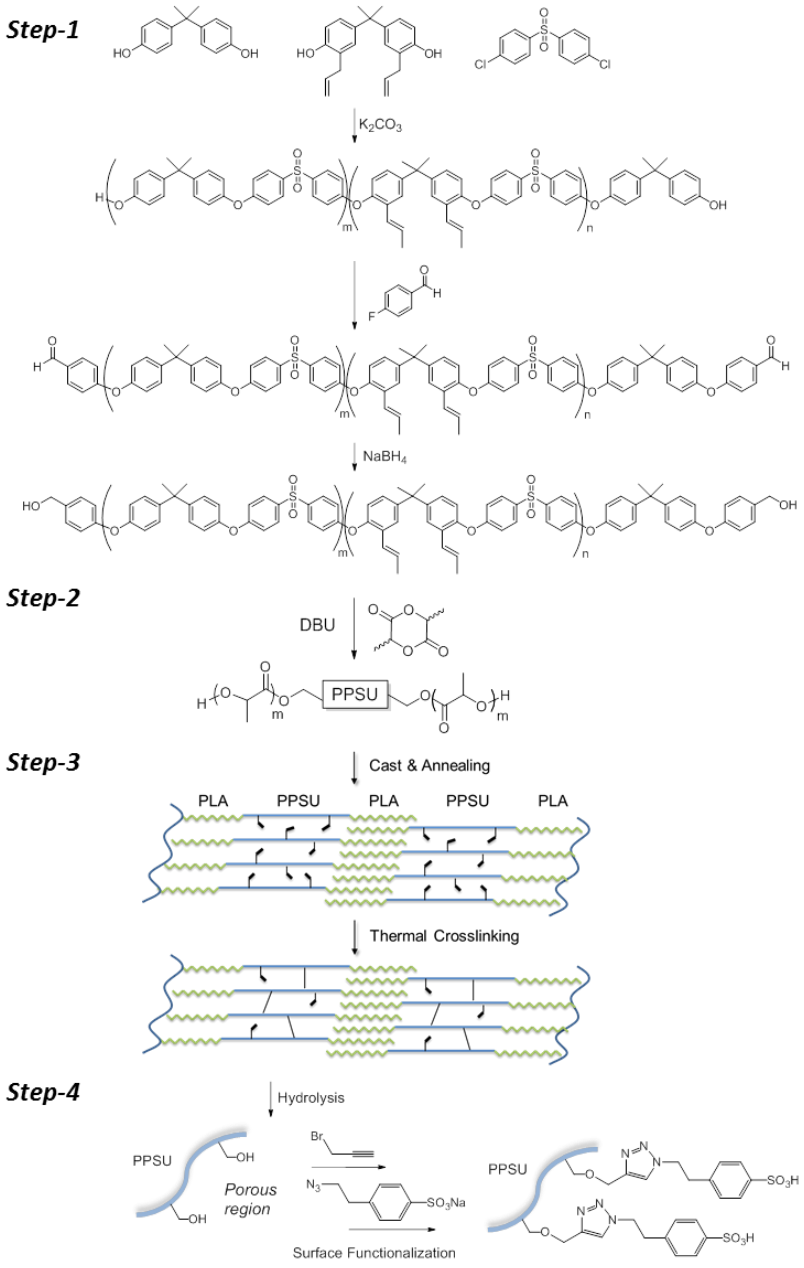

Figure 3-1 Preparation method of functional nano-porous PPSU membranes; Step-1: dihydroxyl-PPSU synthesis, Step-2: PLA-PPSU-PLA triblock copolymer, Step-3: membrane cast, annealing, followed by crosslinking of PPSU phase, Step-4: complete hydrolysis of PLA blocks followed by solid-phase reactions to achieve acid-functionalized pore surface

The allyl substituent of diallyl-BPA rearranged to a propenyl group during the polymerization. Upon completion of polycondensation, the phenol endgroups were

modified into primary alcohols via aldehyde groups. This process is crucial for our design since we utilize the alcohol groups after the membrane fabrication. The completion of each reaction was confirmed by monitoring ^{1}H NMR (Figure 3-2).

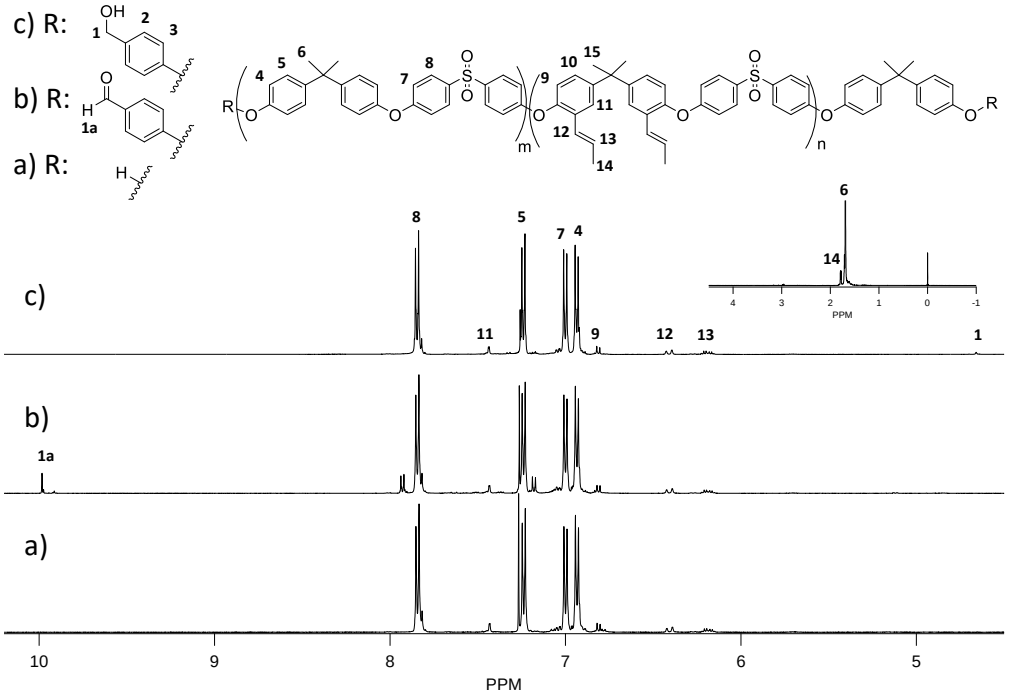

Figure 3-2 ^{1}H NMR spectra of (a) PPSU-X15 random copolymer, (b) PPSU-X15 with aldehyde end groups, and (c) PPSU-X15 with primary alcohol end groups in $CDCl_3$.

Step-2 is ring-opening polymerization of DL-lactide to prepare ABA type triblock copolymers (PLA-PPSU-PLA) with weight fractions of PPSU:PLA between 70:30 and 50:50 wt%. Typical ^{1}H NMR spectrum shown in Figure 3-3, and ^{13}C NMR spectra of PPSU and PLA-PPSU-PLA shown in Figure 3-4 have indicated those polymers are well structured and pure. The gel permeation chromatograms (GPC) of typical PPSU (PS-converted M_n = 15K, M_w = 41K) showed a relatively wide polydispersity index (2.80) which is not unusual for polycondensation polymers. However, the polydispersity became narrower (1.55)

after the polymerization of lactide to complete PLA-PPSU-PLA (PS-converted M_n = 44K, M_w = 68K) Figure 3-5.

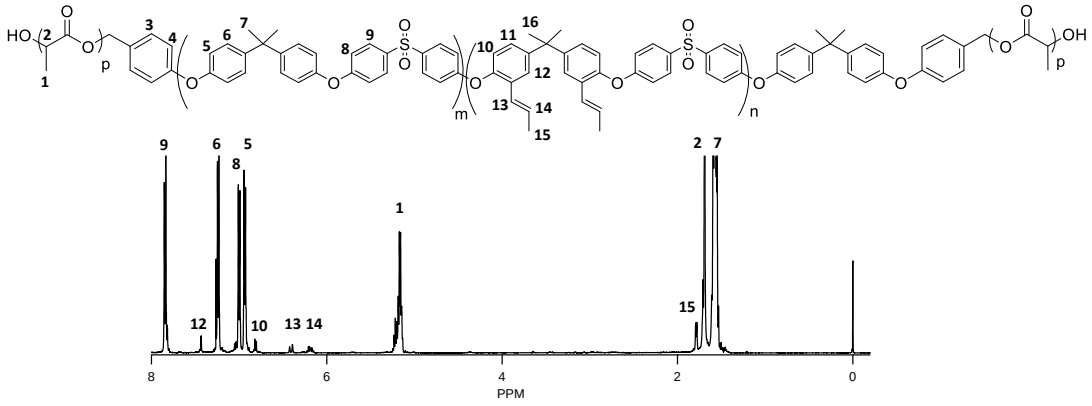

Figure 3-3 ^{1}H NMR spectrum of PLA-(PPSU55-X15)-PLA triblock copolymer in $CDCl_3$.

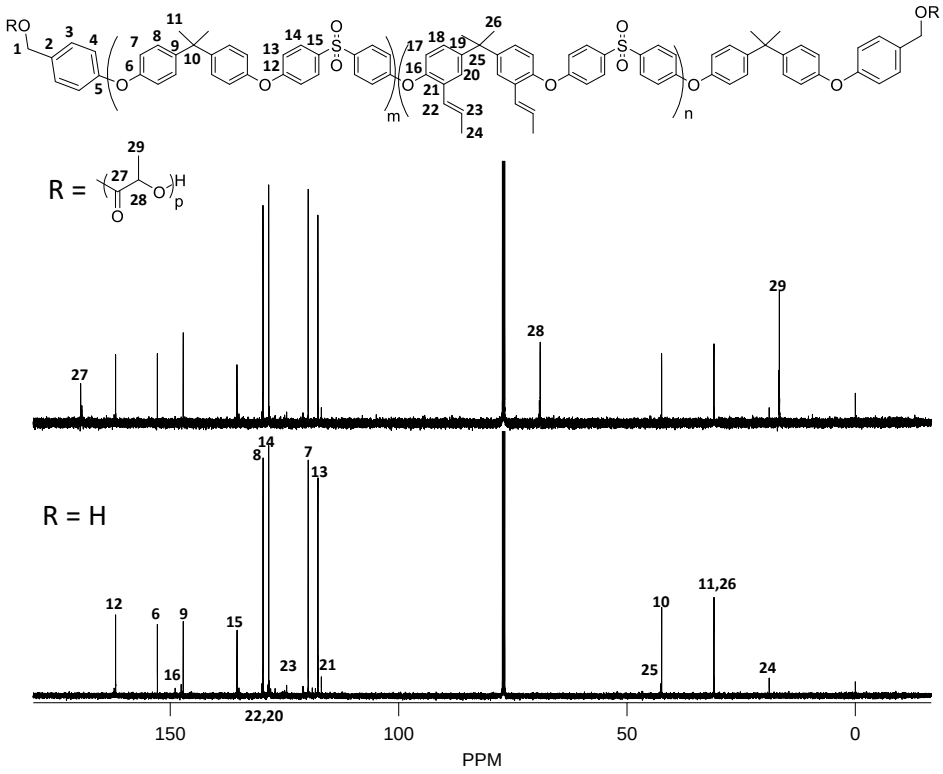

Figure 3-4 ^{13}C NMR spectra of (a) PPSU-X15 and (b) PLA-(PPSU55-X15)-PLA triblock copolymer in $CDCl_3$.

Step-3 in Figure 3-1 depicts the membrane fabrication process which involves three stages. First, the PLA-PPSU-PLA polymer solution in DMAc including a radical initiator was solvent cast at 50 °C. After 6 h the membrane was annealed at 150 °C to promote phase separation. Lastly, thermal crosslinking was done at the elevated temperature of 185 °C to promote radical initiation. The radical initiator, tert-butyl hydroperoxide was chosen based on its half-life temperature (10 h half-life at 170°C in benzene).[69] It is important that the radical formation rate must be reasonably slow at the annealing temperature of 150°C to allow the self-assembly of block copolymers into the ordered, phase-separated morphology before crosslinking of olefin side groups occurs. Figure 3-6 shows AFM images of PLA-(PPSU55-X15)-PLA cast from DMAc solution onto a mica surface and subsequently processed under the same conditions as membrane preparation. The topological image (6a) displayed a flat membrane surface with RMS roughness of 0.79 nm as seen in the depth profile. In contrast, the phase image (6b) from the same scan revealed a distinctly phase-separated structure with an average domain size of 20-30 nm and the repeat unit was about 50 nm.

The effect of crosslinking was clearly seen after the complete hydrolysis of the PLA blocks. Without the crosslinking process, the majority of the hydrolysed PPSU membranes were unable to maintain their integrity. Quantitative analysis on the degree of crosslinking and a study on the relationship to the mechanical properties are underway. TEM was also used to examine the nanostructures and crosslinking effect on the membrane structures. The microtomed cross section of the annealed membrane from non-crosslinkable triblock copolymer, PLA-(PSU57-

X0)-PLA showed a lamellae-cylinder morphology (Figure 3-7a). After hydrolysis of the same membrane without the crosslinking process at 185°C, some deformation of the ordered nanostructure was observed (Figure 3-7b). While the cast sample of crosslinked polymer PLA-(PPSU55-X15)-PLA displayed a distinct nanostructure (Figure 3-7c). FT-IR spectra confirmed the complete hydrolysis of PLA blocks based on the disappearance of the ester carbonyl absorbance peak (Figure 3-8). Thermal behavior of PPSU, PLA-PPSU-PLA, and hydrolyzed nanoporous PPSU membrane by DSC was shown in Figure 3-9. In the third heating cycle, the glass transition temperature (T_g) of PPSU macroinitiator was detected at 179 °C. The triblock copolymer displayed clearly the Tg for the PLA block (54 °C) and as a small transition for the PPSU middle block (176 °C), in which only slight shifts from the homopolymer Tg's were observed. This data suggested the well phase-separated structure during the heating-cooling process. After hydrolysis, DSC curve indicated the complete removal of the PLA blocks. Degradation of the PLA blocks results in re-appearance of the primary alcohols at the PPSU terminals. Therefore, this functional group should exist on the surface of the continuous nanoporous domain in the membranes.

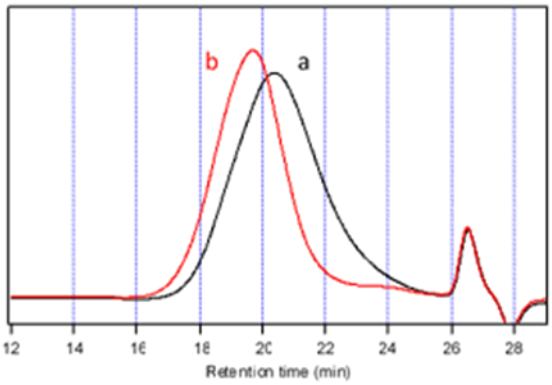

Figure 3-5 GPC chromatograms of (a) PPSU (MW: 23.5K by NMR) and (b) PLA-PPSU-PLA

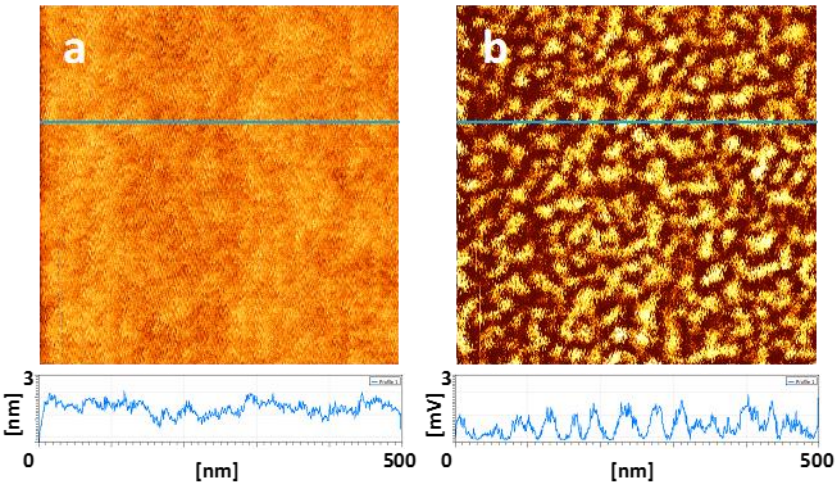

Figure 3-6 AFM result of the annealed PLA-PPSU-PLA solvent-cast membrane from PPSU/PLA = 55:45 weight%; a topological image (a) and a phase image (b) with cross section profiles of the line position.

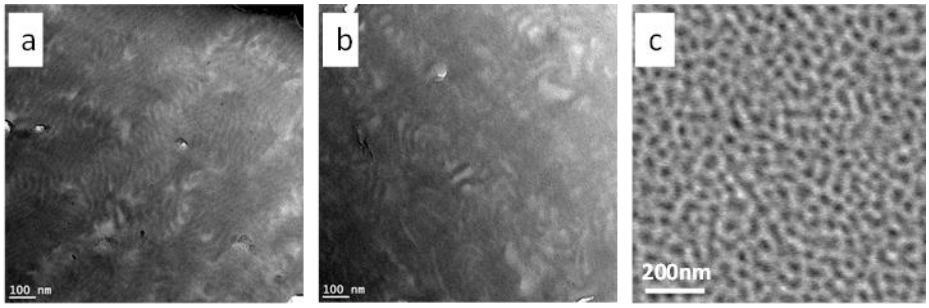

Figure 3-7 TEM micrographs of (a) PLA-(PSU57-X0)-PLA cross section of cast membrane, (b) PSU57-X0 cross section after PLA hydrolysis (not crosslinked), and (c) PLA-(PPSU55-X15)-PLA cast directly onto TEM grid and annealed.

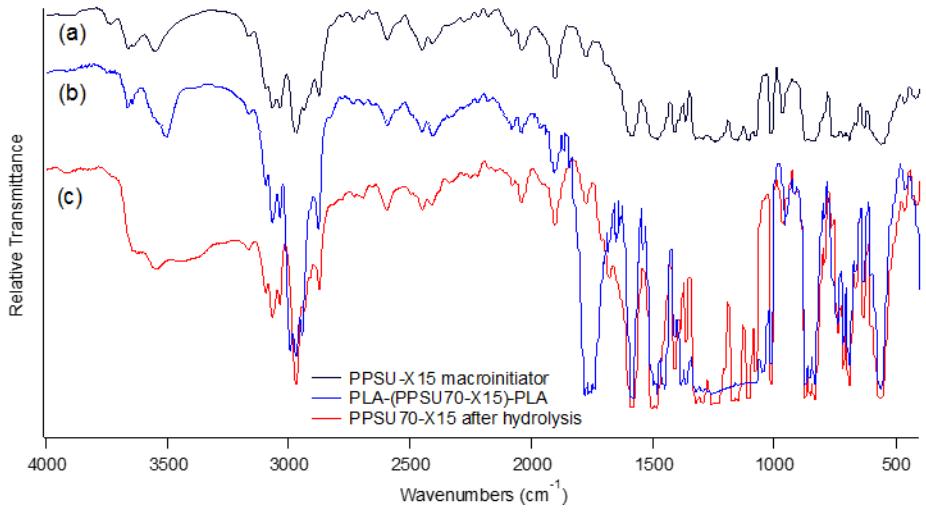

Figure 3-8 FT-IR spectra in pre- and post- hydrolysis: (a) PPSU macroinitiator, (b) PLA-(PPSU70-X15)-PLA triblock copolymer membrane, and (c) PPSU70-X15 nanoporous membrane.

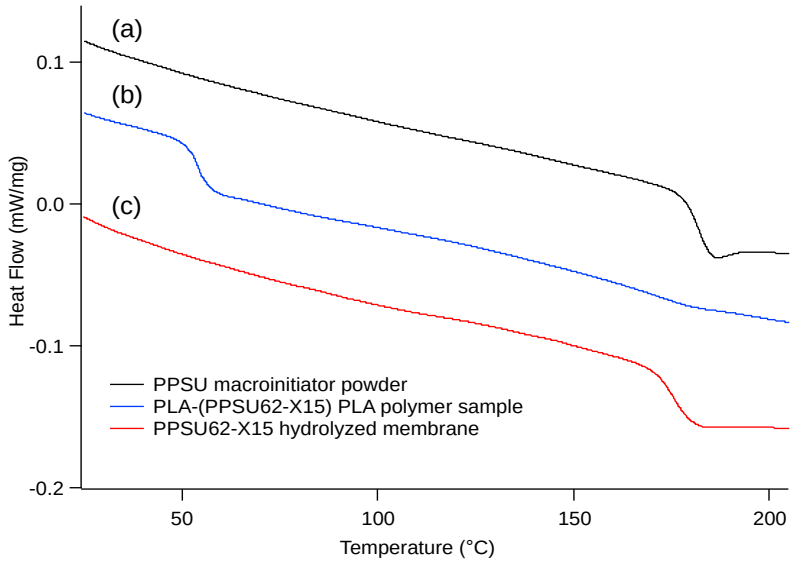

Figure 3-9 DSC thermograms of (a) PPSU-X15 macroinitiator, (b) PLA-(PPSU62-X15)-PLA triblock copolymer, and (c) nanoporous membrane (PPSU62-X15); Samples were scanned with a ramp rate of 10 °C/min over the temperature range 40 °C to 210 °C for 3 cycles (3rd heating cycle shown)

In Step-4, the nanoporous surface was functionalized by solid-phase reactions. The primary alcohols were first reacted with propargyl bromide to convert to the terminal alkyne groups. Using click chemistry, the pore surface was functionalized with a benzene sulfonic acid group. Nanoporous and acid-functionalized PPSU membrane structures were analyzed by FT-IR (Figure 3-10). After the first reaction, the IR spectrum showed the appearance of a C-H stretching absorbance corresponding to terminal alkyne at 3300 cm^{-1} which decreased following the click reaction. This absorbance change was subtle yet reproducible for all membranes examined. Titration of acid in the PPSU62-X15 membrane confirmed an IEC of 0.02 meq/g or about 25% conversion of original hydroxyl groups to sulfonic acid groups.

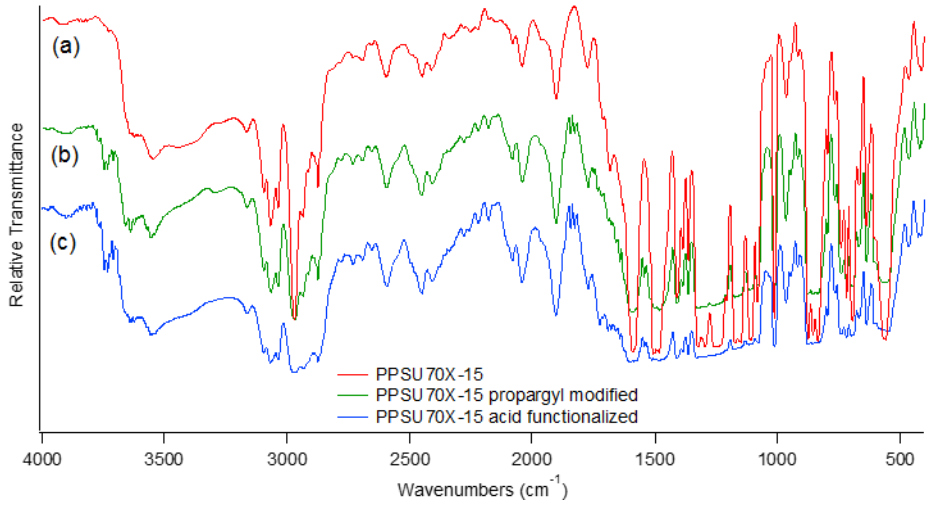

Figure 3-10 FT-IR spectra of PPSU70-X15 nanoporous membrane; (a) unmodified, (b) propargyl-modified pore surface, and (c) after adding sulfonic acid group by click chemistry.

The functionality of the membrane was explored in some preliminary tests of conductivity and battery performance. The conductivity of nanoporous and acid-modified membranes was measured after soaking in various concentrations of sulfuric acid. As plotted in Figure 3-11, the porous membranes with the original weight fraction of PPSU:PLA = 51/49% and PPSU:PLA = 54/46% show significantly higher conductivity data than that of Nafion® 212 in acid with a concentration of 2 mol/L or higher. A similar trend was observed for PPSU weight fractions of 62%. These data are typical of membranes in contact with the H_2SO_4 solutions.[131] The peak shape reflects the competing effects of acid uptake into the membrane (adding charge carriers increases conductivity) and

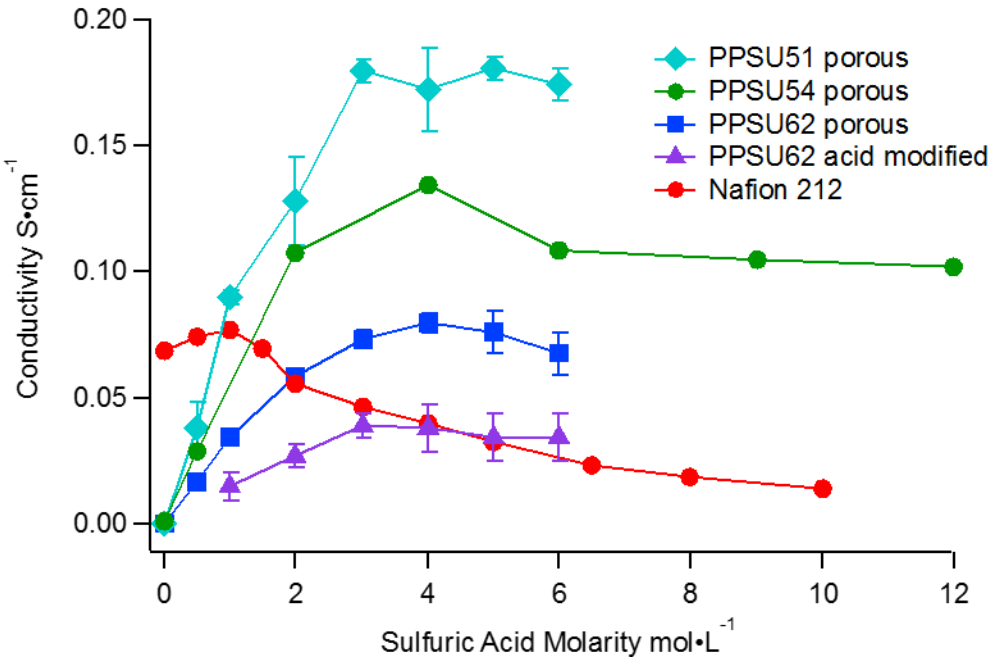

Figure 3-11 Proton conductivity of the membranes after soaking in sulfuric acidic solution for 24 h: porous PPSU51 (blue diamond), PPSU54 (green circle) PPSU62 (blue square), and surface functionalized PPSU62-acid (purple triangle), comparison with Nafion® 212 (ref)

decreasing water in the membrane (decreasing water content lowers mobility). This peaked behaviour is a general trend for the conductivity of acids as well.[145] For the porous system, we anticipate that all conductivity arises from the sulphuric acid solution simply imbibed into the pores and not significantly interacting with the polymer. The conductivity data indicated the volume of nanoporous region was precisely tailored by the block ratio of the triblock copolymers.

After chemically acidifying the pore surface, there was a noticeable decrease observed in conductivity (purple triangle data in Figure 3-11). This decrease in conductivity was in agreement with the lowering of water uptake after click reaction for PPSU62 membrane (31.5% and 20.6% for before and after acid-modification, respectively). Although the conversion rate of hydroxyl groups into sulfonic acid groups

was found to be very low, we initially expected similar or higher water uptake and increase of proton conductivity for the acid membrane. The lower conductivity of the acid-modified PPSU62 in comparison with the porous, unmodified system most likely reflects lower acid solution uptake in the system with acid modification, a result of the Donnan effect of lowering the uptake of 'co-ions' into the membrane. In the unmodified membrane the pore fluid is imbibed solution, while in the acid-modified system a lower concentration of acid is typically present.[131] This is a remarkable result: a mere 0.02 meq/g of ion exchange capacity, localized in a well-defined and rather wide pore, exhibits clear effects of exclusion of ions (For reference, the IEC of Nafion is ~45 times higher). Further systematic study of pore surface-modified membranes will be needed to discuss the effect of pore properties.

The behaviour shown in Figure 3-11 for Nafion 212 is typical of other, more conventional membrane systems. Such studies go back at least 25 years.[17,146-148] We have previously shown that it is typically the case for ion exchange membranes that the pore fluid composition is modified relative to the composition of the bathing solution, resulting in a peak at lower molarity than observed for the free acid. Also, the conductivity of typical membranes is significantly lower than that of the pure acid solution, which can exceed 0.5 S/cm at room temperature. These differences between membrane and solution behaviour likely reflect the influence of a high density of fixed charges in the membranes. Conduction through the confined charged pores is a complex phenomenon but our previous detailed studies suggest that the pore size and uptake of acid and water are primary factors. In the present instance, the pore size is large compared to that of Nafion or (especially) other hydrocarbon-based membranes with a

'naturally' formed pore structure. Therefore, it is surprising to find that the acid sites bound to the pore with such a large diameter have a great impact on conductivity.

The nanoporous PPSU62 membrane was further evaluated by charge/discharge cycling in a vanadium redox cell at 200 mA/cm^2 as shown in Figure 3-12a. The cycling data for the hydroxyl pore surface membrane showed high coulombic efficiency (0.90-0.97) which was comparable to Nafion 212, but fairly low voltage efficiency (0.76-0.80) within 20 cycles. Thus, overall energy efficiency of nanoporous PPSU62 was lower than 0.80. The high coulombic efficiency is of note since this indicates that the rate of cross-over was not particularly high under the experimental conditions. This lower voltage efficiency is probably a result of higher membrane resistance for the PPSU62. The initial improvement in the coulombic efficiency is likely due to the modification of material

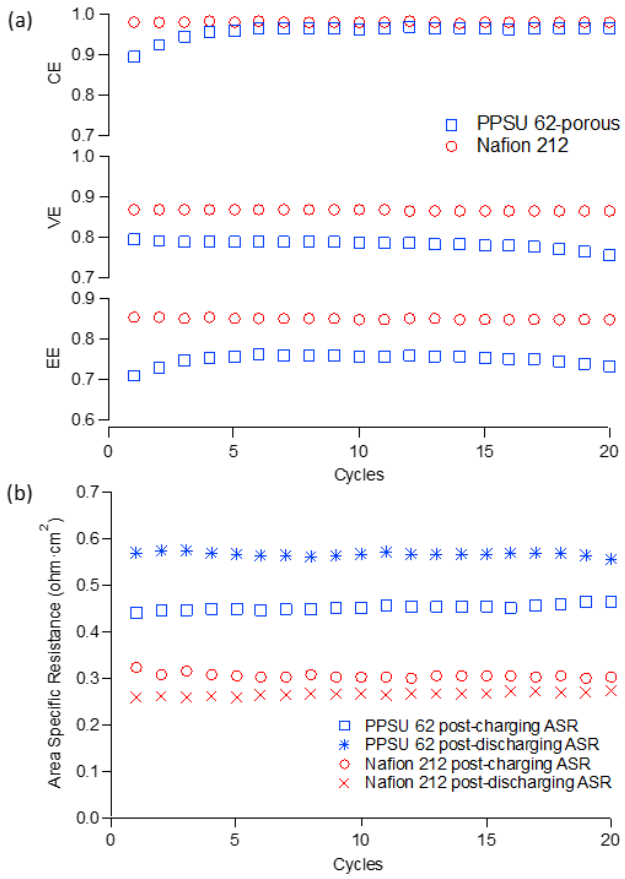

Figure 3-12 (a) VRFB cycling data for PPSU62 (square) and Nafion 212 (circle): Electrode, SGL 7013 (400->250 μm); Electrolyte, 50 mL, 1.7 M Vx+/5M sulfate; Temp: 23C; Flow rate: 50 mL/min. (b) Post-charging and post-discharging ASR of PPSU62 (square and star) and Nafion 212 (circle and x, respectively).

properties under cell test conditions, such as improvement in electrode wetting. However, it is also possible that an initial process of electrochemical clean-up of impurities left from the polymer synthesis is the source of this change.

A comparison of area specific resistances (ASR) of post-charge and post-discharge membranes, shown in Figure 3-12b, revealed apparent differences in post-charge and post-discharge ASR values for the nanoporous PPSU62 membrane in contrast to the closer ASR from Nafion 212. This change in the ASR between charged and discharged states is consistent with the previously reported resistance of electrolyte

solutions,[149] in which solutions containing vanadium (IV) in sulphuric acid exhibited significantly lower conductivity then those containing vanadium (V). Additional effects due to net water transfer across the membrane could also come into play. This will be explored in further investigations of cell behavior using this type of membrane.

3.4 Conclusions

In conclusion, functional nanoporous PSU membranes prepared by a novel approach using crosslinkable and degradable block copolymers exhibit unique performance and properties for RFB applications. Prior to any surface modification, the nanoporous membranes with hydroxyl groups on the pore showed an EE in a VRFB cell of 76% at 200 mA/cm^2, comparable to those of Nafion 212. Although the systematic studies by changing the PPSU/PLA block ratios and the degree of crosslinking on the membrane nano-morphologies, properties, and performance are currently underway, the results presented in this paper have demonstrated the potential of this block copolymer approach to prepare functional nano-porous membranes for energy storage devices and provided hints of some unexpected mechanistic aspects. In addition, a more complete suite of cell tests and related studies is underway.

Chapter 4

Controlled Nanoporous Polysulfone Membranes: The Effect of Different Pore Size and Morphology

The novel nanoporous PSU membranes from block copolymer precursors, established in the previous chapter, are further studied systematically in this chapter. Two series of nanoporous PSU membranes are synthesized and characterized using scattering and microscopy techniques to investigate their pore size and morphology derived by the self-assembly of their block copolymer precursor. The results will be correlated with electrochemical properties of those PEMs for more detailed understanding of the structural effect towards VRFB application.

4.1 Introduction

All vanadium redox flow battery (VRFB), has emerged as a front runner for next generation large scale energy storage.[132] VRFBs are highly efficient, durable, and easily scalable to specific site requirements. The battery functions by circulating two separate aqueous electrolyte solutions of vanadium in differing oxidation states though a central cell. During discharge a redox reaction occurs sending electrons from the negative half-cell to the positive half-cell through an external circuit performing work, and vice versa during charge. During this redox reaction protons traverse a proton exchange membrane (PEM) from one half-cell to the other maintaining charge neutrality and separation of the bulk electrolyte solutions.

A widely-used PEM is Nafion® or similar membranes, perfluorinated polymers containing sulfonic acid moieties. The membrane has a large effect on the overall performance of the battery and cost, making up to 11% of the cost of the entire

battery.[9,150] High cost of Nafion as well as other factors such as low proton selectivity is driving the research for other candidate membranes.[8,10,134,151] Porous membranes could offer the lower cost, but were the least studied in this system.[10,67] In general, uncharged nanoporous membranes lack the selectivity and conductivity of AEMs and PEMs respectively, but have been demonstrated recently to perform effectively.

Different membrane fabrication techniques such as phase inversion casting, have yielded high performance porous membranes.[152153] Phase inversion casting has been used on many other polymer systems which performed well. Many of these membranes were outlined in chapter 1 which showed the diversity of porous membranes that work in VRFBs.

The aforementioned membranes utilize a physical fabrication method to fashion a porous structure. Nanosized pores are more difficult to tailor and are normally made using lithography.[154] In contrast, the chemical methods can be used to produce porous membranes; specifically, selective degradation of block copolymers has been shown to be a popular method.[80,82,83,155] Polylactide (PLA) can be used as a sacrificial block that can be etched using mild base hydrolysis. This approach has been used to fabricate many nanoporous membranes from different block copolymers,[85,92,93] however, it has rarely been applied to robust condensation polymers. Only two examples are known in the literature: PLA incorporation onto a poly(arylene ether ketone) (PAEK) or onto a polyimide.[156-158] No annealing was used to promoted self-assembly with these high T_g blocks, limiting the development of long-range order.

Herein we describe the synthesis and characterization of tailored nanoporous polysulfone membranes (NP-PPSU) in VRFBs. This method was previously published by

our group and used polylactide-polysulfone-polylactide (PLA-PPSU-PLA) triblock copolymers (B-PPSU) to fabricate bicontinuous nanoporous membranes through selective PLA degradation.[159]. Morphologies of the series of nanoporous membranes and bulk polymers are characterized using SEM and SAXS to study the relationship of phase separated structures on performance in VRFB. Moreover, dual pore membranes possessing both macro- and nano-sized voids are prepared by combining microporous fabrication and selective block copolymer degradation to further explore the optimum structure and chemical modification for the VRFB application.

4.2 Experimental

4.2.1 Materials

Bisphenol A (BPA), dichlorodiphenyl sulfone (DCDPS), and rac-Lactide (purchased from Purac Biochem) were recrystallized twice from toluene. All polymerization solvents and 1,8-Diazabicyclo(5.4.0)undec-7-ene (DBU) were distilled one or more times over calcium hydride. All other reagents were used as received unless denoted otherwise.

4.2.2 Polymer Synthesis

All polymers were synthesized using a previously reported method.[159] An example polymerization of PLA-PPSU-PLA Mn = 44000 g/mol and weight fraction of PSU:PLA of 53:47 is described below.

Propenyl-functionalized polysulfone (PPSU) macroinitiator. BPA (42.5 mmol), 2,2'-diallylbisphenol A (7.5 mmol), DCDPS (48.9 mmol), and K_2CO_3 (60 mmol) were charged into a 3-neck flask equipped with a Dean-Stark trap, nitrogen inlet, and stir bar. 100 mL of N,N-dimethylacetamide (DMAc) and 50 mL of toluene were then added

and the reaction was refluxed for 4 h. Toluene was slowly distilled of by draining the Dean-Stark trap and heated at 170 °C for 12 h. The temperature was decreased and 4-fluorobenzaldehyde (10 mmol) was added and the reaction mixture was heated for another 6 h. After being cooled to RT, 25 mL of DMAc was added with $NaBH_4$ (20 mmol) and stirred for 2 h. The reaction mixture was centrifuged and precipitated three times into methanol and dried in vacuum before moving onto the next step.

Polylactide- Propenyl-Functionalized Polysulfone-Polylactide (PLA-PPSU-PLA) triblock copolymer. PPSU macroinitiator (0.175 mmol) and rac-lactide (31 mmol) was dissolved in 60 mL of dichloromethane (DCM) followed by addition of (0.31 mmol) of DBU. The reaction was quenched after 4 h by adding (0.4 mmol) of benzaldehyde then precipitated into diethyl ether twice.

4.2.3 Membrane Fabrication

Nanoporous membrane. Using different PLA-PPSU-PLA polymers, membranes were cast as previously reported.[159] An example is as follows: 1.5 g of PLA-PPSU-PLA was dissolved in 15 mL of DMAc/1 mL of 5.5 M t-butyl hydroperoxide in decane. The polymer solution was filtered onto a flat glass pane at 55 °C for 12 h, heated at 160 °C for another 8 h under nitrogen and slight vacuum, and finally heated at 185 °C for 10 h. The membrane was lifted from the glass in warm water and treated for up to 10 days in 1.5-3 M NaOH with sodium dodecyl sulfonate.

Dual pore membrane. Dual pore membrane preparation was done by phase inversion casting as follows: PLA-PPSU-PLA triblock copolymer was dissolved in DMAc. After dissolution, a predetermined amount of t-butyl hydroperoxide 70% in H_2O is added to give a final solution 14-18% w/v of polymer in 10% t-butyl hydroperoxide

solution. The solution was cast onto a flat glass sheet via filtration through wool. After the cast solution was kept for 10 minutes to fully spread along the glass, transferred to a chamber with 100% RH at 80 °C. The membrane immediately turned white during vapor induced phase inversion. After 20 minutes the membrane was removed from the oven and soaked in H_2O for 4 h. Finally, the membrane was annealed and hydrolyzed under the same conditions as nanoporous membranes.

4.2.4 Instrumentation

General. Nuclear magnetic resonance spectroscopy (NMR) was done on a Varian 500 Mhz spectrometer. Gel permeation chromatography (GPC) was performed on a Shimadzu LC-20AD with two Jordi DVB 5 μm particle size columns (250 × 10 mm) calibrated against polystyrene standards with a flow rate of 1.0 mL/min using a THF eluent at 35 °C. Thermal gravimetric analysis (TGA) and differential scanning calorimetry (DSC) was recorded using a TA instruments Q50 and TA instruments Q20 respectively. TGA experiments were done using a platinum pan, where samples were dried at 120 °C for min then heated from 30 to 600 ° C under a nitrogen purge. DSC experiments were cycled 3 times from 20 to 28- ° C at 10 ° C/min and cooled at the same rate. Attenuated total reflection Fourier transform infrared spectroscopy (ATR-FTIR) was run using a Perkin Elmer Frontier on neat membrane samples.

Small-angle X-ray scattering (SAXS). The measurement was done at the Advanced Photon Source (APS) on beamline 12-ID-B with an emission wavelength of 0.932 Å using a Pilatus 2M detector. Samples were run in air, Kapton tape, or quartz cuvette as specified. Irena was used to analyze all 1D SAXS curves.

Polymer powder and cast polymer membranes were analyzed using SAXS. Polymeric membranes could be placed directly in beam path as neat samples or in a quartz cuvette if a solution was needed. Powdered samples were wrapped in Kapton tape and placed in the beam path. The 2-D image obtained during analysis was azimuthally integrated to a 1-D plot and presented as intensity (I) versus scattering wave vector (q). $q = \frac{4\pi}{\lambda}\sin(\frac{\theta}{2})$ where θ is the scattering angle. SAXS data were analyzed using Irena software to fit all curves.[160]

Conductivity. Proton conductivity was calculated using impedance spectroscopy to obtain the resistance of a membrane sample using the equation below:

$$\sigma = \frac{L}{R \times A}$$

Where σ is the conductivity, L is the length between electrodes, R is resistance, and A is the cross-sectional area. Membranes were soaked acidic solution gradient for at least 24 h prior to measurements.

Scanning Electron Microscope (SEM). Samples were cut into 10-100 μm samples using an optical microscope and placed on conductive carbon tape. Gold sputtering was done on described samples for 20-300 seconds followed by cutting to remove the gold surface. Pt deposition and/or conductive copper tape was also used as needed to minimize charging issues. Imaging was performed using a SEM Zeiss-Auriga using in-lends modes at a working distance of 3-6 mm. Working voltages were between 0.5-5 kV.

4.3. Results and Discussion:

4.3.1 Nanoporous Polysulfone Preparations

Nanoporous membranes were prepared using self-assembled block copolymer membranes with a selectively degradable PLA block. Following PLA-PPSU-PLA synthesis and membrane casting, PLA was degraded in mild base and removal was monitored using ATR-FTIR noting the disappearance of the carbonyl stretching band at 1750 cm^{-1} in Figure 4-20.

Two series of nanoporous polysulfone membranes (NP-PPSU) were prepared with differing morphology and porosity. In the first series, the PPSU:PLA ratio (fraction, *f*) was varied to investigate the pore size, structure, and continuity in the resulting nanoporous membrane as shown in Figure 4-1. In the second series of NP-PPSU membranes, the ratio of non-crosslinkable monomer (BPA) to crosslinkable monomer (2,2'-diallyl BPA) was increased to raise the degree of crosslinking in the final membrane.

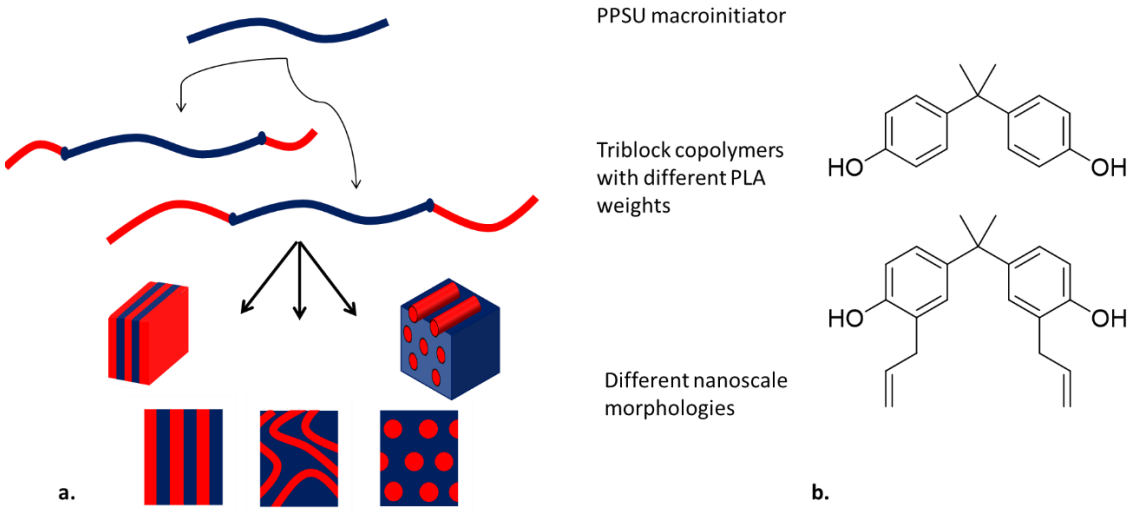

Figure 4-1 a) Schematic of different PLA-PPSU-PLA triblock copolymers (B-PPSU). B) top, Bisphenol A (BPA) (noncrosslinkable monomer), bottom, 2,2'-diallyl BPA(crosslinkable monomer)

The first series of membranes targeting different weight fractions of PPSU:PLA blocks was synthesized by polymerizing a PPSU macroinitiator with a targeted molecular weight (M_n = ~23,000 g/mol). Afterwards, this same initiator was used to make triblock copolymers with different PLA molecular weights. The different weight fractions are shown in the horizontal box of Figure 4-2, spanning a 50-70% weight fraction of PPSU, f_{PPSU}. This range was chosen for targeted bicontinuous morphologies which can minimize "dead-end" channels when used as a VRFB separator. If the f_{PPSU} is too high spherical or poorly connected channels can form, and if it is too low (below 50%), poor mechanical properties develop. These limitations set the minimum and maximum f_{PPSU} at 50 and 70%.

Besides PPSU:PLA ratios, the degree of crosslinking in the polysulfone block would affect the final NP-PPSU morphology and properties such as: 1) retention of nanostructure during PLA block degradation, 2) durability of the membrane during VRFB cell cycling, and 3) membrane strength. The degree of crosslinking was controlled for series 2 membranes by adjusting 2,2'-diallyl BPA from 5-25% seen in the vertical column of Figure 4-2. To minimize the effect of f_{PPSU}, all block copolymers for this series were synthesized with a 50% weight fraction of PPSU.

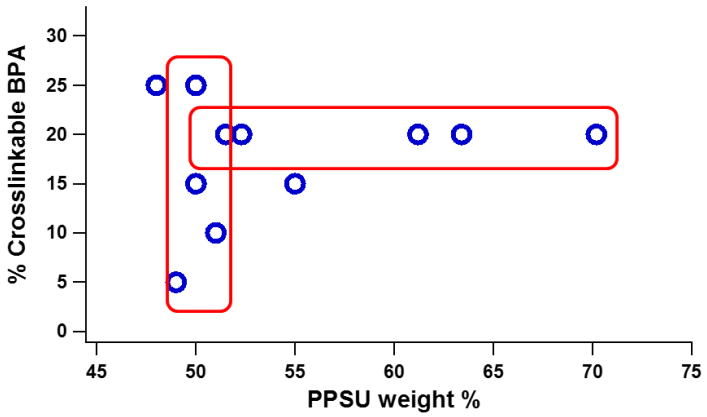

Figure 4-2 PLA-PPSU-PLA synthesized copolymer weight fraction (horizontal box) vs ratio of crosslinkable BPA (vertical box).

4.3.2 PLA-PPSU-PLA Triblock copolymer

All polymers were characterized by ^{1}H NMR and GPC shown in Table 4-1, Table 4-2, Figure 4-18, and Figure 4-19. The membranes morphology was studied using SEM and SAXS. Five different PPSU macroinitiators were synthesized termed H-PPSU-X# (H- for homopolymer), where X# denotes the ratio of crosslinkable BPA to standard BPA as summarized in Table 4-1. The end group analysis by ^{1}H NMR confirmed the agreement of molecular weights with the theoretical molecular weight which was based on the feed ratio of the monomers; however, GPC gave relatively low M_n compared to data by ^{1}H NMR. This is a result of the GPC column being calibrated against polystyrene, a physically different polymer from PPSU. Also, the PDI of the PPSU macroinitiator was relatively high because it was synthesized by ordinary polycondensation.

Table 4-1 Polysulfone macroinitiator (H-PPSU-X#) polymer index

Sample #	Macroinitiator ID	BPA:XL-BPA Ratio	Phenol:Halide Ratio	H-PPSU M_n (^{1}H NMR)	H-PPSU M_n (GPC)	PDI
1	H-PPSU-X5	95:5	46:45	20000	12085	2.63
2	H-PPSU-X10	90:10	46:45	24000	13008	2.65
3	H-PPSU-X15	85:15	46:45	23000	14596	2.80
4	H-PPSU-X20	80:20	46:45	23431	13774	2.88
5	H-PPSU-X25	75:25	46:45	19500	12722	2.86

PLA was polymerized using controlled ROP of lactide onto the PSU macroinitiator, that generated the PLA-PPSU-PLA triblock copolymers. They are abbreviated here as B-PPSU(1)-X(2) (B- for block), such that (1) represents PPSU block weight faction and (2) is again crosslinker monomer feed. Table 4-2 shows the molecular weight and weight fraction of the triblock copolymers. Sample numbers 6-10 have different PLA fractions using the same macroinitiator. Sample Number 10-14 represents different degrees of crosslinkable polysulfone units within the polymer. This series all have a PPSU weight fraction close to 50% so only variable in that series is crosslinking capacity. All triblock copolymers show a large decrease in PDI, over 40%, after PLA polymerization for all triblock copolymers due to the nature of ROP being a controlled polymerization compared to PPSU's uncontrolled polymerization.

Table 4-2 PLA-PPSU-PLA triblock copolymer molecular weight

Sample #	Triblock Polymer ID	PPSU volume fraction, f^a (%)	PPSU wt.%	XL Ratio	B-PPSU M_n (^{1}H NMR)	B-PPSU M_n (GPC)	PDI
6	B-PPSU51-X20	51.7	51.5	20	44431	40648	1.67
7	B-PPSU53-X20	52.5	52.3	20	44700	41671	1.69
8	B-PPSU61-X20	61.4	61.2	20	38200	33403	1.72
9	B-PPSU63-X20	63.6	63.4	20	37000	35047	1.69
10	B-PPSU70-X20	70.3	70.2	20	33223	30938	1.71
11	B-PPSU49-x5	49	49	5		38648	1.46
12	B-PPSU51-x10	51	51	10		42737	1.43
13	B-PPSU55-x15	50	50	15		38366	1.58
14	B-PPSU48-X25	48	48	25		38291	1.69

[a] Calculated using PPSU and PLA literature densities of 1.24 and 1.248 g/cm^3 (amorphous) respectively[161]

4.3.3 Membrane Morphology

The PLA-PPSU-PLA block copolymer synthesized in this study is unique and can be distinguished from many commercially available block copolymers due to the significant contrast in physical and chemical properties between PSU and PLA blocks. For instance, one of the blocks is made from polycondensation (a high PDI polymer) while the other block is made from a controlled ROP (a low PDI polymer). Also, PPSU has a glass transition temperature (T_g) of 180 °C, much higher than PLA's T_g of 54 °C.

Although PPSU-b-PLA is such a challenging system, proper phase separation is crucial for the latter formation of controlled nanoporous materials. Thus, understanding this thin window between phase separation and PLA degradation is imperative for controlling the final morphology. SAXS was used to study the morphology of the final membranes, the triblock copolymer itself, and the multiple treatment methods needed to produce the final membrane. Additionally, PLA-PPSU-PLA polymers prior to membrane

formation were analyzed by SAXS as a function of temperature to monitor it's self-assembly and validate the membrane fabrication method.

Table 4-3 NP-PPSU SAXS overview

Sample #	Membrane ID	PPSU volume fraction (%)	q* x10^{-2} (Å^{-1})[a]	d* nm	Morphology[b]
15	NP-PPSU51-X20	51.7	2.05	30.7	LAM
16	NP-PPSU53-X20	52.5	2.05	30.7	LAM
17	NP-PPSU61-X20	61.4	2.40	26.2	LAM?
18	NP-PPSU63-X20	63.6	2.55	24.6	LAM
19	NP-PPSU70-X20	70.3	2.80	22.4	CYL?
20	NP-PPSU49-X5	49	1.85	34.0	LAM
21	NP-PPSU51-X10	51	1.90	33.1	LAM
22	NP-PPSU55-X15	50	1.85	34.0	LAM
23	NP-PPSU48-X25	48	2.20	28.6	LAM

[a] Determined from first large scattering peak in SAXS
[b] Morphology determined by SAXS analysis

4.3.3.1 Temperature-dependent SAXS

SAXS experiment was performed to investigate the *in-situ* phase separation process of as-synthesized powder form of the triblock copolymers, B-PPSU prior to membrane processing. Figure 4-3 shows scattering curves of a powder sample of B-PPSU51-X20 in a Kapton film, during thermal annealing from RT to 200 °C. A scattering curve was collected after 10 minutes of equilibrating at a given temperature while ramping at 10 °C increments. At low temperatures, there is no clear phase separation embodied by the lack of a primary scattering peak (q*). When the temperature reaches 160 °C a small hump around 0.035 Å^{-1} appears. As the temperature surpasses 160 °C, the q* peak shifts towards lower q values and becomes more evident shown in Figure 4-3. After reaching 200 °C, q* shifted to around 0.25 Å^{-1} and is clearly a broad distinguishable peak. The final q* at 0.25 Å^{-1} is representative of a domain spacing of 27 nm.

The secondary peaks are not detectable to determine further structural information since the polymer is not fully ordered and background scattering is high because of the powder sample. It is probable that the polymer morphology is disordered from the quick annealing treatment leading to microphase separation, but not long enough for long-range order to develop. After heating the overall intensity at the onset (0.01 $Å^{-1}$) was reduced by close to 2 orders of magnitude. This is due to some "membrane processing" during the heat treatment which greatly reduced background scattering caused by power samples. Temperature-dependent SAXS experiments on the block copolymer put forth experimental evidence that the multistep membrane fabrication step is required to achieve a final phase separated membrane having long-range order. During membrane fabrication, membranes were annealed at 160-170 °C for 8 h and further crosslinked at 180-190 °C for another 8 h. This high temperature range shows fully phase separated domains by SAXS that are "locked in" via *in situ* crosslinking.

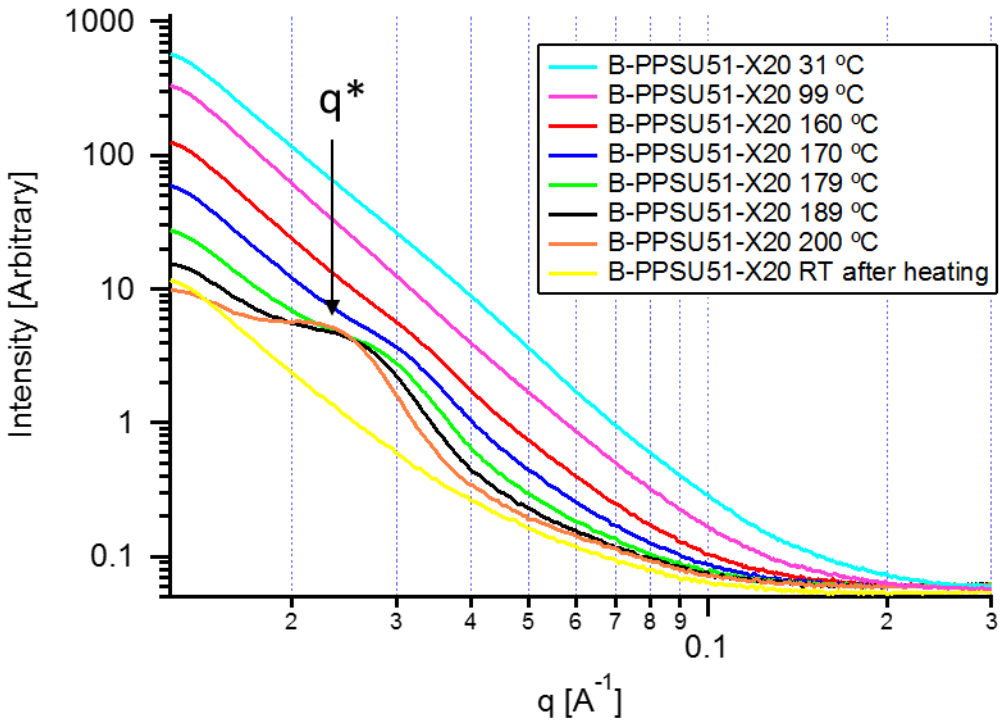

Figure 4-3 B-PPSU 51-X20 powder SAXS curves during thermal treatment.

4.3.3.2 Series 1: PPSU fraction, f_{PPSU}

The primary objective of this study was to see how pore size and morphology that can be tailored as VRFB membrane separators. As shown in Figure 4-4, SAXS profiles of nanoporous membranes varied from a f_{PPSU} of 51 to 70% revealed a shift of the primary scattering peak. As f_{PPSU} increases, the average domain size decreases reflected by an increase in q*. The primary scattering peak was identified after fitting the curve and the results are shown in Table 4-3. The q*, used to calculate average domain spacing, showed as the PPSU weight fraction increased, the domain spacing decreased from 31.4 nm to 22.4 nm.

The nanoporous membranes showed secondary scattering peaks in their SAXS curves from the presence of long-range order. NP-PPSU51-X20 has two secondary scattering peaks at q/q* of 2 and 3 revealing a lamella orientation. Lamella morphology is

well known and characterized by a q/q* pattern of 1, 2, 3, 4, 5… NP-PPSU70-X20 has one visible peak past its primary scattering peak at $\sqrt{3}$. Hexagonally packed cylinders give secondary scattering at q/q* at 1, $\sqrt{3}$, 2, $\sqrt{7}$, 3… It is likely that NP-PPSU70.2-X20 has cylindrical morphology, but there are too few secondary scattering peaks to confirm. SAXS of the hydrolyzed membranes clearly shows reduction in domain spacing as well as changing of the morphology and is expected to affect the battery significantly.

Morphology of series 1 membranes was observed using SEM. Figure 4-5 shows uncoated surface of a cross section of all membranes (left images) and cracked membrane view projected from the Pt coated surface. These micrographs show distinguishable nano-porous morphology with polymer domain size about 10-30nm ranges. Although, the magnification of x100k was achieved by metal coating, the detailed size and morphological differences depending on f_{PPSU} were not possible to be identified. Gold coated samples show higher resolution to view the detailed morphological information as shown in Figure 4-22 for NP-PPSU-x20 membrane. The higher resolution images of NP-PPSU membranes indicated uniform lamellar-like rods structure, which showed good agreement with SAXS data shown above.

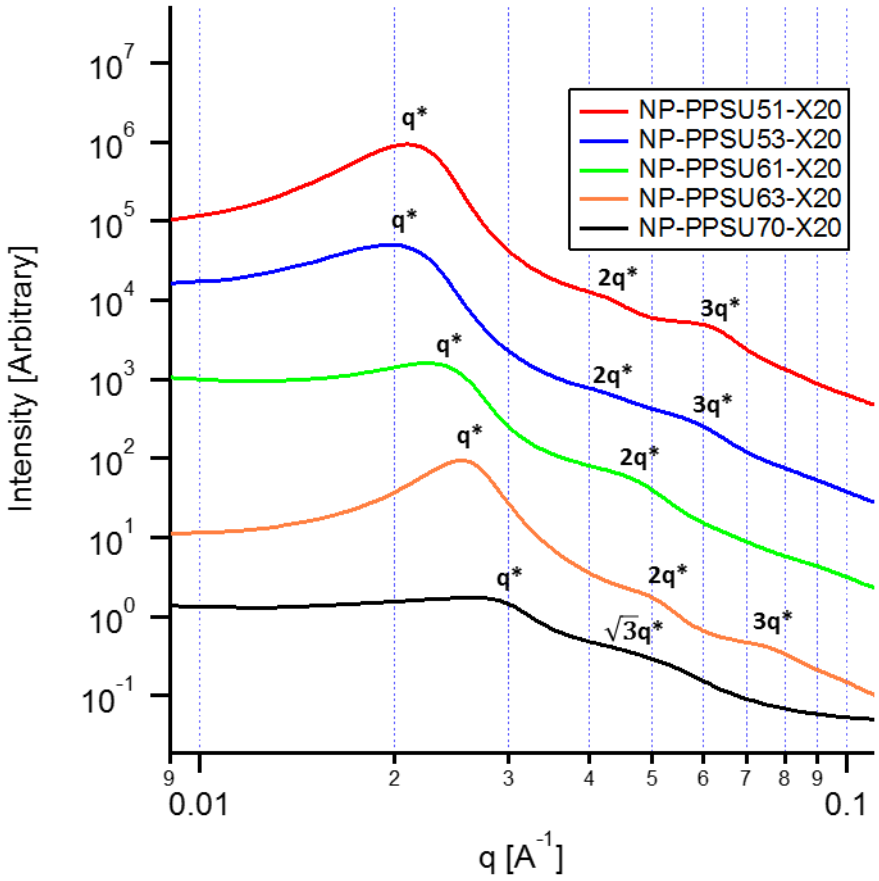

Figure 4-4 SAXS profiles of NP-PPSU membranes with different weight fractions.

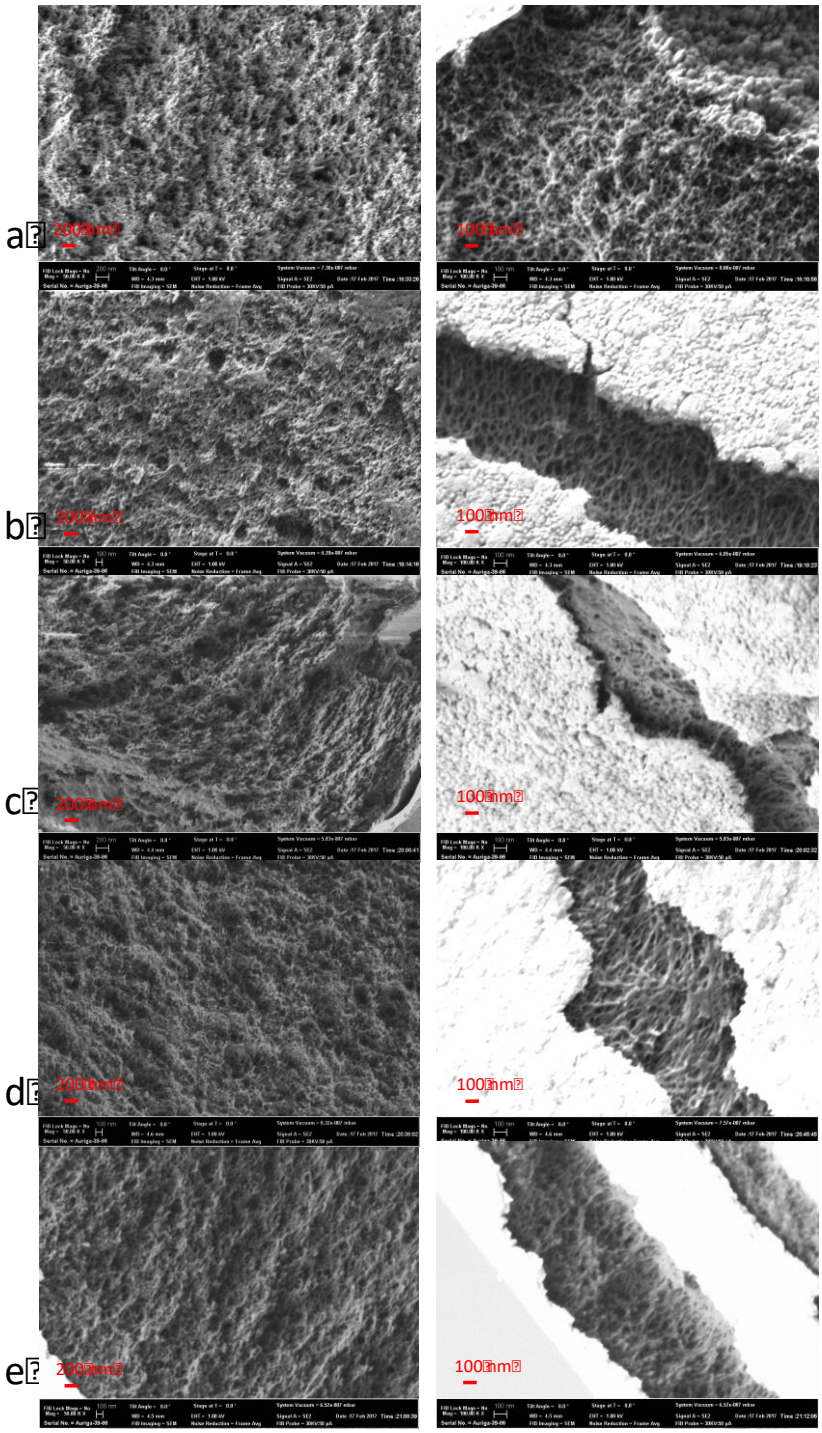

Figure 4-5 SEM images of series 1 NP-PPSU membranes: a) NP-PPSU51-X20, b) NP-PPSU53-X20, c) NP-PPSU61-X20, d) NP-PPSU63-X20, e) NP-PPSU70-X20; (left) untreated cross section at x50k Mag, and (right) inside membrane projected from Au or Pt coated surface at x100k Mag.

4.3.3.3 Series 2: Crosslink fraction

The morphology of the NP-PPSU with differing degrees of crosslinkable BPA was analyzed by SAXS in Figure 4-6 showing BPA:2,2'diallylBPA of 95:5 to 75:5. The primary scattering peak for 5-15% crosslinkable BPA remained constant around 0.0175 $Å^{-1}$ corresponding to a domain size of 35.9 nm. The secondary scatting peak around 0.035 $Å^{-1}$ did not shift either though its relative intensity and visibility changed. Increasing the crosslinker to 20 and 25% shifted the primary scattering peak to 0.0205 and 0.0220 $Å^{-1}$ respectively, corresponding to a domain size of 30.6 nm and 28.6 nm. Again, the secondary scattering peaks show a q/q* of 1, 2, 3… ratio corresponding to a lamellar morphology. The crosslinker content changed domain size, but not shape. As crosslinker content is increased visibility of the secondary peaks becomes more evident. This represents an increase in long range order and is a direct effect of having a more efficiently "locked in" morphology during thermal crosslinking.

GPC in Figure 4-24 shows the molecular weight of these polymer is nearly identical meaning the change in domain spacing is from 2,2'-diallylBPA incorporation. This monomer could affect the morphology by: 1) the 2,2-'diallylBPA causes a change in PPSU density leading to a change in $f_{PPSU,}$ or 2) the actual crosslinking during high thermal treatment (180 °C) locks in a more narrow domain spacing. Incorporating up to 25% 2,2'-diallylBPA can change the polymer properties since the monomer composition is different than traditional PSU. See thermal analysis below.

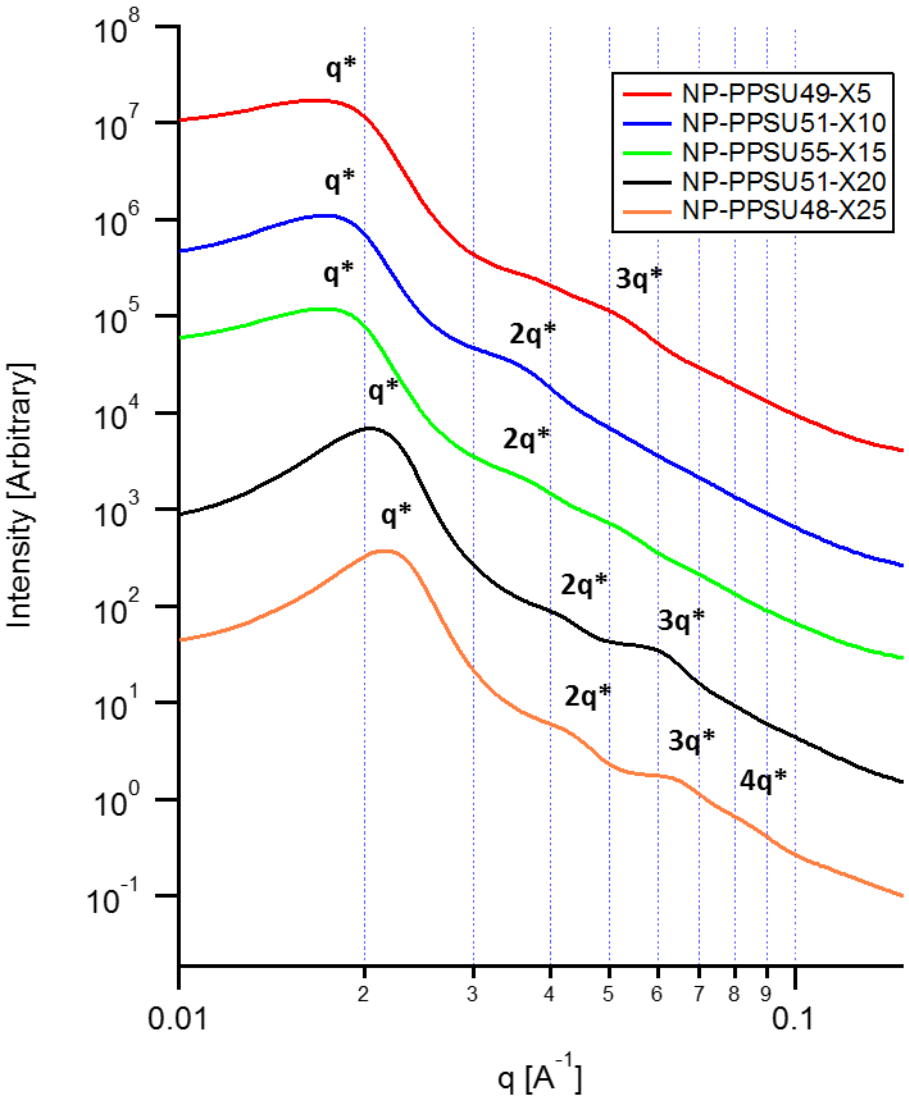

Figure 4-6 SAXS curve of NP-PPSU membranes of different crosslinking content.

4.3.3.4 Cycling effect on morphology

NP-PPSU63.4-X20 was studied in the battery electrolyte solution to see how the morphology is effected in the actual battery environment. The electrolyte solution contained 1.7 M vanadyl sulfate and 3.3 M sulfuric acid. After soaking the membrane in the electrolyte solution, there was a small reduction in the d spacing decreasing from 24.6 nm to 22.0 nm as seen in Figure 4-7. The secondary scattering peak pattern remains the same revealing there was no change in morphology. However, it was accompanied by

widening of the q* peak. This slight shift in scattering peaks could be an effect of analysis in air vs in solution. Measurements were made as a function of time showing the SAXS curve in the electrolyte solution did not change after over 1 h of soaking.

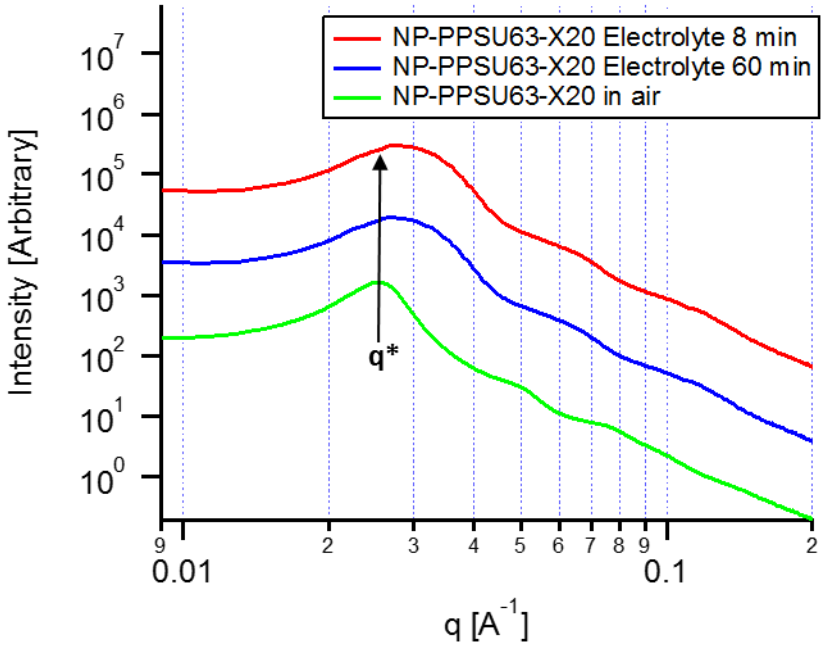

Figure 4-7 NP-PPSU63-X20 in air vs in electrolyte solution over time.

4.3.4 Thermal analysis

The stability of NP-PPSU was further analyzed by thermal gravimetric analysis (TGA) and differential scanning calorimetry (DSC). The TGA curve of NP-PPSU63.4-X20 in Figure 4-8 shows a 5 and 10% weight loss temperature of 403 and 433 °C, respectively. This 5% weight loss temperature is below that of commercial PSU (Udel®) which is over 450 °C.[162] This reduced initial thermal stability is due to incorporation of the crosslinking monomer decomposition than the rigid aromatic background. The TGA traces of block polymer, crosslinked membrane, and hydrolyzed membrane are all thermally stable below 250 °C proving the fabrication process is safe for the polymer. This also shows the membranes are stable over thermal conditions of the VRFB.

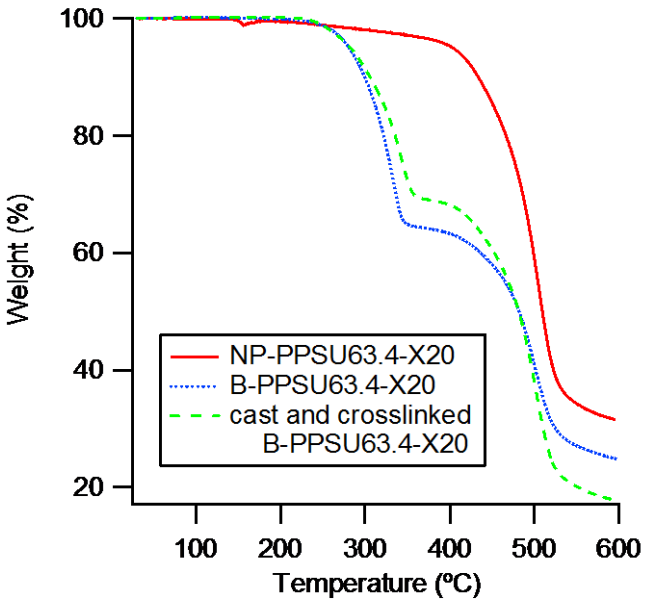

Figure 4-8 TGA curves of a) NP-PPSU63-X20, b) TGA B-PPSU63.4-X20, c) TGA B-PPSU63.4-X20 cast and hydrolyzed prehydrolysis membrane run from 30 – 600 °C at 10 °C min^{-1}.

A DSC curve of the same NP-PPSU polymer from above, NP-PPSU63.4-X20, is shown in Figure 4-9. The solid line and dashed line represent the heating ramp on the 1st and 2nd cycle respectively. The first cycle shows a clear exothermic peak at 176. This irreversible exothermic transition comes near the T_g onset and is completely gone in the 2nd and further scan. This exotherm comes from rearrangement or repacking of PPSU chains that have now free end groups. This small transition was the first time the polymer had the opportunity since the phase separation process of PPSU/PLA blocks before PLA hydrolysis. This is further proof that NP-PPSU possesses a porous nanostructure that is "locked" as phase separation morphology unless heated to the T_g of PPSU, but can be lost above this temperature.

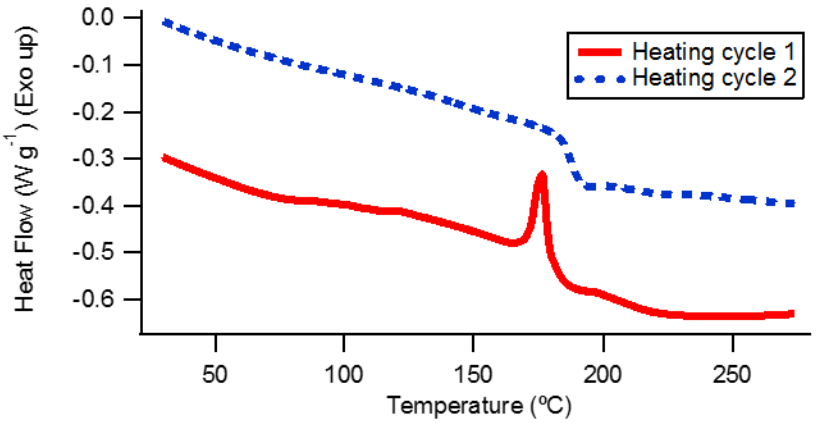

Figure 4-9 DSC curve of NP-PPSU63-X20: solid line) heating cycle #1, dashed line) heating cycle #2.

4.3.5 Conductivity

Three of the porous membranes had conductivity analysis run in a sulfuric acid gradient. NP-PPSU-52.3-X20, the lowest f_{PPSU} series 1 membrane analyzed, showed the highest conductivity as seen in Figure 4-10. As f_{PPSU} increases the conductivity of the membranes decreases due to decreasing pore volume. This is a result of increased electrolyte uptake providing more ion exchange groups in the membrane. The conductivity in 4 M H_2SO_4 is higher than Nafion 212 for 2 of the 3 membranes cycled. The uncharged surface of the membrane causes a considerable difference in conductivity compared to Nafion 212. After the membranes peak conductivity is achieved around 4 M H_2SO_4, it remains level while Nafions decreases. Vanadium permeability and cycling analysis will give detailed information on the effect of pore structure and turbidity effects on the battery and are underway now.

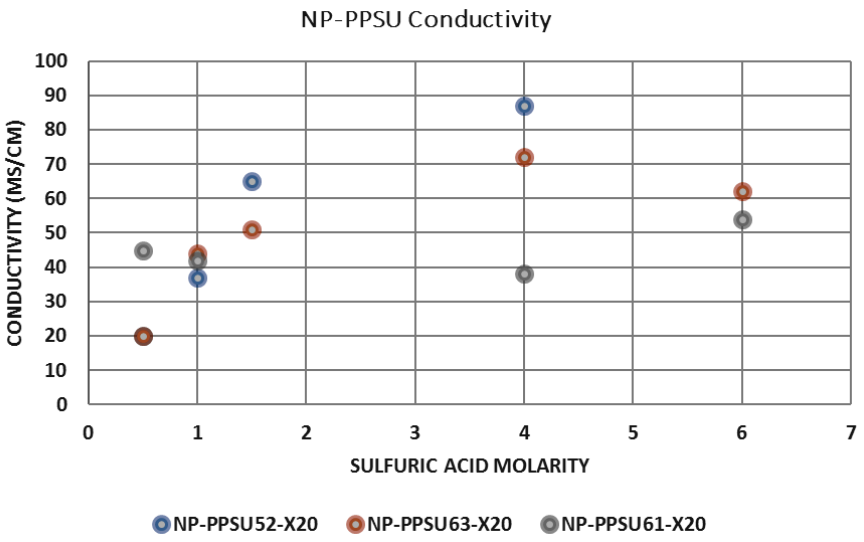

Figure 4-10 Conductivity of NP-PPSU membranes in a sulfuric acid gradient

4.3.6 Effect of B-PPSU polymer length

Series 1 and series 2 membranes were prepared using PPSU of similar molecular weight at 22,000 g/mol. One NP-PPSU sample was prepared using H-PPSU at ~45,000 g/mol (double D_p as the other samples) with maintaining comparable porosity to observe effect on domain spacing and morphology and is summarized in Table 4-4.

Table 4-4 NP-PPSU using large PPSU block. M_n compared to other previously described membranes

Sample #	Membrane ID	PPSU weight fraction	H-PPSU M_n	B-PPSU M_n	q* x 10^{-2} ($Å^{-1}$)	D* nm
24	Large-NP-PPSU60-X20	51.5	47025	91375	1.25	50.3
15[a]	NP-PPSU51-X20	51.7	23431	44431	2.05	30.7
18[a]	NP-PPSU63-X20	63.6	23431	37000	2.55	24.6

[a] reposted from previous tables

SAXS curves from Figure 4-11 show the q* of Large-NP-PPSU60-X20 was at a much lower q than the previous samples. This low q* of 0.125 Å corresponds to a domain spacing of 50.3 nm. The SAXS curve illustrates how doubling the molecular weight while keeping the f_{PPSU} fraction the same causes q* to shift from 0.0205 to 0.0125 $Å^{-1}$ for Large-NP-PPSU60-X20 to NP-PPSU63.4-X20. This corresponds to an increase in average domain spacing from 24.6 nm to 50.3 nm, a linear increase. Figure 4-11 also shows a loss of secondary scattering peaks that were evident in the short NP-PPSU curves. This shows a loss of long range order accompanied with the broadening of the q* peak. This disordered bicontinuous morphology is more favored at higher degrees of polymerization. This further illustrates the diversity of pore control in this system as membranes with pores between 20-50 nm have been selectively prepared.

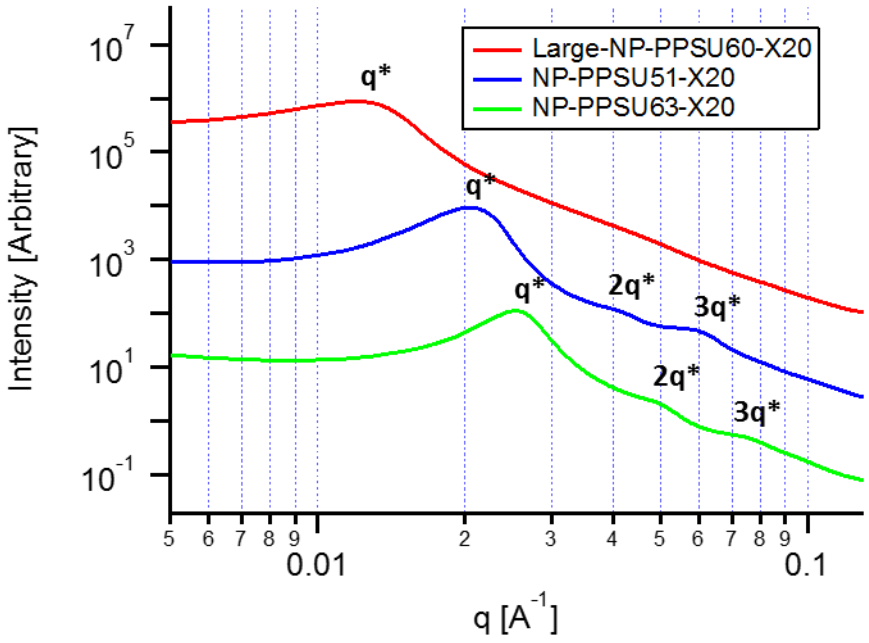

Figure 4-11 NP-PPSU showing different molecular weights (circle and square) and different f with same PPSU block (square and triangle).

4.3.7 Dual pore PSU membranes

Two different membranes were prepared adjusting the concentration of the casting solution giving membranes of different thicknesses, summarized in Table 4-5. Hydrolysis was monitored by IR.

Table 4-5 Dual pore PPSU nanoporous membranes

Sample #	Membrane ID	Polymer	Concentration %	% t-butyl hydroperoxide	Time in climate chamber	Membrane thickness
25	DP1	PPSU63.4-X20	14.2%	0%	12 minutes	0.20 um
26	DP2	PPSU63.4-X20	16.4%	10%	12 minutes	

Membrane morphology on the micro- and nano- level was determined through SEM and SAXS. SEM images depicting micro- sized features of membranes, as-cast and after hydrolysis of PLA block, are shown in Figure 4-12 and Figure 4-22.They show a thin

skin layer on the surface of the membrane made up of spherical PPSU clusters. The skin layer is around 5 μm thick and is uniform. The cross section of the membrane shows a bicontinuous micro-porous structure with 2-4 μm voids separating PPSU rods for DP1 membrane and 4-5 μm voids separating PPSU rods on DP2 membrane. The size difference of microstructure between DP1 and DP2 was due to the processing conditions. Changing the concentration of the cast solution and incorporating radical initiator gives control over resulting membrane thickness and microporous morphology.

After hydrolysis, the microstructure remains intact, although clear differences in the micrographs are evident. The broken ends of the rods appear more jagged after hydrolysis in contrast to the flatter ends from fracturing prehydrolysis. This visual effect, though caused from sample processing, is indirect evidence of a large physical difference in pre- and post- hydrolysis samples. The microporous domain spacing remains largely unchanged after hydrolysis, the most striking difference is the contrast of the PPSU vs void space. Post hydrolysis samples appear “more white” due to decreased contrast in the two phases. This is a result of PPSU rods being “hollowed” out as depicted in Figure 4-13. since up to 50% of the atomic density has been removed which is complemented by SEMs high ‘depth of field’.

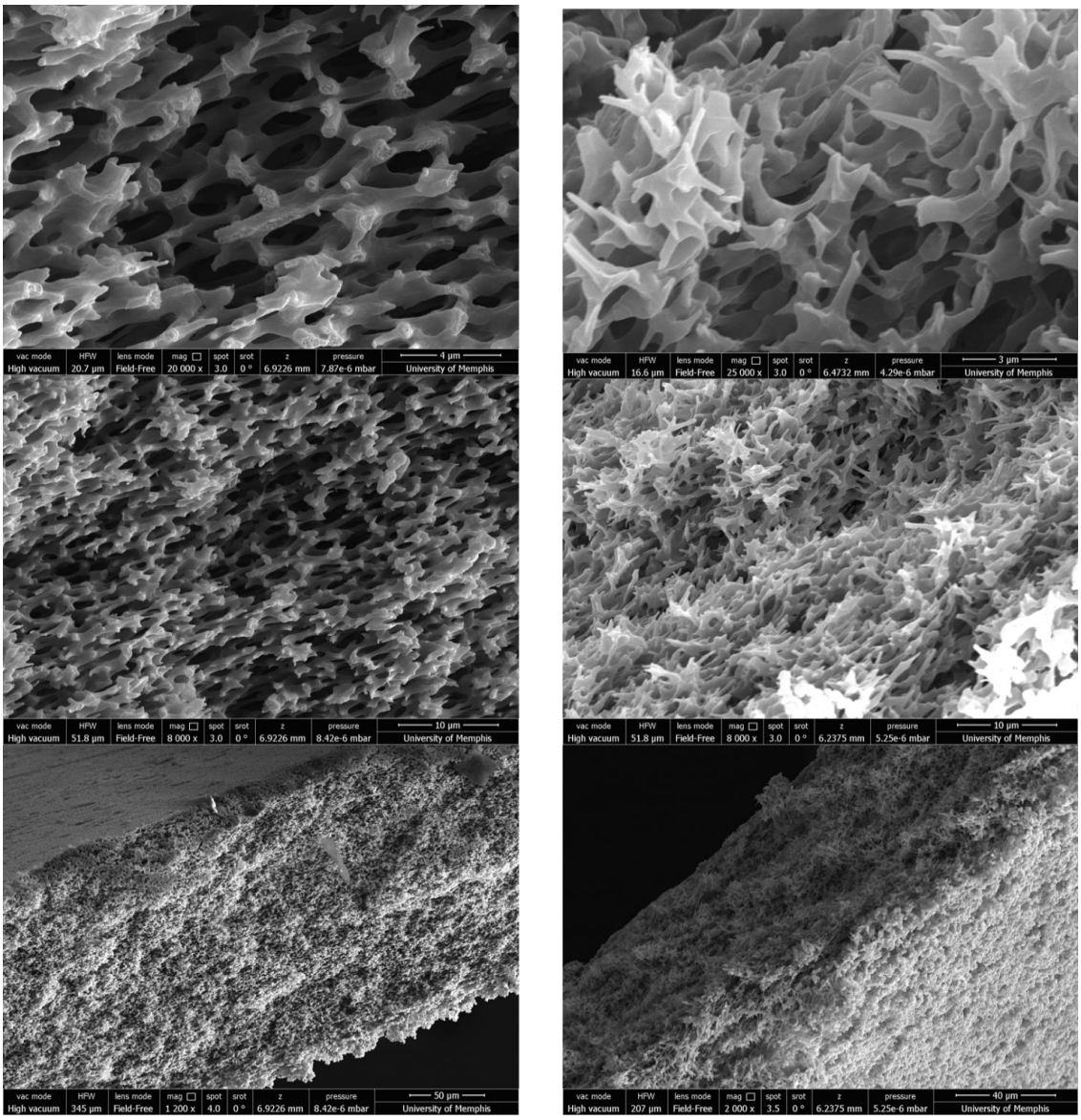

Figure 4-12 SEM images of dual pore PSU, DP1 (sample #25) of left) as cast membrane, right) post hydrolysis.

SAXS experiments were run on the samples: 1) as cast, 2) hydrolyzed without annealing, and 3) annealed and hydrolyzed (normal procedure.) Figure 4-14 shows nonhydrolyzed membranes have no distinct peaks as a results of low electron density contrast, the same results seen in NP-PPSU membranes. Both annealed and not annealed membranes show a clear q* peak after hydrolysis with different secondary scattering. The secondary peaks shift because of improved phase separation from the annealing step. SEM as well as SAXS has shown phase separation for samples not annealed at 180 °C (slightly over T_g of PPSU block), but the annealed sample does show more evident ordered orientation in SAXS. Overall, the annealing stage might not have a much effect on the domain spacing, but can clearly improve long-range order.

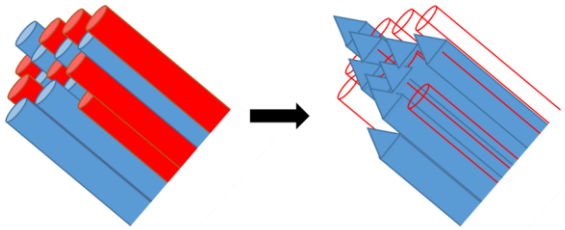

Figure 4-1 Animation depiction of pre and post hydrolysis dual pore membrane microrods.

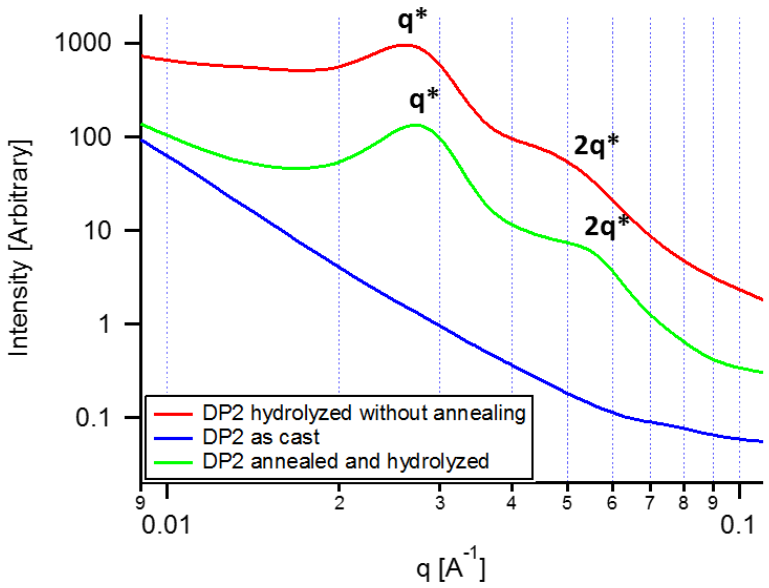

Figure 4-14 SAXS analysis of DP2 under different treatment conditions. Intensity axis was offset.

High resolution SEM images were obtained on the membranes before and after hydrolysis as shown in Figure 4-15 after sputter coating samples for 50 seconds with gold. The membranes show distinct lamellae orientation on the surface before and after hydrolysis. Due to the lengthy sputter coating time, the gold has a thicker coating on the surface. Despite a thicker coat the phase separation is still visible for nonhydrolyzed samples showing PPSU domain sizes of roughly 25-35 nm in agreement with SAXS measurements. Prehydrolysis PPSU also shows the cross section of a fractured PPSU rod with similar domain sizes. The phase separation is more evident from the different affinity PPSU and PLA have for gold which led to high contrast. After hydrolysis samples showed similar morphology, but the visibility decreased as only PPSU remained so pores and voids were filled evenly.

DP1 and DP2 are compared in Figure 4-16 showing identical scattering peaks with only the intensity differing. This intensity difference might simply be due to the

thickness of the membranes being different causing increased or reduced scattering. The peak profiles also appear the same showing a lamellar like orientation at q spacing's equal to 1, 2, and 3. NP-PPSU63-X20 is a membrane cast from the sample polymer as DP1 and DP2. As shown in Figure 4-16, the domain sizes of the nanoporous and dual pore membranes agreed with result in the SEM images (Figure 4-15). SAXS data showed the average pore diameters of 23-25 nm. SEM images also indicated a lamellae morphology both before and after crosslinking which is in high agreement with SAXS peak pattern. Additionally, the AFM and TEM images reported in chapter 3 for the lamellae phase separated PLA-PPSU-PLA triblock copolymer resemble Figure 4-15. Table 4-6 below emphasizes the relation between both SAXS and SEM structural analysis. Ensuing cycling, conductivity, and crossover analysis of these membranes can be evaluated against morphological data for the first ever systematic analysis of nanoporous membranes in VRFBs.

Table 4-6 Nanopore size and structural comparison by SAXS and SEM

Membrane	**Domain Spacing from SAXS (nm)**	**Domain Spacing from SEM (nm)**	**Morphology from SAXS**	**Morphology from SEM**
NP-PPSU51-X20	30.7	20-30	LAM	LAM
NP-PPSU53-X20	30.7	20-30	LAM	LAM
NP-PPSU61-X20	26.2	15-30	LAM	LAM
NP-PPSU63-X20	24.6	15-30	LAM	LAM
NP-PPSU70-X20	22.4	15-30	CYL	N/D
DP1	22.8	30-50	LAM	LAM
DP2	23.3	30-50	LAM	LAM

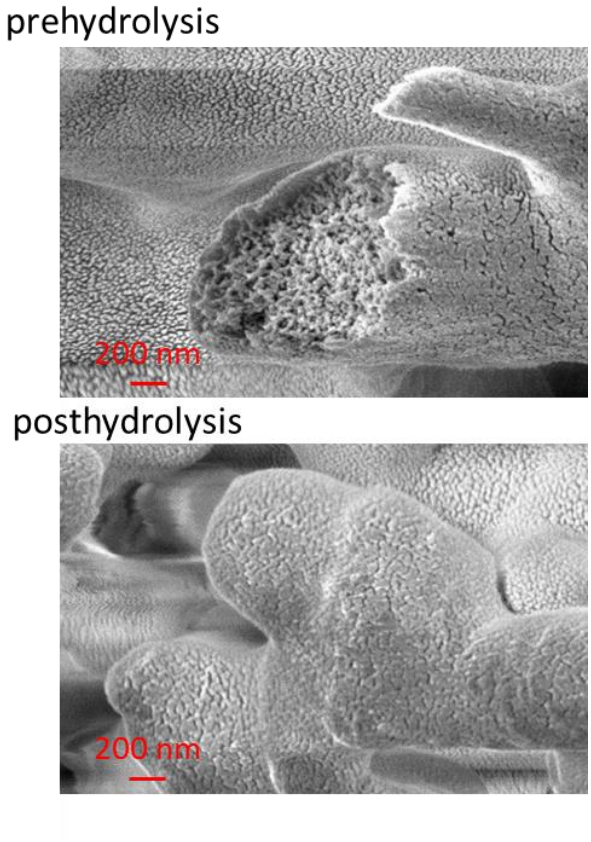

Figure 4-15 SEM images of Au sputtered dual pore membranes. Top) DP2 prehydrolysis, Bottom) DP1 post hydrolysis.

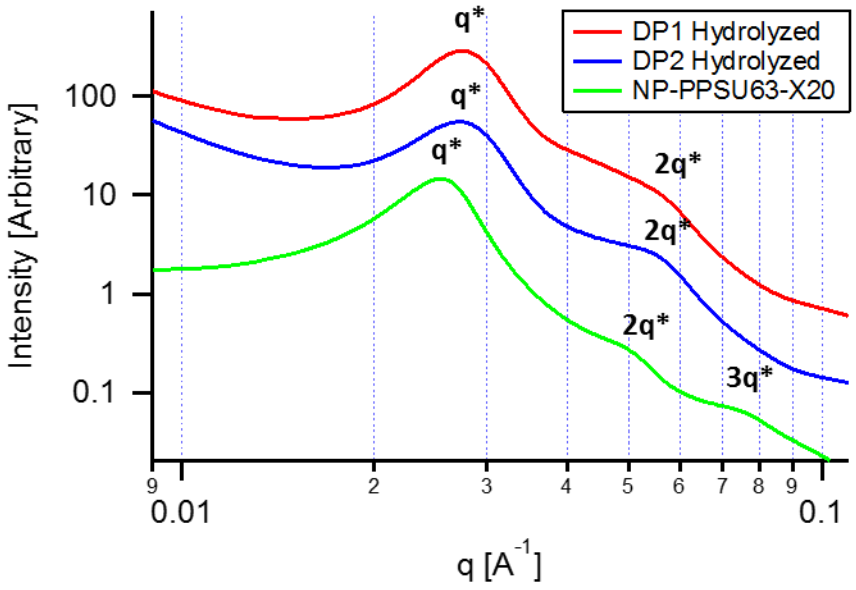

Figure 4-16 Offset SAXS curves of dualpore membrane and equivalent nanoporous membrane.

Both dual pore membranes and nanoporous PSU membranes were tested for dye uptake using methylene blue. The results are shown visually in Figure 4-17. A large difference in retention of the dye can be seen on the membranes pre and post hydrolysis. Membranes a and c show microporous membranes of nonhydrolyzed DP1 and commercial PSU respectively. Neither membrane takes up much of the dye. Membranes b and d both have nanopores via hydrolysis of DP1 and np-PPSU64-X20 respectively. After soaking in H_2O for more than 24 h, the membranes keep a dark blue color showing little loss of the methylene blue dye after it has been taken up into the pore. This experiment clearly shows the added layer of functionality given by combining the nano and micro pores in one membrane. Further battery cycling could reveal very interesting results of improved CE and VE over the porous membranes.

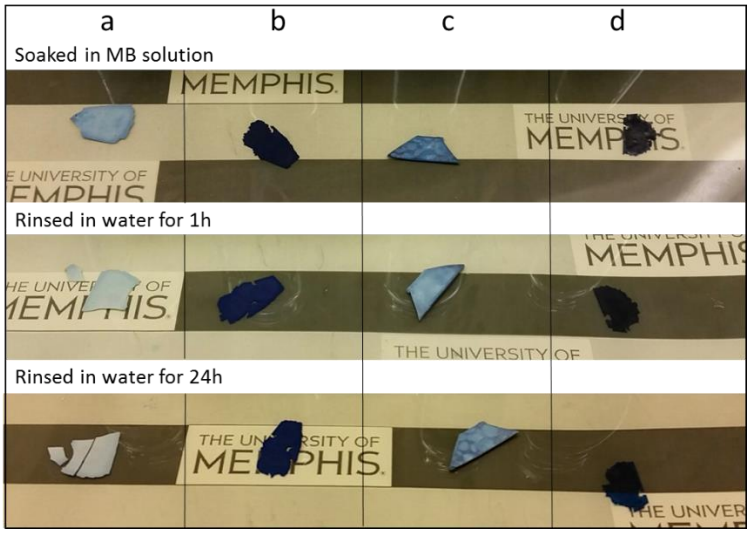

Figure 4-17 Porous membranes after immersed in 120 ppm Methylene Blue aqueous solution for 24 h with sonication (upper), rinsed and soaked in water for ^{1}H (middle), and further rinsed in water for 24h; a) Dual pore PSU membrane before PLA hydrolysis, b) Dual pore PSU membrane after PLA hydrolysis, c) PSU homopolymer microporous membrane, d) Nanoporous PSU membrane after PLA hydrolysis.

4.4. Conclusion

Nanoporous membranes (mesoporous) were prepared having different pore size and morphology and structure by controlling using a selective degradable component precursor block copolymer precursor s. For the first time, a controlled nanoporous structure was incorporated into a PSU membrane. Structure was confirmed through SAXS and SEM showing giving pore sizes between 50 and 23 nm. The volume of the degradable block was varied from 49 – 30% causing a change in pore size and morphology. When the degradable components volume percent was between 37 – 49% a lamellae morphology was confirmed by SAXS analysis. As the degradable component decreased to 30% a cylindrical morphology formed. Pore size was determined through SAXS and SEM giving pore sizes between 22 and 50 nm depending on the total degree of polymerization and volume fraction. Dual pore membranes were also demonstrated

here showing a combination of micro- and nano- size pores all in one PSU scaffold. Dye uptake studies showed the uptake of a cationic dye into the nanopores; the die was completely rinsed out of the micropores, but stayed in the nanopores. The tailor-made porous PSU membranes prepared by the unique methods are promising material as a PEM for VFRB and other applications.

4.5 Supplementary Information

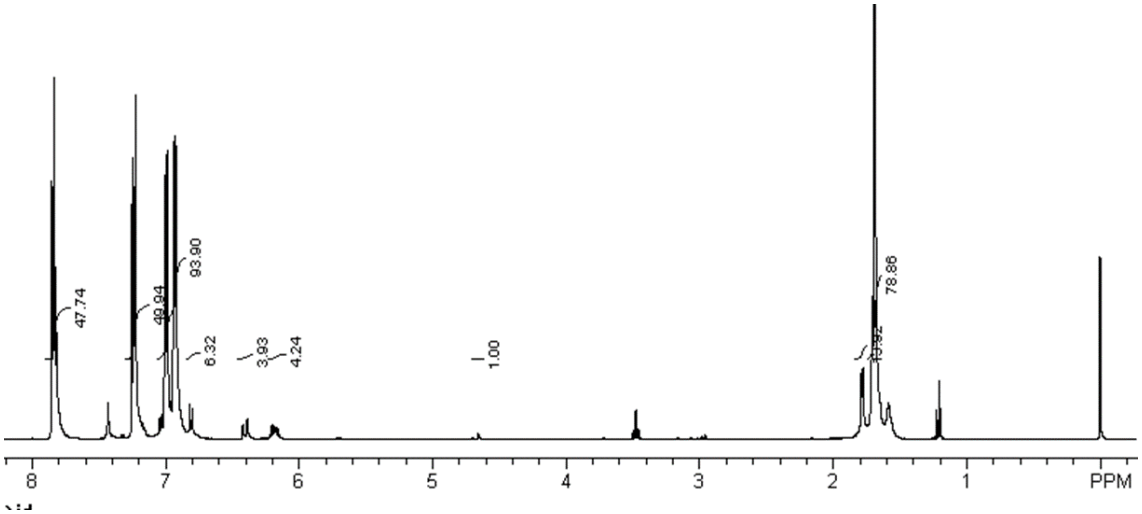

Figure 4-18 ^{1}H NMR of H-PSU-X20.

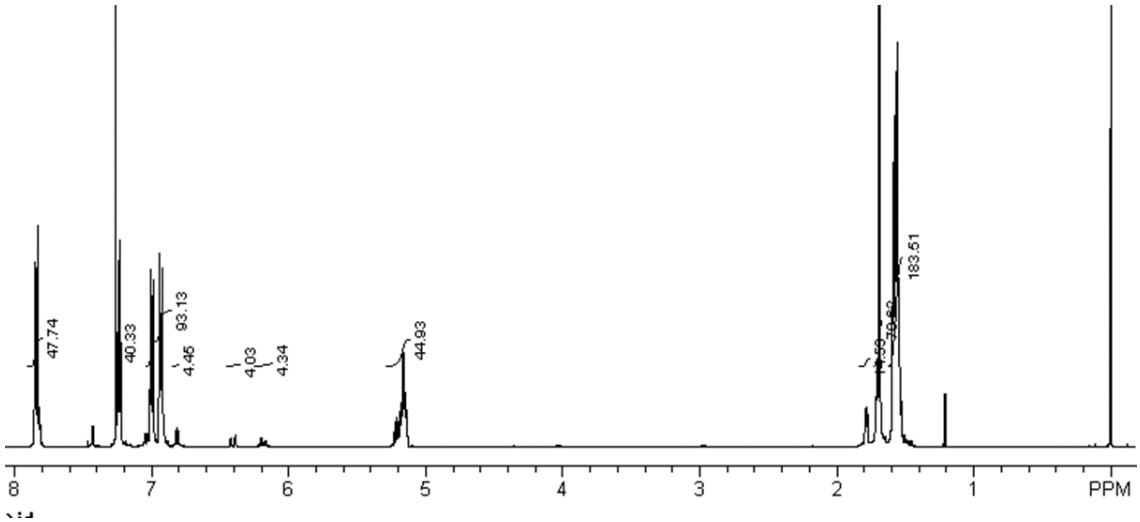

Figure 4-19 ^{1}H NMR of B-PPSU63.4-X20.

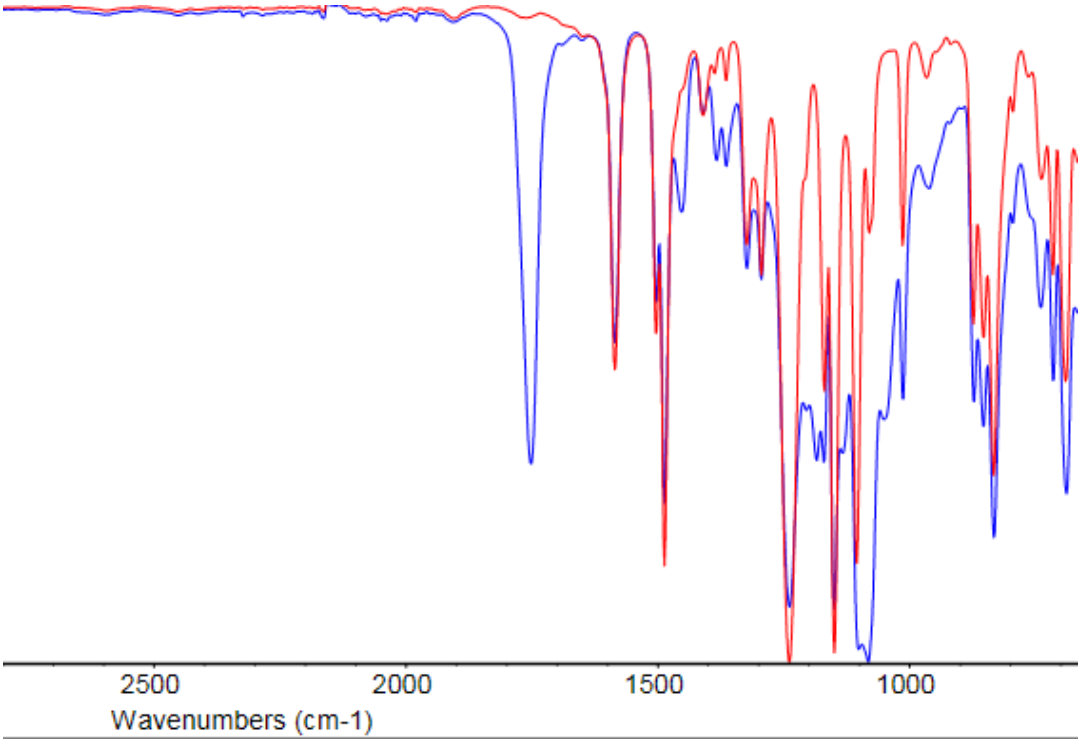

Figure 4-20 PPSU63.4-X20 membrane pre (blue) and post (red) hydrolysis, showing complete disappearance of PLA absorbance.

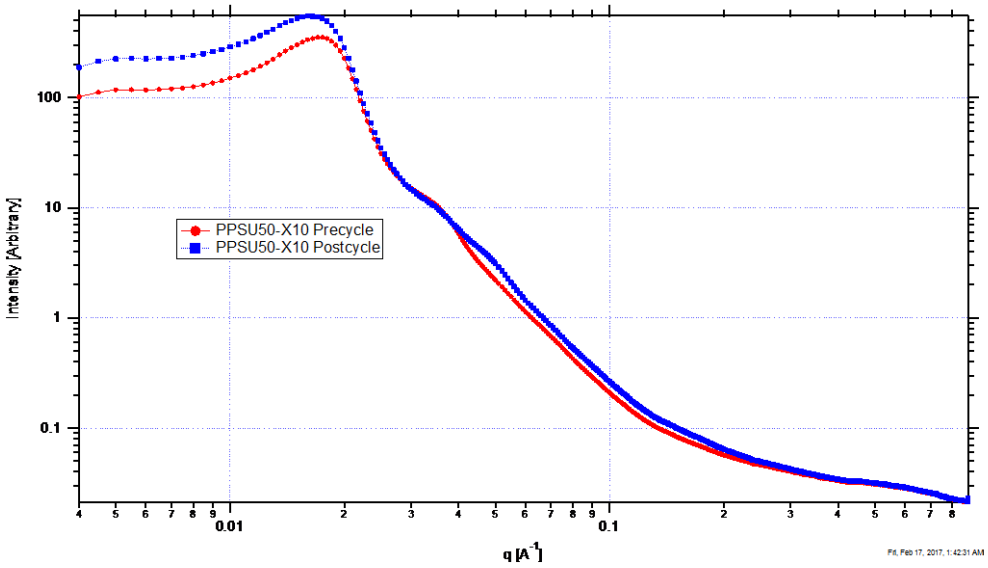

Figure 4-21 NP-PPSU50-X10 before and after 30 cycles in a VRFB, top) Postcycle membrane, bottom) Precycle membrane.

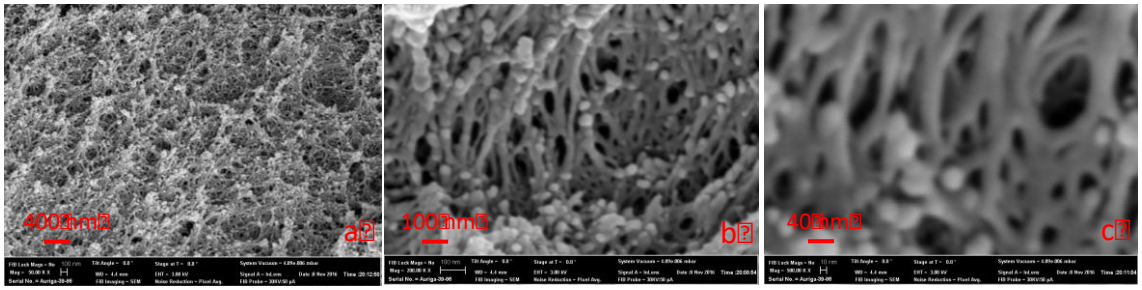

Figure 4-22 SEM images of NP-PPSU63-X20 gold coated cross section, at x50k, x100k, and x500k Mag.

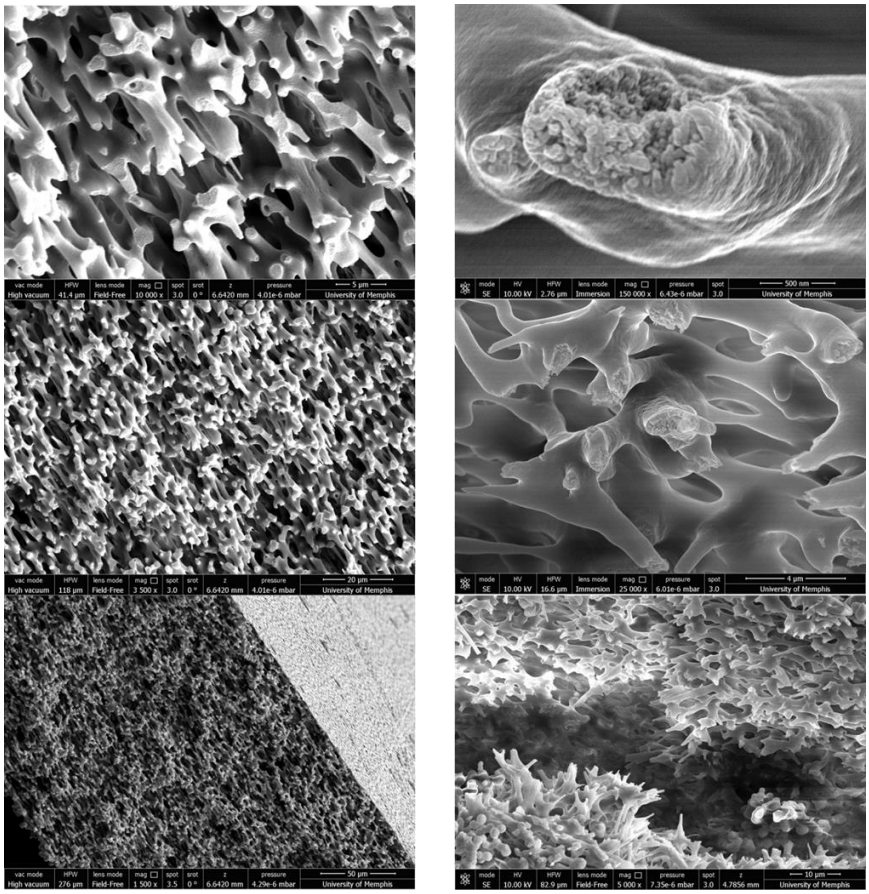

Figure 4-23 SEM images of dualpore PSU, DP2 (sample #26) of left) as cast membrane, right) post hydrolysis.

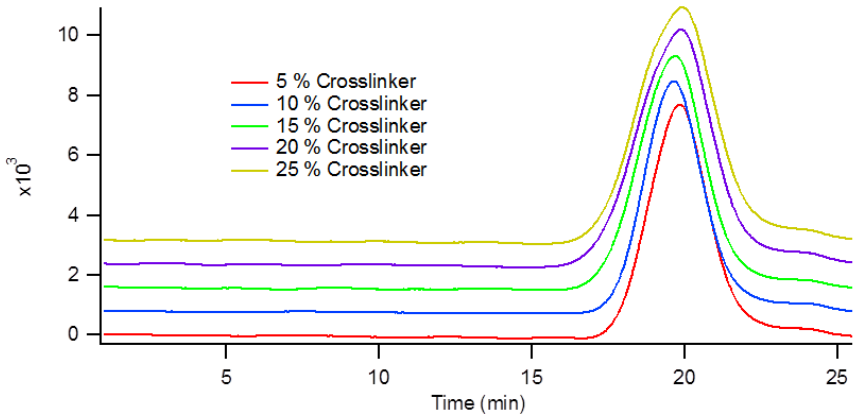

Figure 4-24 GPC chromatogram overlay of series 2 (crosslinking content) NP-PPSU. Listed from bottom to top: 1) B-PPSU49-x5, 2) B-PPSU51-x10, 3) B-PPSU55-x15, 4) B-PPSU51.5-X20, 5) B-PPSU48-X25.

Chapter 5

Pore surface and structural modification of nanoporous polysulfone

Controlled reactions that take place inside the pore of the aforementioned nanoporous PSU membranes will be invaluable in determining the structure-property relationships the pore chemistry, e.g. hydrophilicity and IEC, has on VRFBs. This chapter illustrates two methods to chemically functionalize the nanoporous PSU membranes covered in chapters 3 and 4. It is important to note that VRFBs possess highly acidic and oxidizing conditions which limit possible chemistries for pore/surface functionalization. These conditions eliminate the use of common chemical bonds such as esters and other pH sensitive bonds. The following pore modifications may not be viable for VRFB pore separators.

5.1 Photo-induced graft polymerization

5.1.1 Introduction

Photo-induced graft polymerization was used on commercially available nanofiltration (NF) membranes for improved filtration and durability.[159] Belfort *et al.* showed that commercially available PSU NF membranes can be directly functionalized by photo-induced graft polymerization that exploited the photoactive sulfone group on PSUs backbone.[160-166] UV induced homolytic cleavage of the sulfone group forms a reactive radical that initiates vinyl polymerization whilst degrading the polymer and is shown in Figure 5-1. Thus, the polymerization mechanism causes a tradeoff between the degree of grafting and the strength of the membrane.

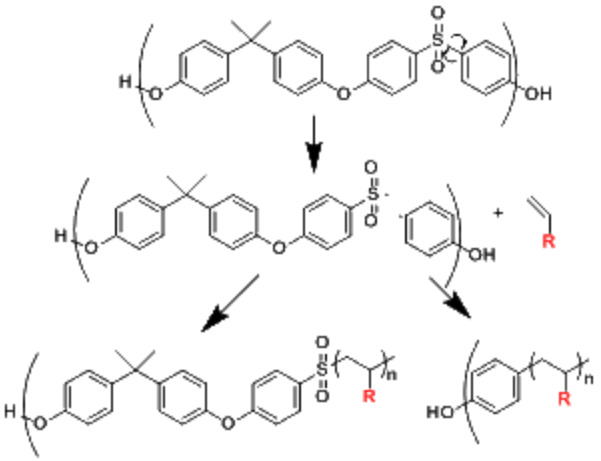

Figure 5-1 The proposed mechanism for the photochemical modification of PSU with vinyl monomers.

Chemically diverse vinyl monomers, e.g. 2-hydroxyethyl methacrylate (HEMA), glycidyl methacrylate (GMA), methacrylic acid (MAc) N-vinyl-2-pyrrolidinone (NVP), N-vinylformamide (NVF), and N-vinylcaprolactam (NVC) and others have been successfully grafted onto porous PSU membranes.[160,161,163] These modifications improved membrane properties, for example, increased hydrophilicity and selectivity and decreased fouling.

Photo-induced graft polymerization was used on NP-PPSU membranes (from chapters 3 and 4) to incorporate cationic and anionic exchange groups and is described here. Many vinyl reagents were screened and it was found that the highest grafting yield was obtained using styrenyl based reagents. The styrenyl monomers used were sodium 4-vinylbenzenesulfonate and (vinylbenzyl)trimethylammonium choloride shown in Figure 5-2.

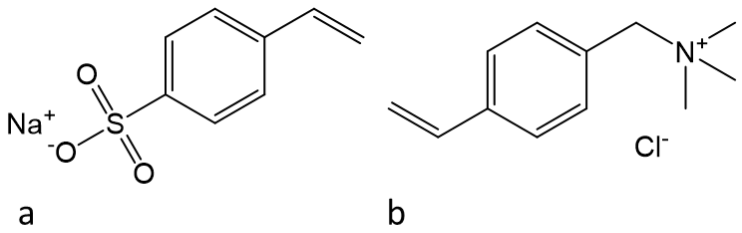

Figure 5-2 Chemical structures of photografted monomers, a) sodium 4-vinylbenzenesulfonate, b) (vinylbenzyl)trimethylammonium chloride

5.1.2 Membrane preparation

Nanoporous polysulfone membrane (NP-PPSU) were prepared using the same method described in chapter 3. Photo-induced graft polymerization was done on NP-PPSU52-X10 as follows: in a thin-walled glass beaker with a 5% aqueous monomer solution, a PSU membrane was charged and stirred for 4 h. Polymerization was initated by placing the solution roughly 6 in. from a 200 W unfiltered mercury arc lamp and irradiated for 60 minutes. After polymerization the membrane was rinsed with H_2O and soaked overnight to remove any residual monomer and homopolymer. Three different membranes were prepared: 1) PEM grafted PSU using sodium 4-vinylbenzenesulfonate, 2) AEM grafted PSU using (vinylbenzyl)trimethylammonium choloride, and 3) blank grafted PSU.

5.1.3 Results and Discussion:

Grafting was verified by FT-IR, contact angle, and titration. Titration of the grafted membranes showed comparable IECs of 0.10 to 0.14 for both strenyl monomers as shown in Table 5-1. Alternative sulfonated PEMs, such as the membranes in chapter 2, have much higher IECs around 1.5 or greater. Low IEC of sulfonated PEMs leads to low proton conductivity; however, this trend could be offset by more efficeint placement of ionic groups, e.g. exclusevely on the pore suface. This ultimately leads to enhanced

proton conductivity without the loss of physical and chemical strength as a result of high IEC.

Table 5-1 Photografted NP-PPSU52-X10

Membrane	**Water uptake%**	**Contact angle[a]**	**IEC via titration[b]**	**Density (dry)[c]**	**Density (wet)[c]**
PEM Graft	38.0 ± 3.8	56.6 ± 6.6	0.14 ± 0.09	0.725 ± 0.027	1.019 ± 0.063
AEM Graft	44.0 ± 2.9	68.9 ± 3.6	0.10 ± 0.06	0.680 ± 0.007	1.012 ± 0.002
H2O Blank	41.0 ± 1.3	74.1 ± 4.1	0	0.656 ± 0.004	0.945 ± 0.008
PPSU52-X10	43.4 ± 5.4	74.7 ±5.2	0	0.658 ± 0	1.013 ± 0

[a] Average of 9 measurements on each membrane
[b] IEC is given as mmol acid/gram of polymer
[c] Volume was calculated using l, w, and h measurements, given in g/cm^3

Contact angle is a great method to determine the change of a substrates surface chemistry and homogeneity. Contact angle decreased for both the AEM and PEM photo-grafted PSU membranes because the surface was more hydrophilic. Also, the blank grafted membrane had no change in contact angle. The water uptake did not change much due to the non-ionic hydrophobic polymer matrix that does not swell in water despite the presence of grafted hydrophilic ion exchange groups.

Grafted membranes were analyzed by ATR FT-IR as shown in Figure 5-3. Pre and post grafted PSU membranes showed nearly identical FT-IR spectrum as a result of the low grafting density which was not significant enough to give a noticeable band by FT-IR.

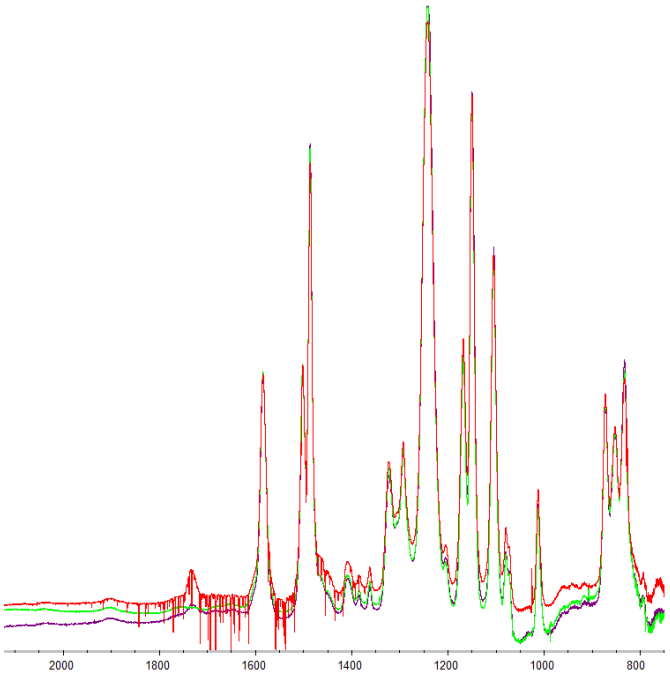

Figure 5-3 ATR FTIR spectrum of functional membranes: red) PEM modified, green) AEM modified, purple) unmodified porous membrane.

Table 5-2 shows *ex-situ* battery characterization of the membranes. Both photo-grafted samples had detectable conductivities in H_2O, but was much lower than Nafion and other sulfonated PEMs due to its lower IEC. The PEM grafted membrane showed higher proton conductivity than the AEM grafted membrane which was in agreement with the literature.

Permeability of VO^{2+} was measured for all membranes as shown in Table 5-2. Surprisingly, the unfunctionalized nanoporous membrane showed the lowest permeability whilst the photografted blank had over 4-times higher permeability. This was direct evidence that showed photografting has a negative effect on the membrane performance. The increased permeability of photografted samples could be from either an increased pore size or the formation of large defects. Compared to the blank grafted membrane, the PEM grafted membrane had increased vanadium crossover while the AEM grafted

membrane had lower crossover. Again, this trend is seen in VRFBs where anionic groups show higher VO^{2+} crossover compared to cationic groups due to the Donnan exclusion principle.

Table 5-2 Photografted membranes ex-situ analysis

Membrane	**Conductivity (mS/cm)[a]**	**Permeability (10^{-12} m^2/sec)[b]**
PEM Graft	2.10 ± 0.98	8.3875
AEM Graft	0.77 ± 0.39	4.5208
H2O Blank	0	7.2757
PPSU51.5-X10	0	1.7736

[a] Soaked in DI water overnight, removed from water and immediately analyzed

Conductivity was measured on all PSU membranes in sulfuric acid solutions with different concentrations shown in Figure 5-4. The unfunctionalized porous membrane had the highest conductivity with peak conductivity at 3 M H_2SO_4. At this concentration, the relative conductivity values for the non-treated membrane, PEM functionalized, and AEM functionalized were 1 : 0.5 : 0.25 respectively. These results agree with the decrease in conductivity seen in chapter 3 porous PSU membranes after acid functionalization via click reaction.

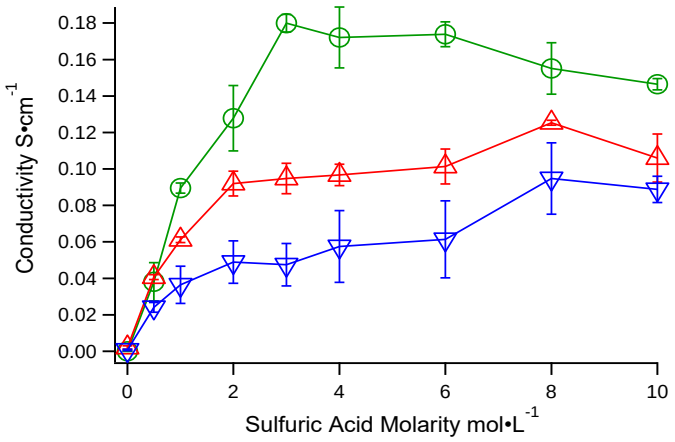

Figure 5-4 Conductivity of photografted membranes in different sulfuric acid molarities: (●) NP-PPSU-52-X10, (▲) PEM grafted NP-PPSU-52-X10, (▼) AEM grafted NP-PPSU-52-X10.

Membrane cycling was done under the same conditions given in chapter 3 for pre and post photo grafted membranes. The OCV decay in Figure 5-5 showed the porous PSU and PEM modified PSU were virtually overlapping up to 0.8 V meaning they have similar crossover. AEM grafted PSU showed much slower OCV decay because of its reduced crossover.

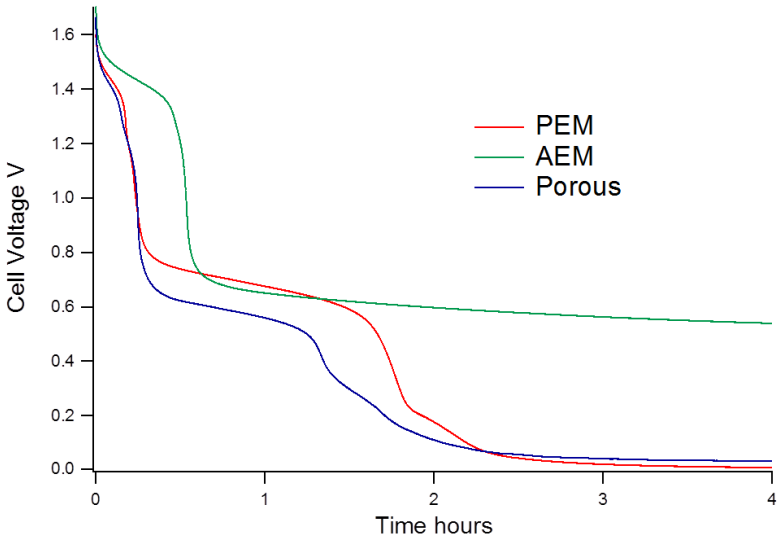

Figure 5-5 OCV decay of photografted membrane.

ASR of all membranes post- charge and discharge is shown in Figure 5-6. All porous membranes have a lower ASR than Nafion and are independent of the state of charge of the battery. The AEM grafted membrane showed a continuous decrease in ASR over the first 15 cycles which was likely due to slow sulfuric acid uptake into the membrane that required more cycles to equilibrate. Comparing the membrane ASRs to the conductivities, the PEM grafted membrane has a higher conductivity than AEM grafted membrane at 5 M H_2SO_4, but under battery conditions this trend is flipped. This changed resistance (or conductivity) for samples of the same thickness must be a direct effect from the vanadyl ion, specifically vanadyl ion interaction with the sulfonic acid moieties.

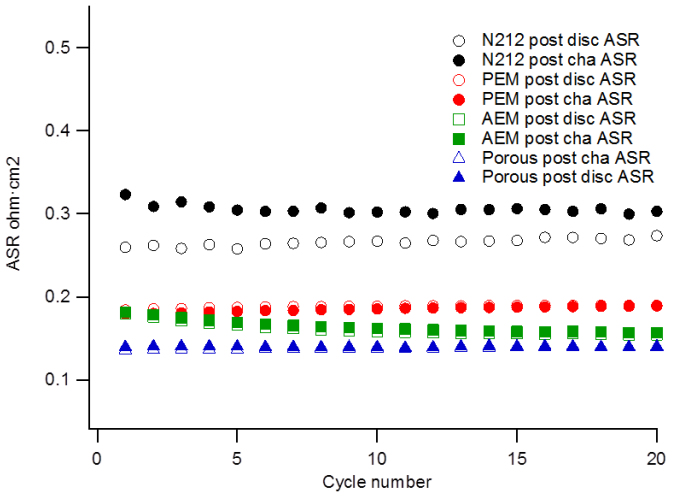

Figure 5-6 ASR of photografted membranes.

Cycling efficiencies are given in Figure 5-7. The AEM grafted membranes had the highest CE as a result of the Donnan exclusion principle preventing vanadium ion uptake. The PEM grafted membranes had a higher CE than the porous membrane due, but still lower than the AEM grafted membrane. The PEM grafted membrane showed lower VE

than the AEM modified membrane because of its higher ASR under cycling conditions. Overall the AEM grafted membrane shows the highest EE at high current density.

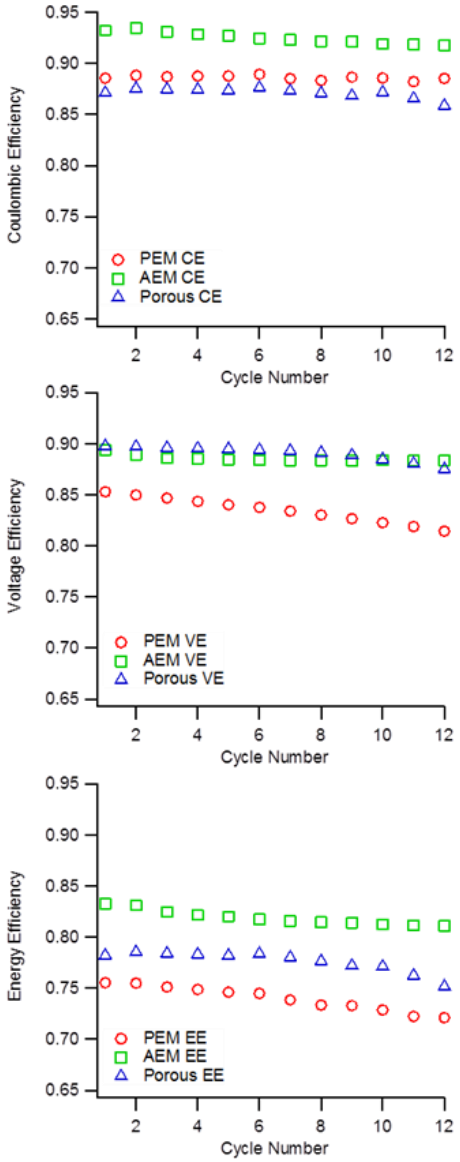

Figure 5-7 Cycling efficiencies of photografted membranes.

5.2 Silane grafting

5.2.1 Introduction and Overview

Silane coupling agents have been used since the 40s to functionalize substrate surfaces.[167-171] This method is a diverse platform used in many industries owing to its

ability to form durable bonds between organic and inorganic materials. Figure 5-8 illustrates the reaction mechanism of silane coupling on a generic substrate, coating it with a particular R group. First, alkoxy silyl bonds are hydrolyzed. During hydrolysis, these reagents condense to form oligomers and bind to the substrate surface. Lastly, a curing step (usually a thermal treatment) catalyzes a condensation reaction forming covalent bonds onto the substrate.

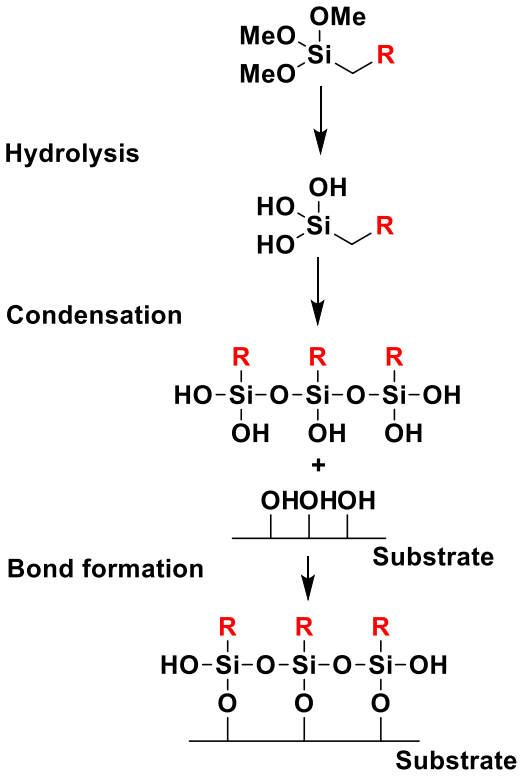

Figure 5-8 Deposition of silanes onto a hydroxyl coated substrate.[172]

5.2.2 Membrane Preparation

Nanoporous PSU membranes were prepared using the same procedure outlined in chapter 3. The nanoporous membranes were functionalized using trialkoxy silane reagents purchased from Gelest Inc. All membrane functionalization was done using same general procedure as follows: a 2% solution of a selected silane reagent in 95%

ethanol (or DI water if the silane reagent was insoluble in ethanol) was adjusted to a pH of ~5. The nanoporous membrane was added to the solution and stirred for 4 h. The membrane was rinsed quickly with ethanol, air dried, and placed in an oven at 110 °C for 12 h. After cooling to room temperature, the membrane was heated in 95% ethanol solution for 24 h with subsequent rinsing in H_2O.

Membranes were analyzed using the same instrumentation elaborated on in chapter 3. Also, elemental analysis was done using energy-dispersive X-ray spectroscopy (EDS) on a Nova NanoSEM 650 equipped with an Oxford EDS system with a 127 eV resolution detector. Samples were sputter coated with 3 nm palladium-gold prior to EDS analysis.

5.2.3 Results and Discussion

Eleven silane reagents with different functional groups (R groups in Table 5-3) were used for pore modification of porous PSU membranes. Table 5-3 shows the structure of the reagents selected which spans many different functional groups.

Limited chemical analyses could be used on the membranes since they were insoluble. FT-IR was used to qualitatively determine if the silane grafting was successful. For example, a porous PSU membrane functionalized with 3-aminopropyl silane showed the appearance of N-H stretching bands of a primary amine at 3370 and 3294 cm^{-1} seen in Figure 5-9. Membranes functionalized with O-(propargyl)-N-triethoxysilyl propyl carbamate showed a carbonyl stretching band at 1750 cm^{-1} and an alkyne C-H stretching band at 3300 cm^{-1} shown in Figure 5-10. However, the lack of strong stretching bands in FT-IR by most of the tested silane reagents makes qualitative determination difficult.

EDS gave quantitative information on the silane coating of the membranes whose results are summarized in Table 5-3. All reagents analyzed contained Si; however, EDS cannot establish the homogeneity of the silane functionalization. Table 5-4 shows EDS results of two reactions compared to an unfunctionalized nanoporous membrane. The photo grafted membranes have roughly two silane reagents (Si atoms) per available hydroxyl group based on estimations using the Si weight% and the known polymer molecular weight. Further studies are needed to determine how homogeneous the silane graft was in terms of depth.

Water uptake of the membranes was analyzed to discern how the modification changed the local pore properties. All modifications decreased water uptake were the extremely hydrophobic coating from TES-PF showed nearly no uptake at all.

Table 5-3 Summary of Silane modification reagents, conditions, and confirmation results

Silane Reagent Name	Silane ID	Silane Reagent Structure	Reaction Conditions	FT-IR	EDX	Water Uptake%
PPSU65-X25	n/a	n/a	n/a	n/a	n/a	6.9
N-phenyl aminopropyl trimethoxy silane	TMS-An	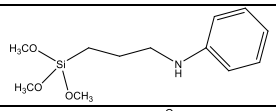	95% ethanol	No	n/a	n/a
Carboxyethylsilanetriol, disodium salt, 25% in water	THS-Ca	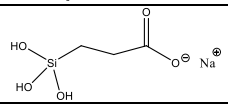	DI	No	n/a	n/a
(Heptadecafluoro-1,1,2,2-tetrahydrodecyl) triethoxy silane	TES-PF	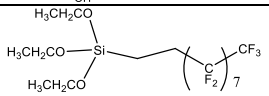	95% ethanol (pH4.5-5.5)	No	Yes	0.7
N-trimethoxysilyl propyl-N,N,N-trimethyl ammonium chloride	TMS-TMAC	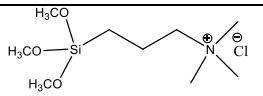	95% ethanol (pH4.5-5.5)	No	n/a	2.1
n-octyltriethoxy silane	TES-O	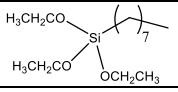	95% ethanol (pH4.5-5.5)	No	n/a	n/a
N-(2-aminoethyl)-3-aminopropyl silanetriol	THS-DAp	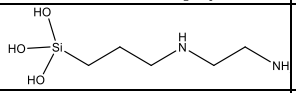	95% ethanol	No	n/a	n/a
3-(trihydroxysilyl)-1-propane sulfonic acid 30% in water.	THS-Sa	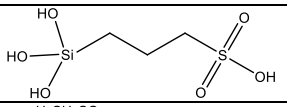	95% ethanol	No	n/a	2.9
3-aminopropyl triethoxy silane	TES-AP	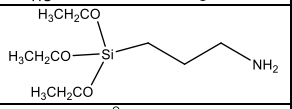	95% ethanol	Yes	Yes	3.5
O-(propargyl)-N-triethoxysilyl propyl carbamate.	TES-Ak	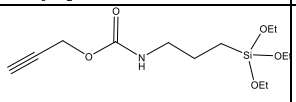	95% ethanol (pH4.5-5.5)	Yes	n/a	n/a
Trimethyl methoxy silane	MS-TM	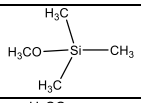	95% ethanol (pH4.5-5.5)	No	n/a	n/a
Trimethoxy methyl silane	TMS-M	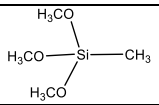	95% ethanol (pH4.5-5.5)	No	n/a	n/a

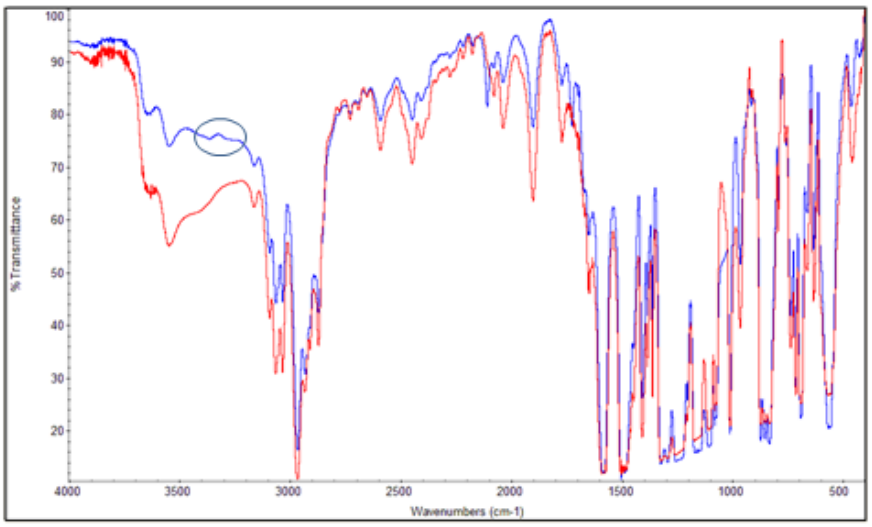

Figure 5-9 FT-IR of PPSU65-X25 (red) and TES-AP functionalized PPSU65-X25 (blue)

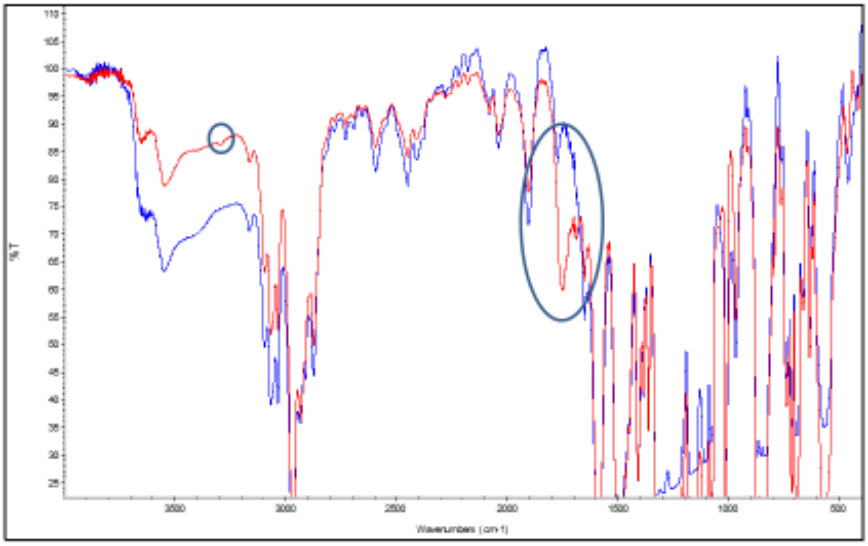

Figure 5-10 FT-IR of PPSU65-X25 (blue) and TES-Ak functionalized PPSU65-X25 (red)

Table 5-4 EDS results for selected silane modified membranes.

Membrane	**C Wt%**	**O Wt%**	**S Wt%**	**Si Wt%**	**F Wt%**	**N Wt%**
PPSU65-x25	78.9	13.95	7.15	N/D	N/D	N/D
PPSU65-x25 Fluoro (TES-PF)	78.27	12.48	7.08	0.65	1.52	N/D
PPSU65-x25 Amino (TES-AP)	78.09	13.99	7.20	0.72	N/D	N/D

5.3 Grafting conclusion

Photoinitiated graft polymerization was successfully employed using nanoporous PSU membranes and ionic vinyl monomers. The monomers selected had an anionic or cationic group that largely affected the photo grafted membrane properties and cycling efficiencies. The cationic groups showed the highest EE during cell cycling with a notably higher CE than the unfunctionalized membrane.

Separately, silane reagents were shown to effectively modify nanoporous PSU membranes. Based on EDS and water uptake analysis before and after grafting, the reaction was successful and changed the pore surface chemistry. For example, incorporating silane reagents with increased hydrophobicity gave reduced water uptake and an increased contact angle. Other reactions with alkyne containing silane reagents were successful and put forth a platform for easy surface click reactions. Further testing is needed to evaluate these membranes in a VRFB.

Chapter 6

Conclusion and outlook

The study described in this dissertation was aimed to explore the relationship of structure-property-performance of polymeric membranes for a VRFB application. Two different types of membranes were designed, synthesized, and fabricated to evaluate in VRFB systems: 1) sulfonated PEMs and 2) nanoporous membranes. All membranes prepared and studied are summarized in Table 6-1.

PEMs are commonly made from aromatic polymers such as PSU or PEEK that are sulfonated along the backbone. Improved self-assembly of the hydrophilic portion is possible by moving the sulfonic acid group away from the backbone using a flexible side chain. In this work, two sulfonated side chains were incorporated onto each PSU backbone using either an allyl sulfonate group (as-) or a strenyl sulfonate group (ss-) whose structures can be referred to in chapter 2. The side chain polymers were compared against PSU with sulfonic acid moieties along its backbone (sb-) using equivalent IECs between 1.45 and 1.72.

Both side chains improved self-assembly by developing phase separated domains of 3.9 and 5.2 nm in size for ss- and as- side chains, respectively. The ss- side chain had a smaller pore size from more complete separation of the hydrophilic channels. The water uptake of the membranes decreased with increased side chain length and hydrophobicity. For comparison, membranes with an IEC of 1.77 had water uptakes of 70, 62, and 50 for sb-, as-, and ss- respectively. This showed a large decrease of up to 30% by incorporating a side chain.

Battery cycling results on all membranes and the different side chains showed satisfactory efficiencies of regardless different IECs. However, the smaller pores of the ss- sample led to increased CE as well as the best EE. It should be noted that the change in efficiency is small but consistent for all IECs. The most interesting membrane was ss-PSU which showed ~30% less water uptake and increased EE and CE. Overall, our hypothesis, that is, improved channel formation can be controlled via polymer architecture and applied as a tool to enhance battery performance was successfully demonstrated.

The central focus of this dissertation is on nanoporous membranes fabricated from selectively degradable block copolymers as described in chapter 3-5. Tailored nanoporous membranes were prepared utilizing self-assembly of block copolymers. The crosslinkable PLA-PPSU-PLA triblock copolymers were synthesized with controlled block ratios. After membrane casting followed by *in* situ annealing and crosslinking based on thermal properties of polymers and reaction catalyst, The PLA block was thoroughly hydrolyzed under mild alkaline conditions.

Two series of membranes containing either different PPSU:PLA volume fractions or different crosslinking capacities were characterized. When the PPSU volume fraction increased from 50 to 70%, the membrane morphology shifted from lamellae to cylindrical nanostructures while pore domain sizes by SAXS analysis decreased from 31 to 22 nm, respectively. In the other series, crosslinking capacity on the PSU block was changed by varying the monomer ratio of 2,2'-diallyl BPA: BPA from 5 to 25%. SAXS analysis of nanoporous membranes showed the higher degree of crosslinking led to membranes with improved long-range order and a smaller pore size. The pore size

decreased from 34 to 29 nm as crosslinking capacity decreased. Preliminary cycling analysis on PPSU62 porous membrane was evaluated and gave a CE comparable to Nafion 212 at ~97%. Surprisingly, the large pores of over 20 nm were sufficient in minimizing crossover of vanadium.

Porous membranes were functionalized using different chemistries that highlighted their flexibility as a multi-functionable template. In one method, sulfonic acid moieties were covalently attached onto the pore surface by selective reactions from the hydroxyl group lined in the nanopores. Another method took advantage of the hydroxyl group lined pores by using silane coupling reagents to tailor the pore chemistry. Various types of functional alknoxy silane reagents were reacted on the surface by condensation to form siloxane layer with desired functionalities such as hydrophobic, hydrophilic, anionic, and cationic groups. Another method used was photo-initiated graft polymerization to incorporate vinyl ionic monomers onto the pores. Improved cell cycling efficiencies and conductivity, and ion selectivity were obtained depending on the monomer.

In summary, systematic studies of the tailor-made membranes in this research have generated some important outcomes in regard to relationship between their nanostructures and electrochemical properties. The performance of those membranes in VRFB has shown to be promising, and more detailed effects in efficiencies are interesting to investigate. Continuing studies will be carried out to take advantage of this tailored pore morphology, size, and chemistry using the previously outlined approach. All nanoporous and pore-modified membranes will be evaluated as a battery separator in VRFB. The results will be correlated to the membrane nanostructure and detailed

properties in order to further study the insight of ion transport mechanism and efficiency as our ultimate goal of this research.

Table 6-1 Summary of the major membranes synthesized and characterized

		Membrane Properties					Battery efficiency at 10 cycles			Structural Data		
Series	Membrane	IEC	Water uptake%	Conductivity in H_2O (mS cm^{-1})	Conductivity in electrolyte[a] (mS cm^{-1})	Conductivity in 3 M H_2SO_4 (mS cm^{-1})	VE%	CE%	EE%	Pore size (SAXS) (nm)	Pore size (SEM) (nm)	Morph-ology (SAXS)
Sulfonated Side chain PSU	sb-PSU-L	1.45	35	52	27	73	NA	NA	NA	NA	NA	NA
	sb-PSU-M	1.62	56	74	nd	NA	89	97	86	8.4	NA	NA
	sb-PSU-H	1.77	70	88	34	99	90	96	86	NA	NA	NA
	as-PSU-L	1.45	39	58	24	70	86	96	83	NA	NA	NA
	as-PSU-M	1.62	70	87	45	116	90	94	85	5.2	NA	NA
	as-PSU-H	1.77	62	83	nd	NA	87	93	82	NA	NA	NA
	ss-PSU-L	1.45	32	44	20	41	NA	NA	NA	NA	NA	NA
	ss-PSU-M	1.62	42	62	16	41	89	97	86	NA	NA	NA
	ss-PSU-H	1.77	50	73	26	71	89	97	86	3.9	NA	NA
Nanoporous Polysulfone	PPSU51-X20	0	NA[b]	0	NA	88	NA	NA	NA	30.7	20-30	LAM
	PPSU53-X20	0	37	0	NA	NA	NA	NA	NA	30.7	20-30	LAM
	PPSU61-X20	0	23	0	NA	39	NA	NA	NA	26.2	15-30	LAM
	PPSU63-X20	0	25	0	NA	72	NA	NA	NA	24.6	15-30	LAM
	PPSU70-X20	0	nd	0	NA	NA	NA	NA	NA	22.4	15-30	CYL
	PPSU49-x5	0	NA	0	NA	NA	NA	NA	NA	34.0	NA	LAM
	PPSU51-x10	0	NA	0	NA	175	88	87	77	33.1	NA	LAM
	PPSU55-x15	0	NA	0	NA	NA	NA	NA	NA	34.0	NA	LAM
	PPSU48-X25	0	NA	0	NA	NA	NA	NA	NA	28.6	NA	LAM
	Styrene sulfonate graft on PPSU51-x10	0.14 ± 0.09	28	2.1	NA	95	83	89	73	33	NA	LAM
	Quaternized graft on PPSU51-x10	0.10 ± 0.06	44	0.8	NA	42	88	92	82	33	NA	LAM
Dual pore Membranes	DP1 from PPSU63-X20	0	NA	0	NA	NA	NA	NA	NA	22.8	2-4 µM + 25-50 nm	LAM
	DP2 from PPSU63-X20	0	NA	0	NA	NA	NA	NA	NA	22.8	2-4 µM + 25-50 nm	LAM
Reference	Nafion 212	0.91	28	105	34	NA	88	96	85	NA	NA	NA

[a] 1.7 M $VOSO_4$ + 3.3 M H_2SO_4

[b] NA: no measurement was don

REFERENCES

(1) United States. Office of Energy Markets and End Use.; Energy Information Administration, Office of Energy Markets and End Use: Washington, D.C., p volumes.

(2) Council, N. R. The National Academies Summit on Americas Energy Future: Summary of a Meeting; The National Academies Press: Washington, DC, 2008.

(3) Weber, A. Z.; Mench, M. M.; Meyers, J. P.; Ross, P. N.; Gostick, J. T.; Liu, Q. H. J Appl Electrochem 2011, 41, 1137.

(4) Kear, G.; Shah, A. A.; Walsh, F. C. International Journal of Energy Research 2012, 36, 1105.

(5) EPRI, U. S. D. o. E. EPRI 2003.

(6) Dunn, B.; Kamath, H.; Tarascon, J.-M. Science 2011, 334, 928.

(7) Sawabe, M.; Tanaka, N.; Mieno, M. N.; Ishikawa, S.; Kayaba, K.; Nakahara, K.; Matsushita, S.; Grp, J. M. S. C. S. Plos One 2012, 7.

(8)nPrifti, H.; Parasuraman, A.; Winardi, S.; Lim, T. M.; Skyllas-Kazacos, M. Membranes 2012, 2, 275.

(9) Schwenzer, B.; Zhang, J. L.; Kim, S.; Li, L. Y.; Liu, J.; Yang, Z. G. ChemSusChem 2011, 4, 1388.

(10) Doan, T. N. L.; Hoang, T. K. A.; Chen, P. RSC Adv. 2015, 5, 72805.

(11) Gierke, T. D.; Munn, G. E.; Wilson, F. C. J Polym Sci Pol Phys 1981, 19, 1687.

(12) Hickner, M. A.; Pivovar, B. S. Fuel Cells 2005, 5, 213.

(13) Paddison, S. J. Annual Review of Materials Research 2003, 33, 289.

(14) Gebel, G.; Lambard, J. Macromolecules 1997, 30, 7914.

(15) James, P. J.; Elliott, J. A.; McMaster, T. J.; Newton, J. M.; Elliott, A. M. S.; Hanna, S.; Miles, M. J. J. Mater. Sci. 2000, 35, 5111.

(16) Elliott, J. A.; Paddison, S. J. Phys. Chem. Chem. Phys. 2007, 9, 2602.

(17) Zawodzinski, T. A.; Derouin, C.; Radzinski, S.; Sherman, R. J.; Smith, V. T.; Springer, T. E.; Gottesfeld, S. J Electrochem Soc 1993, 140, 1041.

(18) Zawodzinski, T. A.; Neeman, M.; Sillerud, L. O.; Gottesfeld, S. J Phys Chem-Us 1991, 95, 6040.

(19) Zawodzinski, T. A.; Springer, T. E.; Davey, J.; Jestel, R.; Lopez, C.; Valerio, J.; Gottesfeld, S. J Electrochem Soc 1993, 140, 1981.

(20) Kalapos, T. L.; Decker, B.; Every, H. A.; Ghassemi, H.; Zawodzinski, T. A. J Power Sources 2007, 172, 14.

(21) Springer, T. E.; Zawodzinski, T. A.; Gottesfeld, S. J Electrochem Soc 1991, 138, 2334.

(22) Wang, F.; Hickner, M.; Ji, Q.; Harrison, W.; Mecham, J.; Zawodzinski, T. A.; McGrath, J. E. Macromol Symp 2001, 175, 387.

(23) Wang, F.; Hickner, M.; Kim, Y. S.; Zawodzinski, T. A.; McGrath, J. E. J Membrane Sci 2002, 197, 231.

(24) Kreuer, K. D. Chemistry of Materials 1996, 8, 610.

(25) Kreuer, K. D. J Membrane Sci 2001, 185, 29.

(26) Ghassemi, H.; McGrath, J. E.; Zawodzinski, T. A. Polymer 2006, 47, 4132.

(27) Peckham, T. J.; Holdcroft, S. Adv. Mater. 2010, 22, 4667.

(28) Ghassemi, H.; Harrison, W.; Zawodzinski, T.; McGrath, J. E. Abstr Pap Am Chem S 2004, 227, U428.

(29) Lee, H. S.; Roy, A.; Badami, A. S.; McGrath, J. E. Macromol Res 2007, 15, 160.

(30) Lee, M.; Park, J. K.; Lee, H. S.; Lane, O.; Moore, R. B.; McGrath, J. E.; Baird, D. G. Polymer 2009, 50, 6129.

(31) Roy, A.; Yu, X.; Dunn, S.; McGrath, J. E. J Membrane Sci 2009, 327, 118.

(32) Wang, F.; Kim, Y. S.; Hickner, M. A.; Zawodzinski, T. A.; McGrath, J. E. Abstr Pap Am Chem S 2001, 222, U387.

(33) Chen, Y.; Rowlett, J. R.; Lee, C. H.; Lane, O. R.; VanHouten, D. J.; Zhang, M.; Moore, R. B.; McGrath, J. E. Journal of Polymer Science Part A: Polymer Chemistry 2013, 51, 2301.

(34) Mcgrath, J. In Advances in Materials for Proton Exchange Membrane Fuel Cell Systems Asilomar, Ca, 2013.

(35) Hickner, M. A.; Ghassemi, H.; Kim, Y. S.; Einsla, B. R.; McGrath, J. E. Chemical Reviews 2004, 104, 4587.

(36) Hickner, M. A.; Wang, F.; Kim, Y. S.; Privovar, B.; Zawodzinski, T. A.; McGrath, J. E. Abstr Pap Am Chem S 2001, 222, U467.

(37) Lee, H. S.; Roy, A.; Lane, O.; Dunn, S.; McGrath, J. E. Polymer 2008, 49, 715.

(38) Badami, A. S.; Lee, H. S.; Li, Y. X.; Roy, A.; Wang, H.; McGrath, J. E. Acs Sym Ser 2010, 1040, 65.

(39) Ghassemi, H.; Zawodzinski, T. Abstr Pap Am Chem S 2005, 230, U1649.

(40) Bae, B.; Miyatake, K.; Watanabe, M. Macromolecules 2010, 43, 2684.

(41) Varcoe, J. R.; Atanassov, P.; Dekel, D. R.; Herring, A. M.; Hickner, M. A.; Kohl, P. A.; Kucernak, A. R.; Mustain, W. E.; Nijmeijer, K.; Scott, K.; Xu, T. W.; Zhuang, L. Energy Environ. Sci. 2014, 7, 3135.

(42) Maurya, S.; Shin, S. H.; Kim, Y.; Moon, S. H. RSC Adv. 2015, 5, 37206.

(43) Mohammadi, T.; Skyllas-Kazacos, M. J Membrane Sci 1995, 107, 35.

(44) Chieng, S. C.; Kazacos, M.; Skyllas-Kazacos, M. J Power Sources 1992, 39, 11.

(45) Mohammadi, T.; Skyllas-Kazacos, M. J Membrane Sci 1995, 98, 77.

(46) Zhou, X. L.; Zhao, T. S.; An, L.; Wei, L.; Zhang, C. Electrochim Acta 2015, 153, 492.

(47) Maurya, S.; Shin, S. H.; Lee, J. Y.; Kim, Y.; Moon, S. H. RSC Adv. 2016, 6, 5198.

(48) Luo, T.; David, O.; Gendel, Y.; Wessling, M. J Power Sources 2016, 312, 45.

(49) Yuan, Z. Z.; Duan, Y. Q.; Zhang, H. Z.; Li, X. F.; Zhang, H. M.; Vankelecom, I. Energy Environ. Sci. 2016, 9, 441.

(50) Peng, S.; Yan, X.; Wu, X.; Zhang, D.; Luo, Y.; Su, L.; He, G. RSC Adv. 2017, 7, 1852.

(51) Xu, W. X.; Li, X. F.; Cao, J. Y.; Zhang, H. Z.; Zhang, H. M. Sci Rep-Uk 2014, 4.

(52) Zhao, Y.; Yuan, Z.; Lu, W.; Li, X.; Zhang, H. J Power Sources 2017, 342, 327.

(53) Yuan, Z. Z.; Dai, Q.; Zhao, Y. Y.; Lu, W. J.; Li, X. F.; Zhang, H. M. J. Mater. Chem. A 2016, 4, 12955.

(54) Chen, D. J.; Li, D. D.; Li, X. F. RSC Adv. 2016, 6, 87104.

(55) Chae, I.; Luo, T.; Moon, G. H.; Ogieglo, W.; Kang, Y. S.; Wessling, M. Advanced Energy Materials 2016, 6.

(56) Zhang, H. Z.; Zhang, H. M.; Li, X. F.; Mai, Z. S.; Zhang, J. L. Energy Environ. Sci. 2011, 4, 1676.

(57) Wu, C. X.; Lu, S. F.; Wang, H. N.; Xu, X.; Peng, S. K.; Tan, Q. L.; Xiang, Y. J. Mater. Chem. A 2016, 4, 1174.

(58) Wei, W. P.; Zhang, H. M.; Li, X. F.; Zhang, H. Z.; Li, Y.; Vankelecom, I. Phys. Chem. Chem. Phys. 2013, 15, 1766.

(59) Zhang, D. S.; Yan, X. M.; He, G. H.; Zhang, L.; Liu, X. H.; Zhang, F. X.; Hu, M. M.; Dai, Y.; Peng, S. S. J. Mater. Chem. A 2015, 3, 16948.

(60) Inform 1990, 4, 26.

(61) Inagaki, M.; Yamada, M.; Yonemoto, N.; Takahashi, K.; Grp, J.-M. Eur Psychiat 2012, 27.

(62) Nakagawara, J.; Minematsu, K.; Okada, Y.; Tanahashi, N.; Nagahiro, S.; Mori, E.; Shinohara, Y.; Yamaguchi, T.; Investigators, J.-M. Stroke 2010, 41, 1984.

(63) Mohammadi, T.; Skyllas-Kazacos, M. J Power Sources 1995, 56, 91.

(64) Tian, B.; Yan, C. W.; Wang, F. H. J Membrane Sci 2004, 234, 51.

(65) Zhou, X. L.; Zhao, T. S.; An, L.; Zeng, Y. K.; Wei, L. J Power Sources 2016, 327, 67.

(66) Zhang, H. W.; Shen, P. K. Chemical Reviews 2012, 112, 2780.

(67) Brandrup. J., I., E.H., Grulke, E.A. Polymer Handbook; 4th ed.; John Wiley: New York, 1999.

(68) Asensio, J. A.; Sanchez, E. M.; Gomez-Romero, P. Chemical Society Reviews 2010, 39, 3210.

(69) Yuan, Z.; Duan, Y.; Zhang, H.; Li, X.; Zhang, H.; Vankelecom, I. Energy Environ. Sci. 2015.

(70) Li, X. F.; De Feyter, S.; Vankelecom, I. F. J. J Membrane Sci 2008, 324, 67.

(71) Zhang, H. Z.; Ding, C.; Cao, J. Y.; Xu, W. X.; Li, X. F.; Zhang, H. M. J. Mater. Chem. A 2014, 2, 9524.

(72) Lu, W. J.; Yuan, Z. Z.; Zhao, Y. Y.; Li, X. F.; Zhang, H. M.; Vankelecom, I. F. J. Energy Environ. Sci. 2016, 9, 2319.

(73) Darling, S. B. Progress in Polymer Science 2007, 32, 1152.

(74) Hamley, I. W. The physics of block copolymers; Oxford University Press: Oxford ; New York, 1998.

(75) Bates, F. S.; Fredrickson, G. H. Physics Today 1999, 52, 32.

(76) Mai, Y.; Eisenberg, A. Chemical Society Reviews 2012, 41, 5969.

(77) Lee, J. S.; Hirao, A.; Nakahama, S. Macromolecules 1988, 21, 274.

(78) Hillmyer, M. A. In Block Copolymers Ii; Abetz, V., Ed. 2005; Vol. 190, p 137.

(79) Liu, G. J. Curr. Opin. Colloid Interface Sci. 1998, 3, 200.

(80) Olson, D. A.; Chen, L.; Hillmyer, M. A. Chemistry of Materials 2008, 20, 869.

(81) Jackson, E. A.; Hillmyer, M. A. Acs Nano 2010, 4, 3548.

(82) Zalusky, A. S.; Olayo-Valles, R.; Wolf, J. H.; Hillmyer, M. A. J Am Chem Soc 2002, 124, 12761.

(83) Zalusky, A. S.; Olayo-Valles, R.; Taylor, C. J.; Hillmyer, M. A. J Am Chem Soc 2001, 123, 1519.

(84) Vayer, M.; Hillmyer, M. A.; Dirany, M.; Thevenin, G.; Erre, R.; Sinturel, C. Thin Solid Films 2010, 518, 3710.

(85) Kubo, T.; Wang, R. F.; Olson, D. A.; Rodwogin, M.; Hillmyer, M. A.; Leighton, C. Applied Physics Letters 2008, 93, 133112.

(86) Saba, S. A.; Mousavi, M. P. S.; Buhlmann, P.; Hillmyer, M. A. J Am Chem Soc 2015, 137, 8896.

(87) Rodwogin, M. D.; Spanjers, C. S.; Leighton, C.; Hillmyer, M. A. Acs Nano 2010, 4, 725.

(88) Pitet, L. M.; van Loon, A. H. M.; Kramer, E. J.; Hawker, C. J.; Meijer, E. W. Acs Macro Letters 2013, 2, 1006.

(89) Nagarajan, S.; Gowd, E. B. Macromolecules 2015, 48, 5367.

(90) Wolf, J. H.; Hillmyer, M. A. Langmuir 2003, 19, 6553.

(91) Mao, H. M.; Arrechea, P. L.; Bailey, T. S.; Johnson, B. J. S.; Hillmyer, M. A. Faraday Discussions 2005, 128, 149.

(92) Olayo-Valles, R.; Guo, S. W.; Lund, M. S.; Leighton, C.; Hillmyer, M. A. Macromolecules 2005, 38, 10101.

(93) Rzayev, J.; Hillmyer, M. A. J Am Chem Soc 2005, 127, 13373.

(94) Bailey, T. S.; Rzayev, J.; Hillmyer, M. A. Macromolecules 2006, 39, 8772.

(95) Mao, H. M.; Hillmyer, M. A. Soft Matter 2006, 2, 57.

(96) Phillip, W. A.; Rzayev, J.; Hillmyer, M. A.; Cussler, E. L. J Membrane Sci 2006, 286, 144.

(97) Cavicchi, K. A.; Russell, T. P. Macromolecules 2007, 40, 1181.

(98) Chen, L.; Phillip, W. A.; Cussler, E. L.; Hillmyer, M. A. J Am Chem Soc 2007, 129, 13786.

(99) Chen, L.; Hillmyer, M. A. Macromolecules 2009, 42, 4237.

(100) Crossland, E. J. W.; Ludwigs, S.; Hillmyer, M. A.; Steiner, U. Soft Matter 2007, 3, 94.

(101) Boudouris, B. W.; Frisbie, C. D.; Hillmyer, M. A. Macromolecules 2008, 41, 67.

(102) Phillip, W. A.; O'Neill, B.; Rodwogin, M.; Hillmyer, M. A.; Cussler, E. L. Acs Applied Materials & Interfaces 2010, 2, 847.

(103) Pitet, L. M.; Amendt, M. A.; Hillmyer, M. A. J Am Chem Soc 2010, 132, 8230.

(104) Bolton, J.; Bailey, T. S.; Rzayev, J. Nano Letters 2011, 11, 998.

(105) Majdoub, R.; Antoun, T.; Le Droumaguet, B.; Benzina, M.; Grande, D. Reactive & Functional Polymers 2012, 72, 495.

(106) Song, J.; Cho, B.-K. Acs Macro Letters 2012, 1, 1375.

(107) Jackson, E. A.; Lee, Y.; Hillmyer, M. A. Macromolecules 2013, 46, 1484.

(108) Kim, S.; Tighe, T. B.; Schwenzer, B.; Yan, J.; Zhang, J.; Liu, J.; Yang, Z.; Hickner, M. A. J Appl Electrochem 2011, 41, 1201.

(109) Jutemar, E. P.; Jannasch, P. J Membrane Sci 2010, 351, 87.

(110) Parasuraman, A.; Lim, T. M.; Menictas, C.; Skyllas-Kazacos, M. Electrochim Acta 2013, 101, 27.

(111) Sun, C. N.; Tang, Z. J.; Belcher, C.; Zawodzinski, T. A.; Fujimoto, C. Electrochemistry Communications 2014, 43, 63.

(112) Tang, Z. J.; Lawton, J. S.; Sun, C. N.; Chen, J. H.; Bright, M. I.; Jones, A. M.; Papandrew, A. B.; Fujimoto, C. H.; Zawodzinski, T. A. J Electrochem Soc 2014, 161, A1860.

(113) Aaron, D. S.; Liu, Q.; Tang, Z.; Grim, G. M.; Papandrew, A. B.; Turhan, A.; Zawodzinski, T. A.; Mench, M. M. J Power Sources 2012, 206, 450.

(114) Lawton, J. S.; Aaron, D. S.; Tang, Z. J.; Zawodzinski, T. A. J Membrane Sci 2013, 428, 38.

(115) Lawton, J. S.; Jones, A.; Zawodzinski, T. J Electrochem Soc 2013, 160, A697.

(116) Tang, Z.; Keith, R. E.; Aaron, D. S.; Lawton, J. S.; Papandrew, A. B.; Zawodzinski, T. A. In Large Scale Energy Storage for Smart Grid Applications; Savinell, R., Meyers, J., Narayan, S. R., Wheeler, D., Eds.; Electrochemical Soc Inc: Pennington, 2012; Vol. 41, p 25.

(117) Ghosh, A.; Banerjee, S. e-Polymers 2014, 14.

(118) Park, C. H.; Lee, C. H.; Guiver, M. D.; Lee, Y. M. Progress in Polymer Science 2011, 36, 1443.

(119) Li, N. W.; Guiver, M. D. Macromolecules 2014, 47, 2175.

(120) Li, Y.; Xie, M.; Wang, X. T.; Chao, D. M.; Liu, X. C.; Wang, C. Int J Hydrogen Energ 2013, 38, 12051.

(121) Kerres, J. A. Polym Rev 2015, 55, 273.

(122) Li, N. W.; Hwang, D. S.; Lee, S. Y.; Liu, Y. L.; Lee, Y. M.; Guiver, M. D. Macromolecules 2011, 44, 4901.

(123) Matsumoto, K.; Higashihara, T.; Ueda, M. Macromolecules 2009, 42, 1161.

(124) Pang, J. H.; Jin, X.; Wang, Y.; Feng, S. N.; Shen, K. Z.; Wang, G. B. J Membrane Sci 2015, 492, 67.

(125) Zhang, X.; Sheng, L.; Hayakawa, T.; Ueda, M.; Higashihara, T. J. Mater. Chem. A 2013, 1, 11389.

(126) Li, N. W.; Shin, D. W.; Hwang, D. S.; Lee, Y. M.; Guiver, M. D. Macromolecules 2010, 43, 9810.

(127) Wang, C.; Shin, D. W.; Lee, S. Y.; Kang, N. R.; Lee, Y. M.; Guiver, M. D. J Membrane Sci 2012, 405, 68.

(128) Kern, K. E.; Abdellatif, M.; Fossum, E. Polym. Int. 2012, 61, 1249.

(129) Sankir, M.; Bhanu, V. A.; Harrison, W. L.; Ghassemi, H.; Wiles, K. B.; Glass, T. E.; Brink, A. E.; Brink, M. H.; McGrath, J. E. J Appl Polym Sci 2006, 100, 4595.

(130) Springer, T. E.; Zawodzinski, T. A.; Wilson, M. S.; Gottesfeld, S. J Electrochem Soc 1996, 143, 587.

(131) Tang, Z. J.; Svoboda, R.; Lawton, J. S.; Aaron, D. S.; Papandrew, A. B.; Zawodzinski, T. A. J Electrochem Soc 2013, 160, F1040.

(132) Alotto, P.; Guarnieri, M.; Moro, F. Renewable and Sustainable Energy Reviews 2014, 29, 325.

(133) Viswanathan, V.; Crawford, A.; Stephenson, D.; Kim, S.; Wang, W.; Li, B.; Coffey, G.; Thomsen, E.; Graff, G.; Balducci, P.; Kintner-Meyer, M.; Sprenkle, V. J Power Sources 2014, 247, 1040.

(134) Li, X. F.; Zhang, H. M.; Mai, Z. S.; Zhang, H. Z.; Vankelecom, I. Energy Environ. Sci. 2011, 4, 1147.

(135) Moore, M.; Watson, J. S.; Zawodzinski, T. A.; Zhang, M. Q.; Counce, R. M. Ecs Transactions 2012, 41, 1.

(136) Hashimoto, T.; Tsutsumi, K.; Funaki, Y. Langmuir 1997, 13, 6869.

(137) Thurn-Albrecht, T.; Steiner, R.; DeRouchey, J.; Stafford, C. M.; Huang, E.; Bal, M.; Tuominen, M.; Hawker, C. J.; Russell, T. Adv. Mater. 2000, 12, 787.

(138) Chan, V. Z. H.; Hoffman, J.; Lee, V. Y.; Iatrou, H.; Avgeropoulos, A.; Hadjichristidis, N.; Miller, R. D.; Thomas, E. L. Science 1999, 286, 1716.

(139) Lee, J. S.; Hirao, A.; Nakahama, S. Macromolecules 1988, 21, 274.

(140) Liu, G. J.; Ding, J. F.; Guo, A.; Herfort, M.; BazettJones, D. Macromolecules 1997, 30, 1851.

(141) Avgeropoulos, A.; Chan, V. Z. H.; Lee, V. Y.; Ngo, D.; Miller, R. D.; Hadjichristidis, N.; Thomas, E. L. Chemistry of Materials 1998, 10, 2109.

(142) Viswanathan, R.; Johnson, B. C.; McGrath, J. E. Polymer 1984, 25, 1827.

(143) Lohmeijer, B. G. G.; Pratt, R. C.; Leibfarth, F.; Logan, J. W.; Long, D. A.; Dove, A. P.; Nederberg, F.; Choi, J.; Wade, C.; Waymouth, R. M.; Hedrick, J. L. Macromolecules 2006, 39, 8574.

(144) Aaron, D.; Tang, Z. J.; Papandrew, A. B.; Zawodzinski, T. A. J Appl Electrochem 2011, 41, 1175.

(145) Suarez, S. N.; Jayakody, J. R. P.; Greenbaum, S. G.; Zawodzinski, T.; Fontanella, J. J. J Phys Chem B 2010, 114, 8941.

(146) Pourcelly, G.; Lindheimer, A.; Gavach, C.; Hurwitz, H. D. J Electroanal Chem 1991, 305, 97.

(147) Pourcelly, G.; Lindheimer, A.; Pamboutzoglou, G.; Gavach, C. J Electroanal Chem 1989, 259, 113.

(148) Verbrugge, M. W.; Hill, R. F. J Phys Chem-Us 1988, 92, 6778.

(149) Skyllas-Kazacos, M.; Kazacos, M. J Power Sources 2011, 196, 8822.

(150) Minke, C.; Turek, T. J Power Sources 2015, 286, 247.

(151) Ulaganathan, M.; Aravindan, V.; Yan, Q. Y.; Madhavi, S.; Skyllas-Kazacos, M.; Lim, T. M. Advanced Materials Interfaces 2016, 3.

(152) Gates, B. D.; Xu, Q.; Stewart, M.; Ryan, D.; Willson, C. G.; Whitesides, G. M. Chemical Reviews 2005, 105, 1171.

(153) Li, M.; Ober, C. K. Materials Today 2006, 9, 30.

(154) Hedrick, J.; Labadie, J.; Russell, T.; Hofer, D.; Wakharker, V. Polymer 1993, 34, 4717.

(155) Hedrick, J. L.; Russell, T. P.; Labadie, J.; Lucas, M.; Swanson, S. Polymer 1995, 36, 2685.

(156) Le Mong, A.; Kim, D. J Power Sources 2016, 304, 301.

(157) Gindt, B. P.; Abebe, D. G.; Tang, Z. J.; Lindsey, M. B.; Chen, J.; Elgammal, R. A.; Zawodzinski, T. A.; Fujiwara, T. J. Mater. Chem. A 2016, 4, 4288.

(158) Ilavsky, J.; Jemian, P. R. Journal of Applied Crystallography 2009, 42, 347.

(159) Mark, J. E. Polymer data handbook; 2nd ed.; Oxford University Press: Oxford ; New York, 2009.

(160) Wypych, G. Handbook of polymers; Second edition. ed.

(161) Kilduff, J. E.; Mattaraj, S.; Zhou, M. Y.; Belfort, G. Journal of Nanoparticle Research 2005, 7, 525.

(162) Kaeselev, B.; Pieracci, J.; Belfort, G. J Membrane Sci 2001, 194, 245.

(163) Kilduff, J. E.; Mattaraj, S.; Pieracci, J. P.; Belfort, G. Desalination 2000, 132, 133.

(164) Nabe, A.; Staude, E.; Belfort, G. J Membrane Sci 1997, 133, 57.

(165) Pieracci, J.; Crivello, J. V.; Belfort, G. J Membrane Sci 1999, 156, 223.

(166) Pieracci, J.; Wood, D. W.; Crivello, J. V.; Belfort, G. Chemistry of Materials 2000, 12, 2123.

(167) Yamagishi, H.; Crivello, J. V.; Belfort, G. J Membrane Sci 1995, 105, 237.

(168) Yamashita, T.; Tomitaka, H.; Kudo, T.; Horie, K.; Mita, I. Polym. Degrad. Stabil. 1993, 39, 47.

(169) Plueddemann, E. P. Silane coupling agents; Second edition. ed.

(170) Plueddemann, E. P. Silane coupling agents; Plenum: New York ; London, 1982.

(171) Plueddemann, E. P.; Pape, P. G. Abstr Pap Am Chem S 1986, 192, 30.

(172) Mittal, K. L.; Plueddemann, E. P. Silanes and other coupling agents; VSP: Utrecht, 1992.

(173) Xie, Y. J.; Hill, C. A. S.; Xiao, Z. F.; Militz, H.; Mai, C. Composites Part a-Applied Science and Manufacturing 2010, 41, 806.

(174) Arkles, B. Chemtech 1977, 7, 766.

APPENDIX

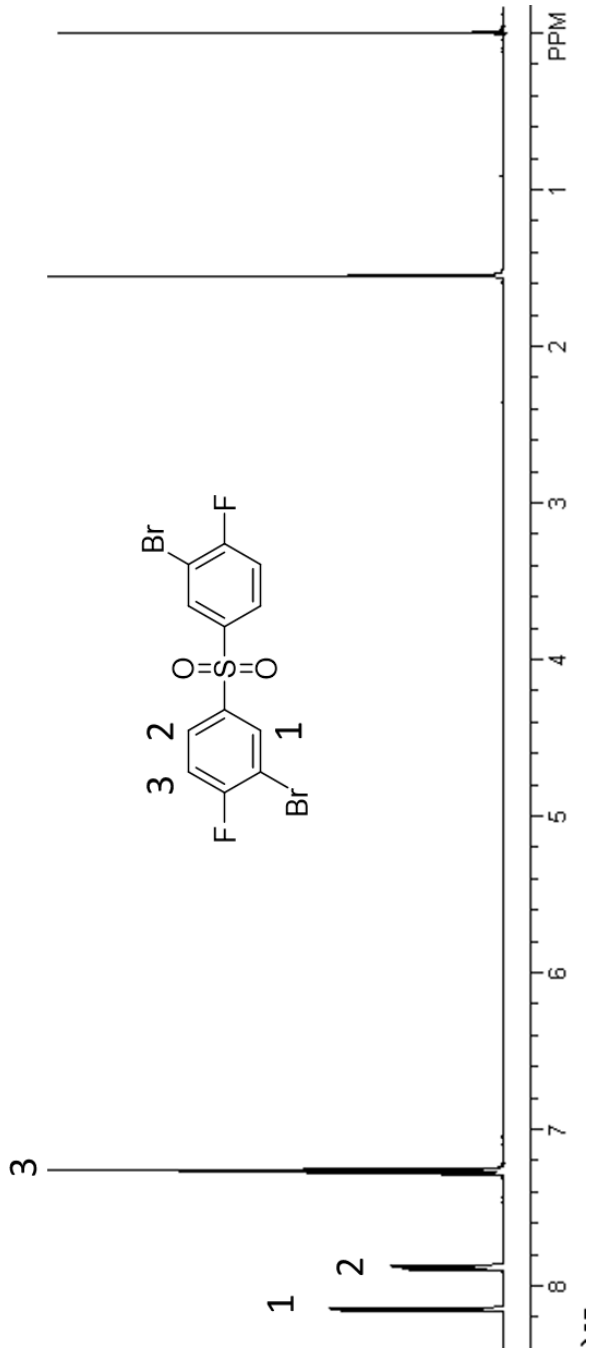

A. 1 4,4'-sulfonylbis(2-bromo-1-fluorobenzene) (dbDFDPS) ^{1}H NMR run on a Varian 500 MHz magnet in $CDCl_3$ using Trimethylsilane (TMS) reference at 0 ppm.

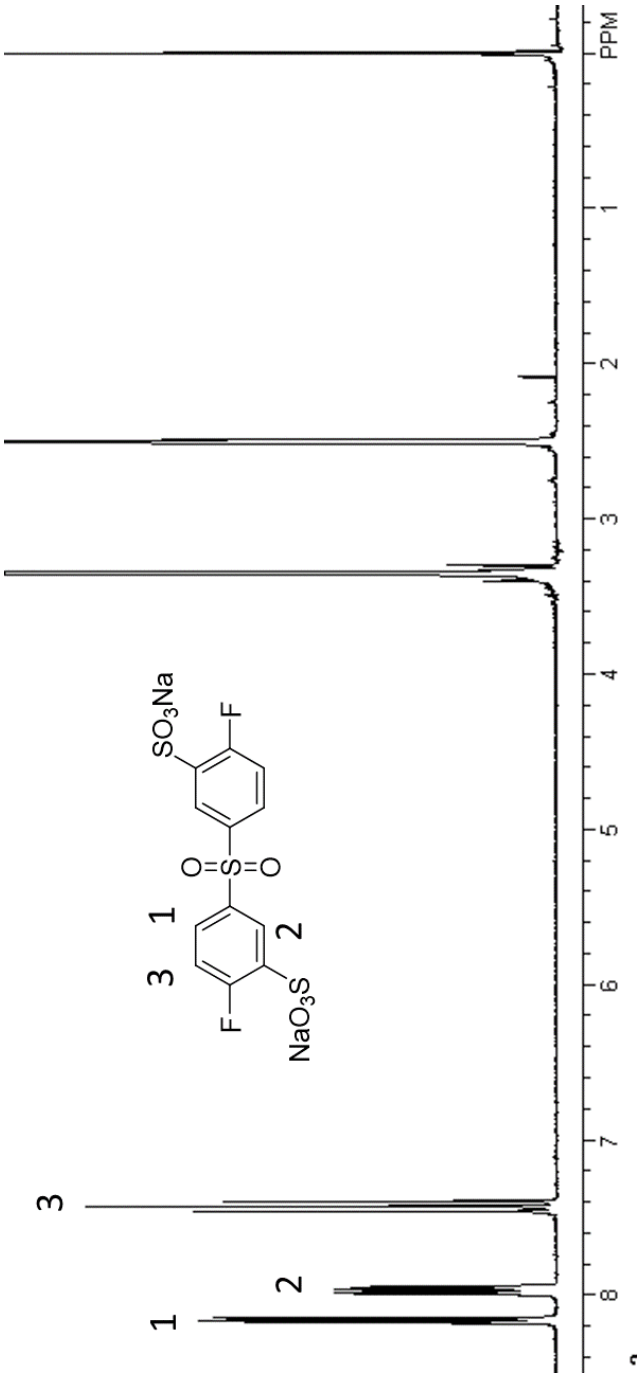

A. 2 Sodium 5,5'-sulfonylbis(2-fluorobenzenesulfonate) ^{1}H NMR run on a Varian 500 MHz magnet in $CDCl_3$ using Trimethylsilane (TMS) reference at 0 ppm.

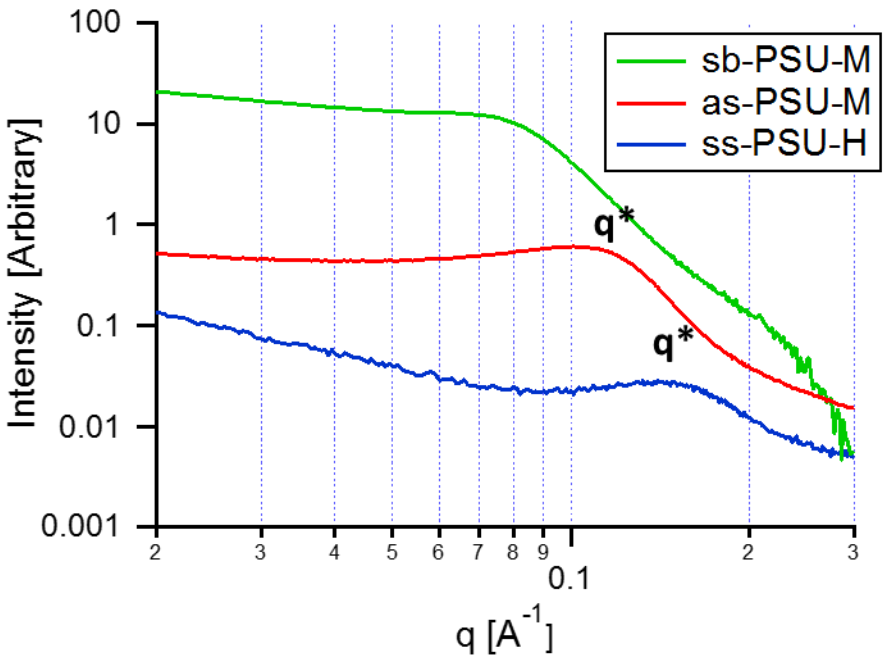

A. 3 SAXS curve of ss-PSU-H (bottom), as-PSU-H (top), and sb-PSU-H (middle). Data was collected in a quartz cuvette filled with H_2O using a blank for background subtraction. Plotted as intensity vs scattering vector q.

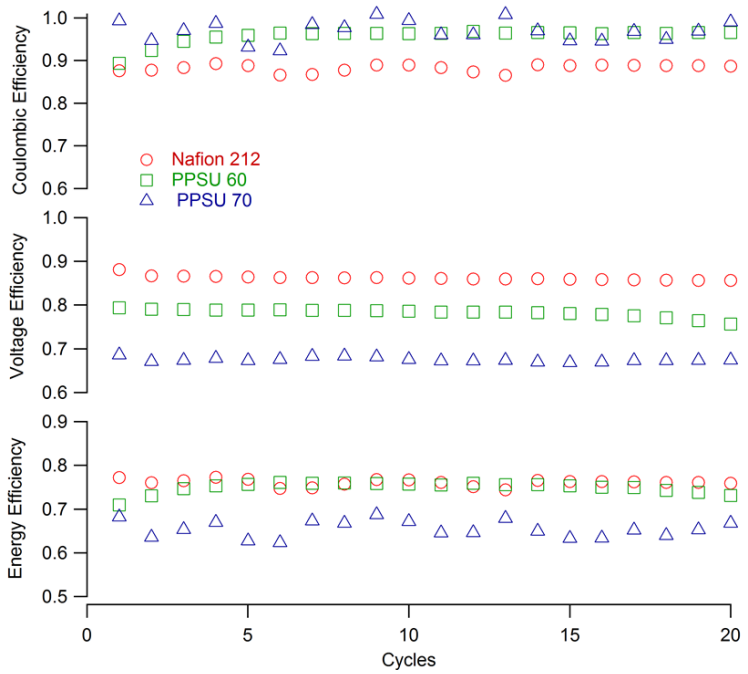

A. 4 VRFB cycling using: 1) PPSU70-X15 (triangle), 2) PPSU60-X15 (square), 3) Nafion 212 (circle). Cycling at 200 mA cm^{-2} using SGL 7013 carbon paper electrode compressed from 400 µm to 250 µm. Electrolyte volume of 50 mL of 1.7 M V^{x+} in 5 M SO_3^{2-}.

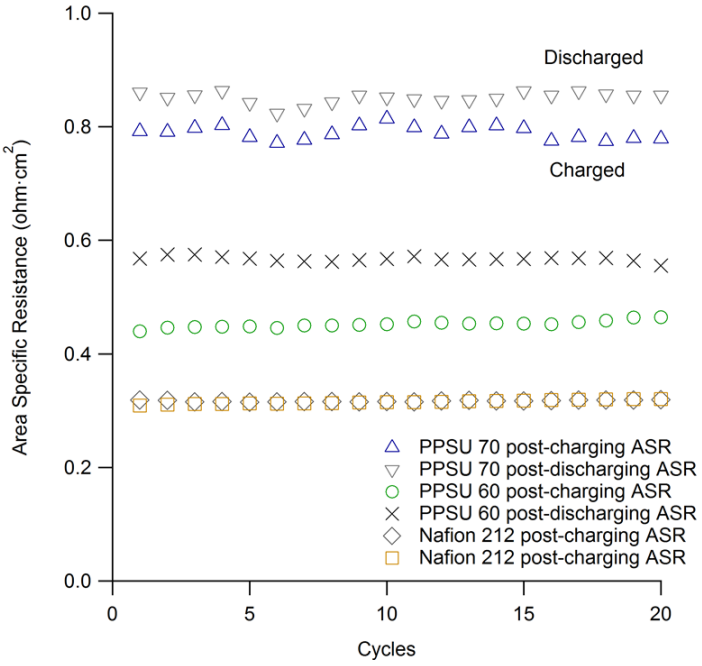

A. 5 Areal specific resistance during charging and discharging: 1) PPSU70-X15, 2) PPSU60-X15, 3) Nafion 212. Cycling at 200 mA cm-2 using SGL 7013 carbon paper electrode compressed from 400 μm to 250 μm. Electrolyte volume of 50 mL of 1.7 M V^{x+} in 5 M SO_3^{2-}.

Table A. 1 Permeability data of selected membranes for VO^{2+}. Collected through standard procedures described elsewhere.[43]

Membrane	**Permeability ($m^2 s^{-1}$)**
Nafion 211	1.05508×10^{-11}
PPSU60-X15	5.9186×10^{-14}
PPSU60-X15 ACID modified	1.4058×10^{-13}
PPSU70-X15	5.3148×10^{-12}
PPSU70-X15 ACID modified	2.0262×10^{-12}

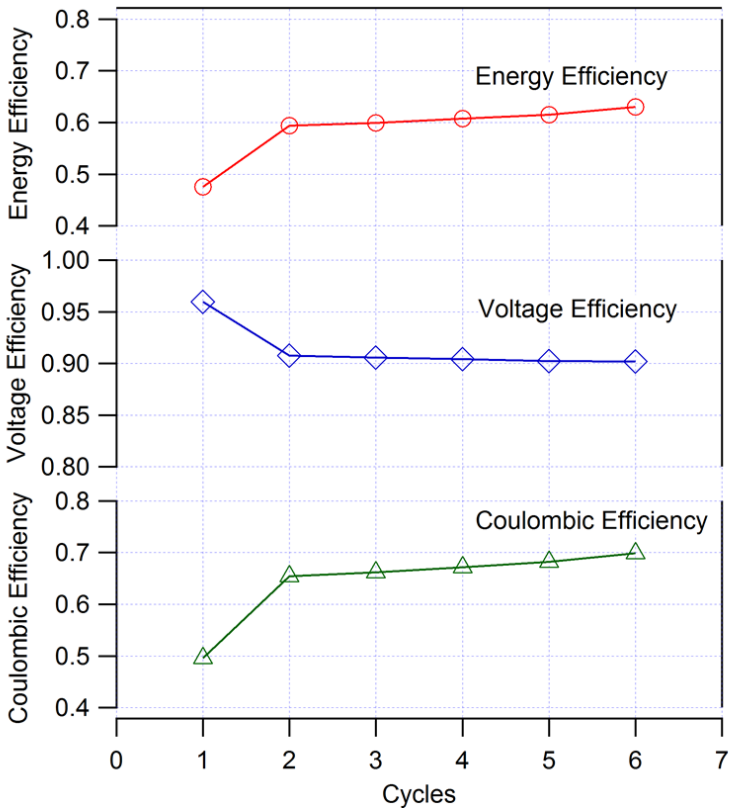

A. 6 PPSU54-X10 (PPSU M_n= 21,500) cycling at 60 mA cm^{-2} using SGL 7013 carbon paper electrode compressed from 400 µm to 250 µm. Electrolyte volume of 50 mL of 1.7 M V^{x+} in 5 M SO_3^{2-}. Theoretical capacity of 4100 C. Flow rate at 50 mL/min at 23 °C.

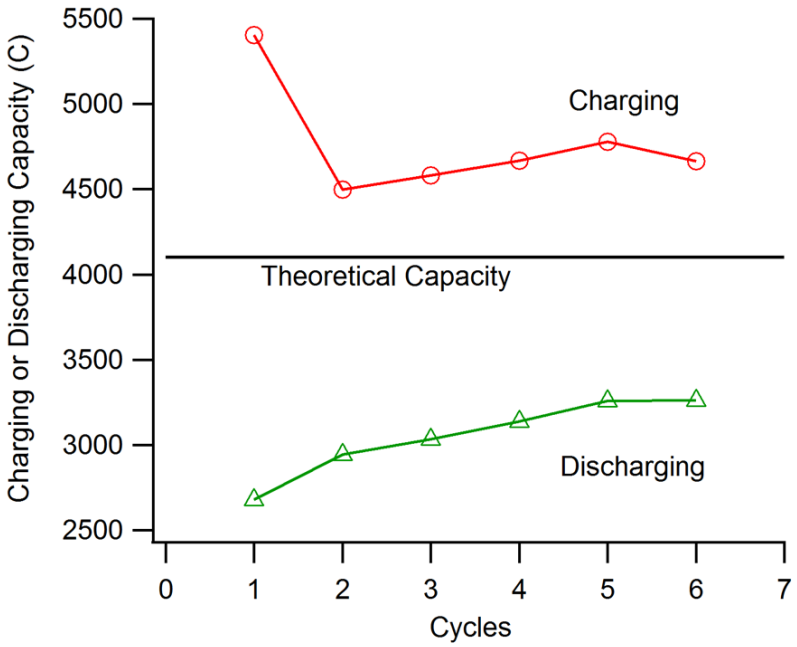

A. 7 PPSU54-X10 (PPSU M_n= 21,500) cycling at 60 mA cm^{-2} using SGL 7013 carbon paper electrode compressed from 400 µm to 250 µm. Electrolyte volume of 50 mL of 1.7 M V^{x+} in 5 M SO_3^{2-}. Theoretical capacity of 4100 C. Flow rate at 50 mL/min at 23 °C.

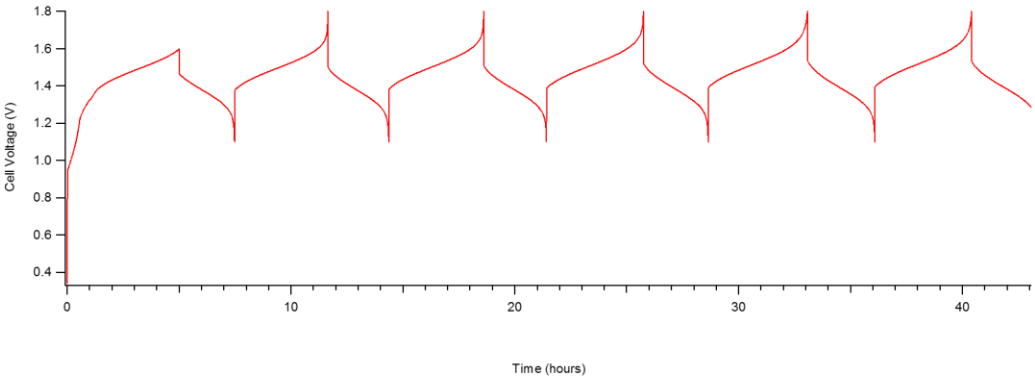

A. 8 Cycling curve of PPSU54-X10 (PPSU M_n= 21,500) during 6 cycles corresponding to Figure A.8 cycling data.

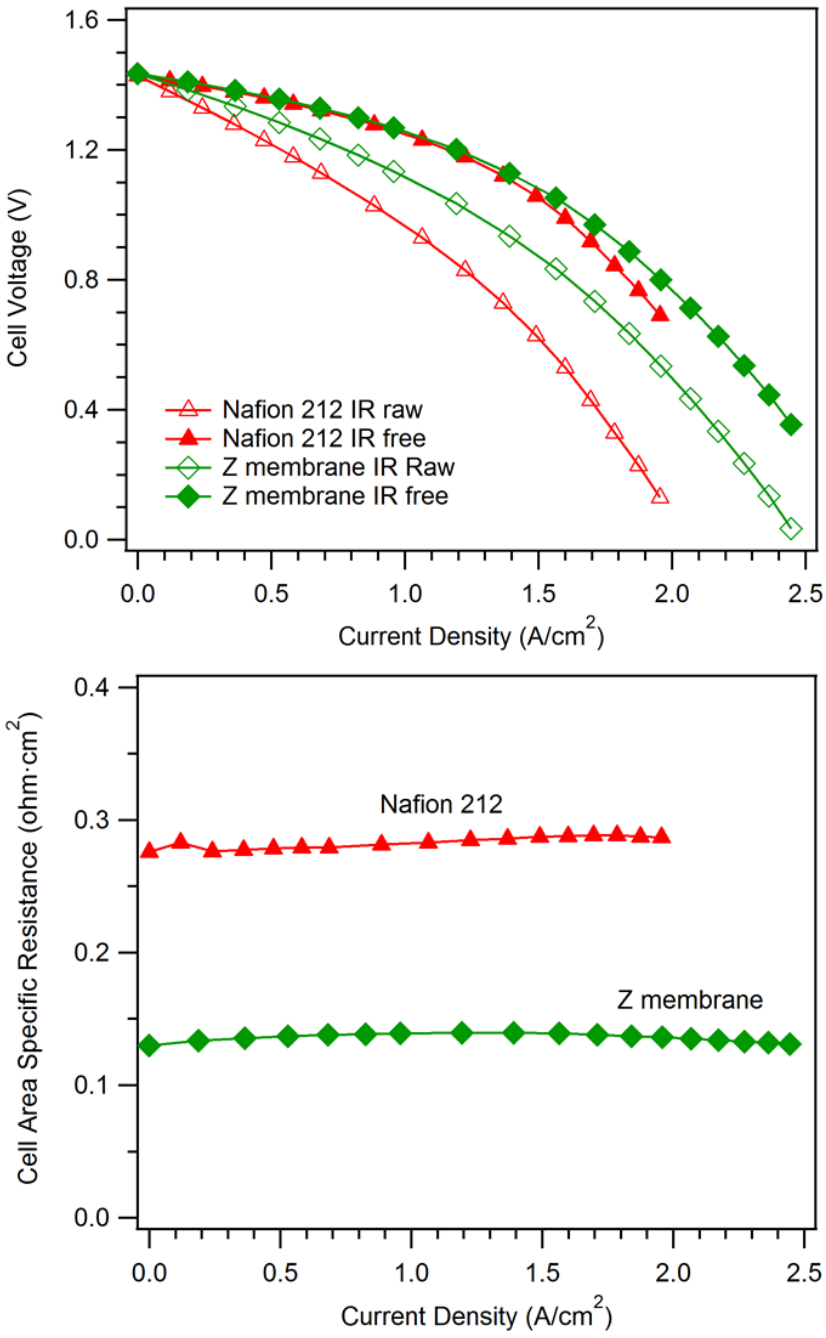

A. 9 PPSU54-X10 (PPSU Mn= 21,500) polarization curve. 55% state of charge constant. SGL 7013 carbon paper electrode compressed from 400 μm to 250 μm. Electrolyte 1.7 M V^{x+} in 5 M SO_3^{2-}. Flow rate at 50 mL min^{-1} at 23 °C.

Table A. 2 Summary of nanoporous membranes used for analysis including polymer molecular weight information.

ID	Membrane Summary	PSU weight fraction	XL percentage	Polymer M_n (GPC)	PDI (GPC)	Polymer M_n (NMR)	Macroinitiator summary	PPSU macroinitiator M_n (HNMR)	PPSU macroinitiator M_n (GPC)	Initiator PDI
PT8	PPSU51.5-X20	51.5	20	40648	1.67	44431	PSU-x20	23431	13774	2.88
PT16	PPSU52.3-X20	52.3	20	41671	1.69	44700	PSU-x20	23431	13774	2.88
PT23	PPSU61.2-X20	61.2	20	33403	1.72	38200	PSU-x20	23431	13774	2.88
PT21	PPSU63.4-X20	63.4	20	35047	1.69	37000	PSU-x20	23431	13774	2.88
PT18	PPSU70.2-X20	70.2	20	30938	1.71	33223	PSU-x20	23431	13774	2.88
PT10	PPSU51.5-X20	51.5	20	40648	1.67	44431	PSU-x20	23431	13774	2.88
PT20	PPSU52.3-X20	52.3	20	41671	1.69	44700	PSU-x20	23431	13774	2.88
PT22	PPSU61.2-X20	61.2	20	33403	1.72	38200	PSU-x20	23431	13774	2.88
PT15	PPSU63.4-X20	63.4	20	35047	1.69	37000	PSU-x20	23431	13774	2.88
PT19	PPSU70.2-X20	70.2	20	30938	1.71	33223	PSU-x20	23431	13774	2.88
PT5	PPSU51-x10	51	10	42737	1.43		PSU-x10	24000	13008	2.65
PT9	PPSU48-X25	48	25	38291	1.69		PSU-x25	19500	12722	2.86
PT4	PPSU55-x15	55	15	38366	1.58		PSU-x15	23000	14596	2.8
PT6	PPSU48-X25	48	25	38291	1.69		PSU-x25	19500	12722	2.86
FR 1	PPSU50-x25	50	25			45000	PSU-x25	19500	12722	2.86
FR 2	PPSU50-x15	50	15	41396	1.64	48159	PSU-x15	24500	17742	2.32
FR 3	PPSU49-x5	49	5	38648	1.46		PSU-x5	20000	12085	2.63

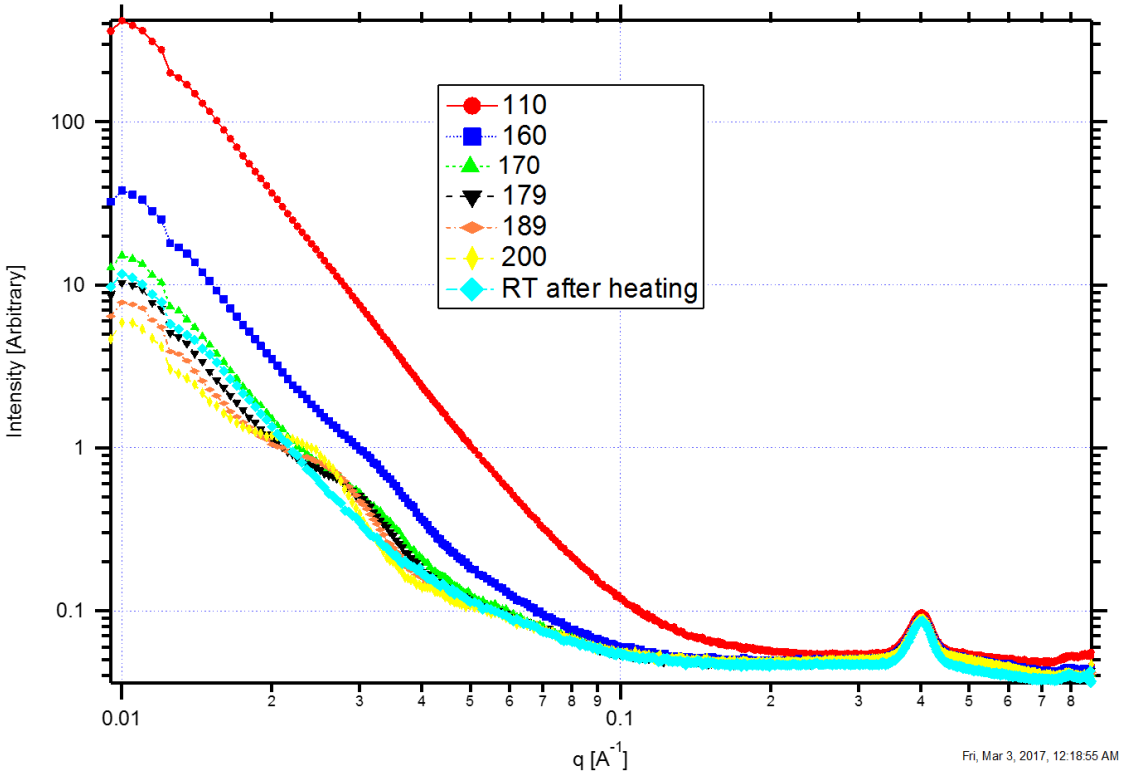

A. 10 Temperature responsive SAXS curves of PPSU50-X15 (PPSU M_n= 20,000). SAXS was measured every 10 minutes while temperature was increased at increments of 10 °C/min from RT → 200 °C.

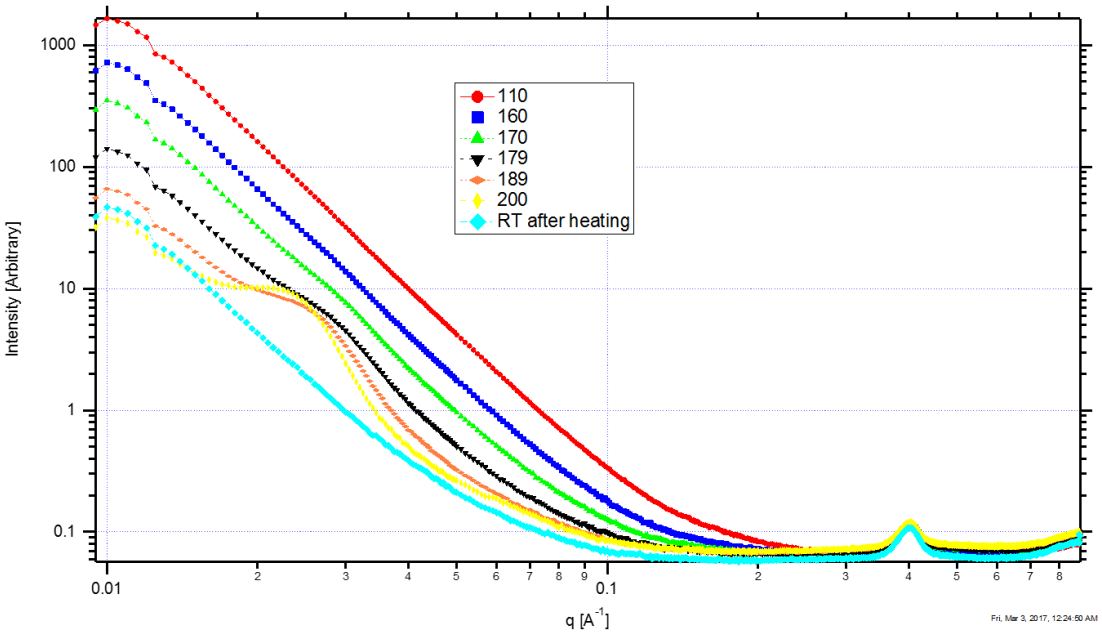

A. 11 Temperature responsive SAXS curves of PPSU51-X15 (PPSU M_n= 20,000). SAXS was measured every 10 minutes while temperature was increased at increments of 10 °C/min from RT → 200 °C.

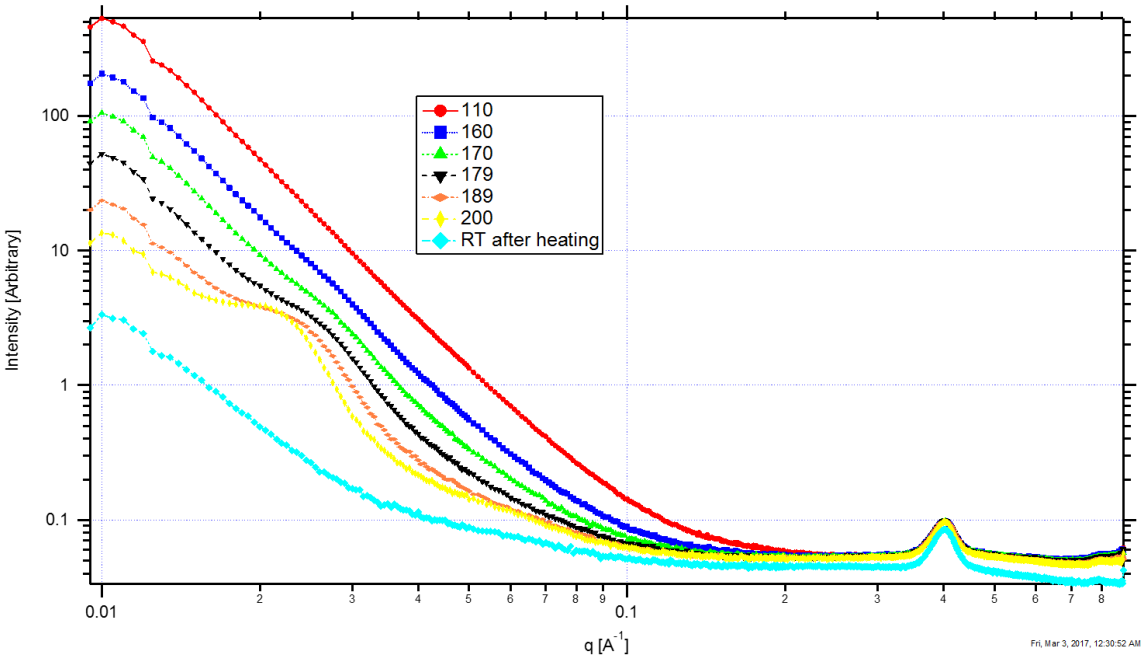

A. 12 Temperature responsive SAXS curves of PPSU54-X15 (PPSU M_n= 20,000). SAXS was measured every 10 minutes while temperature was increased at increments of 10 °C/min from RT → 200 °C.

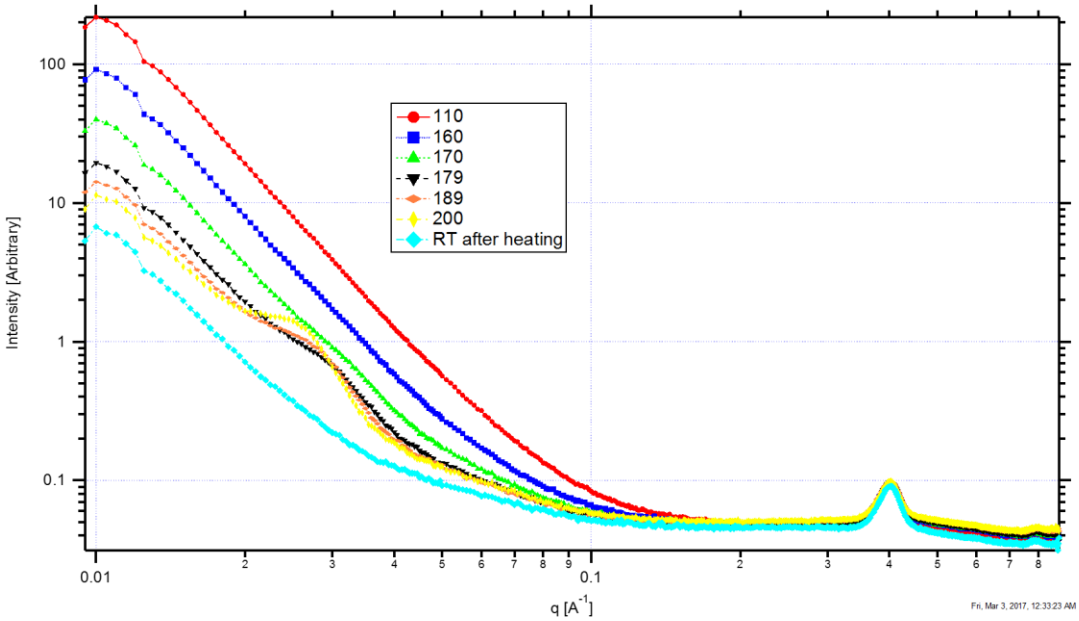

A. 13 Temperature responsive SAXS curves of PPSU52.3-X20 (PPSU M_n= 23,000). SAXS was measured every 10 minutes while temperature was increased at increments of 10 °C/min from RT → 200 °C.

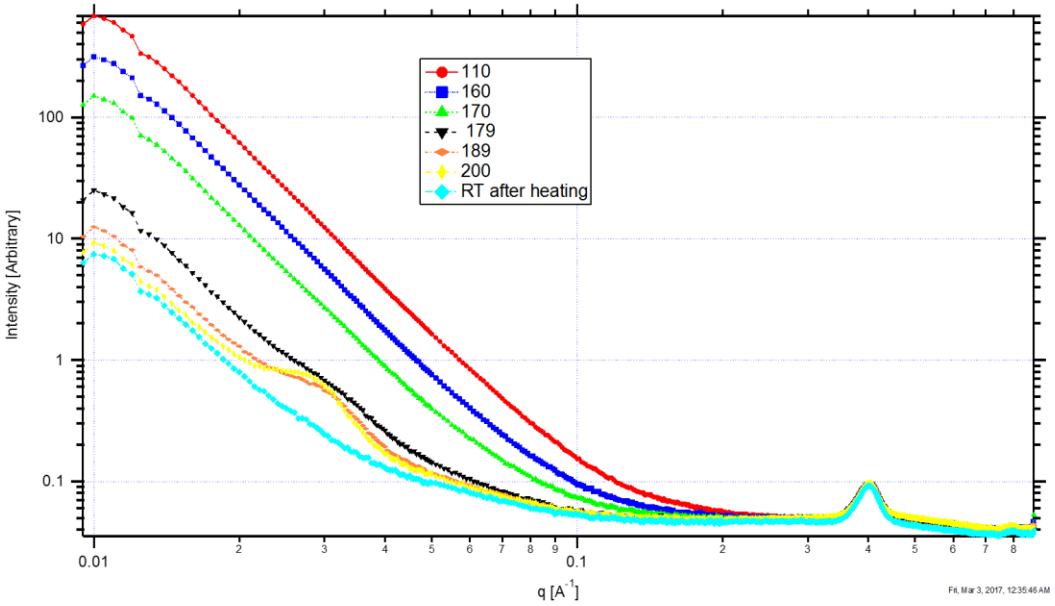

A. 14 Temperature responsive SAXS curves of PPSU63.4-X20 (PPSU M_n= 23,000). SAXS was measured every 10 minutes while temperature was increased at increments of 10 °C/min from RT → 200 °C.

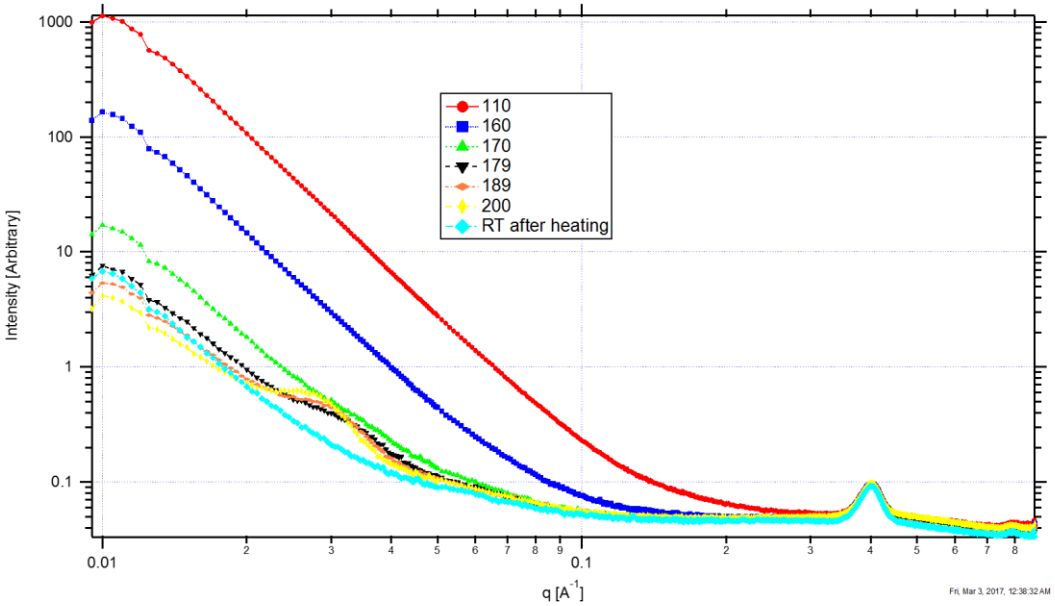

A. 15 Temperature responsive SAXS curves of PPSU61.2-X20 (PPSU M_n= 23,000). SAXS was measured every 10 minutes while temperature was increased at increments of 10 °C/min from RT → 200 °C.

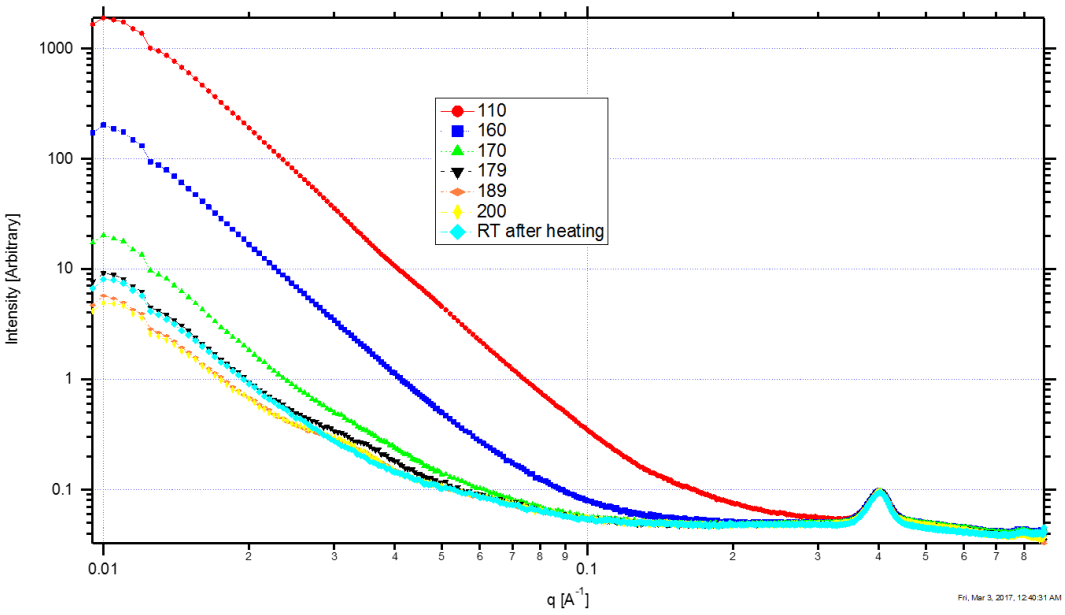

A. 16 Temperature responsive SAXS curves of PPSU70.2-X20 (PPSU M_n= 23,000). SAXS was measured every 10 minutes while temperature was increased at increments of 10 °C/min from RT → 200 °C.

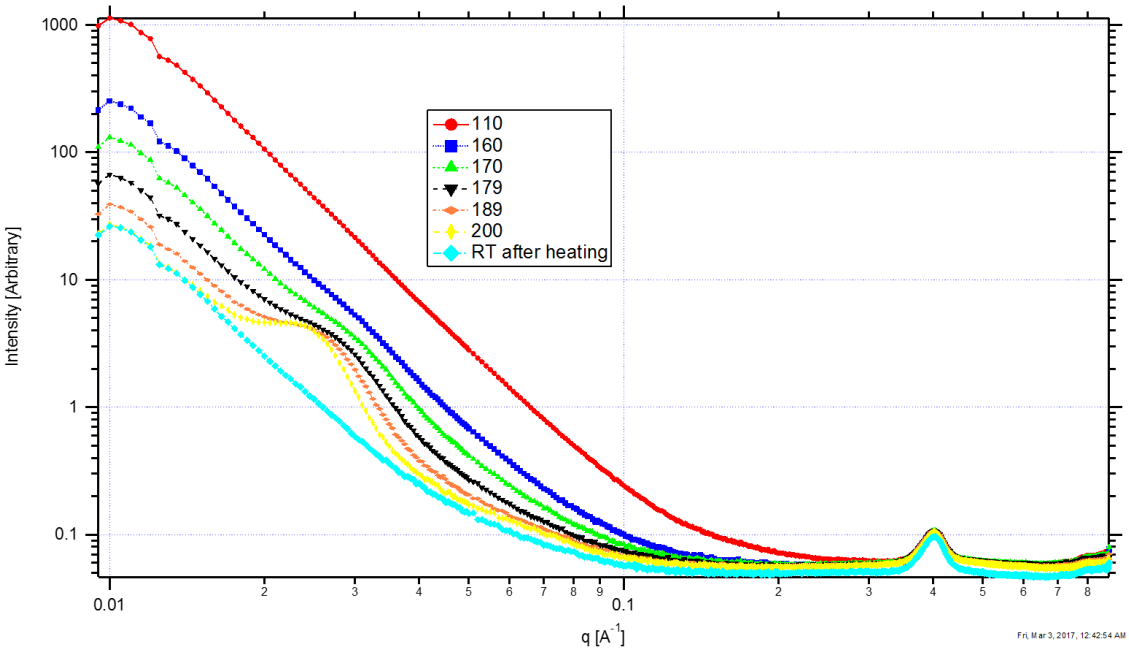

A. 17 Temperature responsive SAXS curves of PPSU~60-X20 M_n= 23,000). SAXS was measured every 10 minutes while temperature was increased at increments of 10 °C/min from RT → 200 °C.

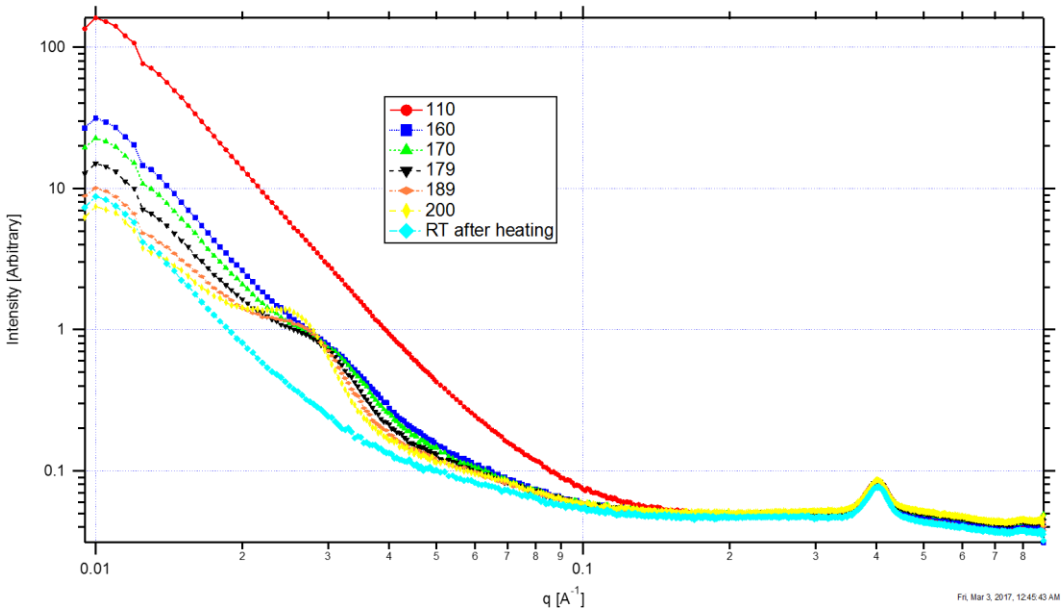

A. 18 Temperature responsive SAXS curves of PPSU61.2-X20 (PPSU M_n= 23,000). SAXS was measured every 10 minutes while temperature was increased at increments of 10 °C/min from RT → 200 °C.

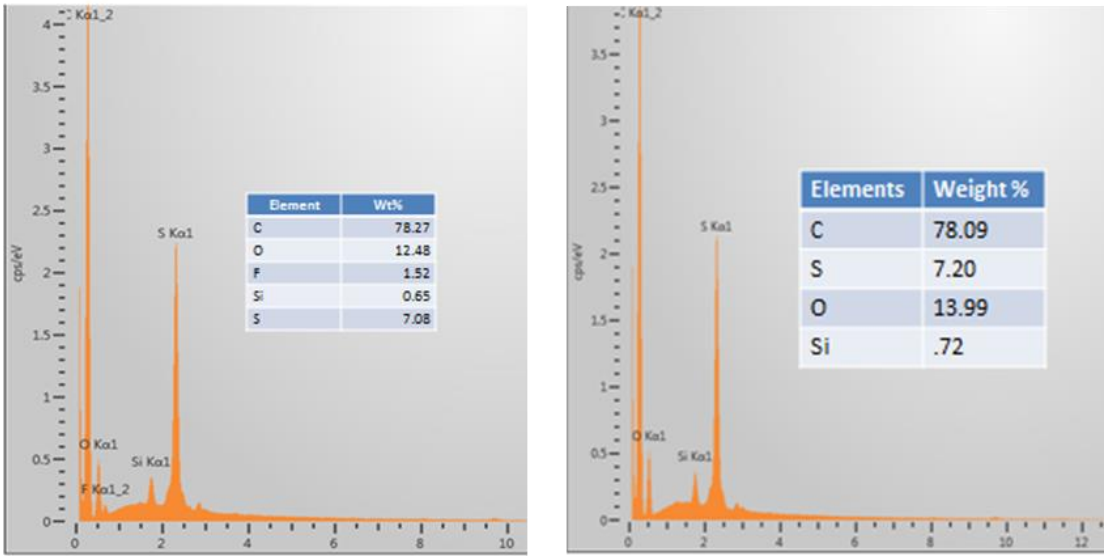

A. 19 EDS spectra of silane functionalized nanoporous PSU membranes. Left) TES-PF (see chapter 5) modification of PPSU 65-X25. Right) TES-AP (see chapter 5) modification of PPSU 65-X25

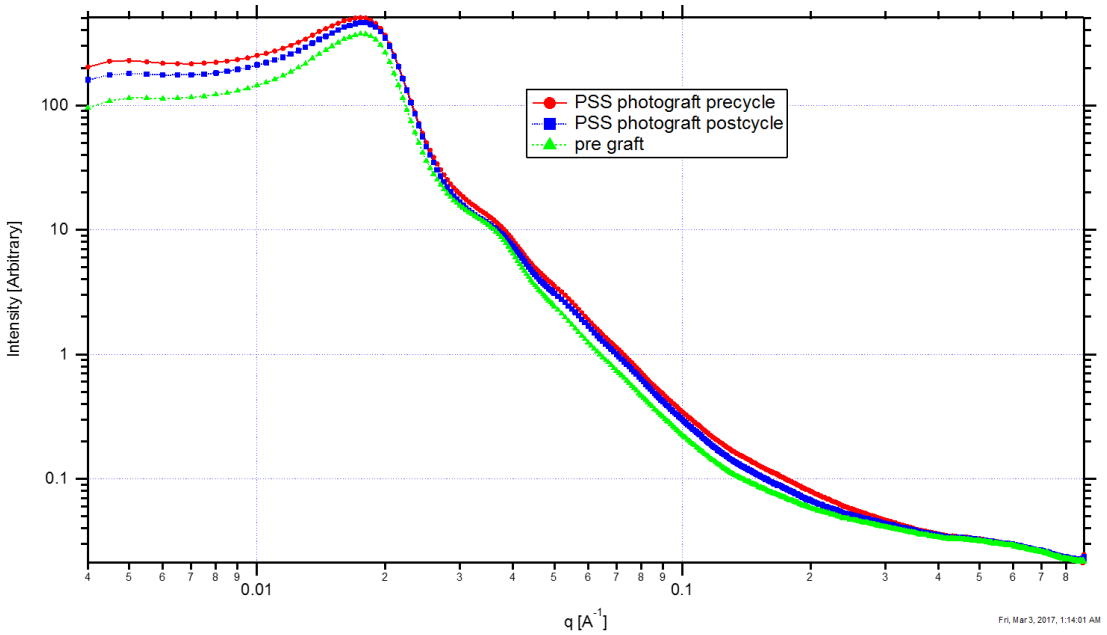

A. 20 SAXS curves of pre- and post- graft using 4-polystyrenesulfonate onto PPSU50-X10 (PPSU M_n= 22,000). Pre- and post- cycling in a VRFB is also given. Photograft polymerization conditions as well as cycling conditions are seen in chapter 5.

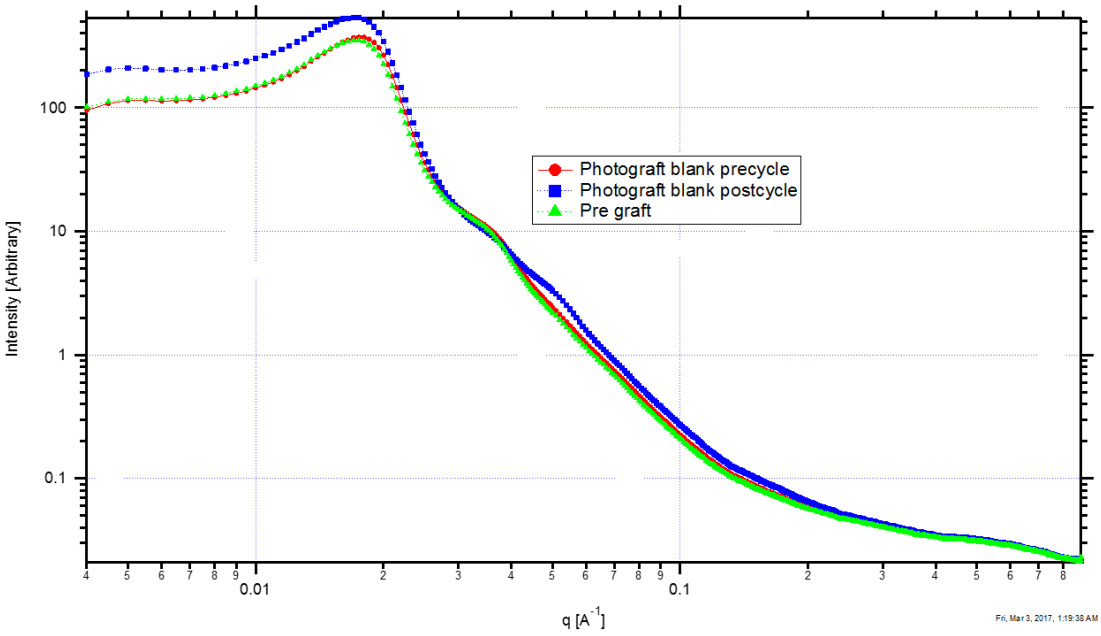

A. 21 SAXS curves of pre- and post- blank graft onto PPSU50-X10 (PPSU M_n= 22,000). Pre- and post- cycling in a VRFB is also given. Photograft polymerization conditions as well as cycling conditions are seen in chapter 5.